Optical parameter sensing: sensitivity limits and the advantages of using spatial modes of light

Arturo Villegas Juarez

Supervisor:

Dr. Juan P. Torres

Quantum Engineering of Light Research Group

A dissertation submitted in partial fulfillment of the requirements for the degree of

Doctor of Philosophy

ICFO - The Institute of Photonic Sciences
UPC - Universitat Politècnica de Catalunya

March 2023
Barcelona, Spain

Funded by the European Union

Thesis advisor:

Prof. Dr. Juan P. Torres

Thesis committee:

Dr. Pablo Loza-Alvarez (ICFO, Barcelona, Spain)
Dr. Etienne Brasselet (University of Bordeaux, Bordeaux, France)
Dr. Armand Koolen (ASML Research, Veldhoven, The Netherlands)
Dr. Luis Arturo Aleman-Castaneda (Fresnel Institut, Marseille, France)
Dr. David Artigas (Universitat Politécnica de Catalunya, Barcelona, Spain)

A mis padres y mi hermana,
y a cada nodo de mi red afectiva que me han acompañado amorosamente.

To the teenager I once was, who dreamt of being called a Doctor.
You made it young man!

"In order for the light to shine so brightly, the darkness must be present."

Francis Bacon

Acknowledgements

This dissertation is the culmination of a journey that started in 2010 and it is the result of a collaborative effort of many people who had contributed to get me through it. In a personal level, I want to thank my family; my parents Guadalupe and Arturo, and my sister Nayeli for their unconditional love and support. Also, my therapist and mentor Magda Solé for showing me how healing the sole presence could be, but mainly for guiding me towards finding true love. To Jaume Mestres and all the team of the IPTB, you all have contributed to the acceptance and understanding of my current self. Thanks to my partner and companion Raquel, for so much love and absolute beauty; but more importantly for your presence and company an patience regardless the distance and time. T'estimo més cada dijous.

On the other hand, in a professional level I would like to acknowledge the National Autonomous University of Mexico for giving me a first glance to science and to meet scientists that made me fall in love with physics. Similarly to the Delft University of Technology for showing me the tough way to believe in my capabilities. I acknowledge as well the professors that I had the pleasure to learn from and who became my mentors by guiding me not only through relevant career decisions but also through life choices: Andres Porta, Rocio Jáuregui, Paul Urbach, Omar El Gawhary, Silvania Pereira and Nandini Bhattacharya.

A big thanks to my closest ICFOnians, who from colleagues became friends and then family: Nicolas Mateos, Paolo Abiuso, Matteo Scandi, Jacopo Sorace and Dario De Santis. We built memories together that I hold very close to my heart. To all the ICFO community, starting with Lluis Torner for leading this institution so greatly. To Anne Gstottner for her kindness and empathy, and together with Ingrid Solsona for the support with relocation, migratory issues, and other official matters. To the academic affairs, KTT and outreach units, and the communications team for the enjoyable collaborations; specially to Brook Hardwick, Andrea Morales, Marta Martin, Tomás Charles, Elena Enrique and Mercé Latorre, for the help and support to carry on our ideas, and for the great chats and fun. To the former and current ICONS members, not only for the time and energy invested in bringing people together, but also for seeing the relevance and importance of it. To Oriol Bardés and the IT department, logistics and facilities management, mainly to Carlos Dengra for keeping everything working properly, but specially for all the help and support through our transition period of transportation and merging our two labs into a single one. To Silvania Pereira, Robert Sewell, Silvia Carrasco, Joan Gené, Luis A. Alemán-Castaneda and Pablo Loza for their advice and guidance at the very end of this process.

Finally, many thanks to Juan P. Torres for giving me the opportunity of being part of this great institution, and for the supervision of this thesis. To the Quantum Engineering of Light (QIP) group and its current and former members who I had the pleasure to work with: Gerard Gimenez-Machado, Daniel Urrego, Marcello Passos and Joan Gené; Carmelo Rosalez-Guzman, Roberto Leon-Montiel, Oscar Cordero, Juan Rafael Alvarez and Miren Lamaisson.

The research carried out in this thesis was supported by PREBIST through the INCOMING Fellowship that has received funding from the European Union's Horizon 2020 research and innovation program under the Marie Sklodowska-Curie Cofunding of Regional, National and International Programmes - COFUND of the European Commission with grant agreement No 754558. This thesis project was part of the project "BeCOMe - Beyond Classical Optical Metrology" 17FUN01 as well as "POLight - Pushing boundaries of nano-dimensional metrology by light" 20FUN02 of the EMPIR-Fundamental programme cofinanced by the Participating States and from the European Union's Horizon 2020 research and innovation programme financed by EURAMET - European Association of National Metrology Institutes.

Abstract

Resolution enhancement in modern optical metrology techniques has been possible due to significant technological improvements. The accurate and precise control of wavelength, bandwidth, and power of light sources; homogeneity, high-quality composition materials and surface smoothness of optical elements; and highly stable nanopositioners and optomechanical components, allow more sensitive imaging and sensing, in certain scenarios even beyond the standard diffraction limit. This has motivated a more detailed study of the fundamental resolution limitations of an optical system.

The chosen approach to address this problem is to consider optical imaging as a parameter estimation problem. With this in mind, the theory of quantum estimation and statistical inference provides the tools to determine the estimation precision limits. Starting by considering the state of light as a quantum state that carries information of interest; the Crámer-Rao lower bound provides a fundamental limit for the achievable precision. This lower bound is directly associated to optical resolution in practical terms.

In this thesis, we present an overview of the useful tools of quantum estimation theory that can be applied to optical metrology. We focus on the Crámer-Rao lower bound, and provide methods to calculate it. Since the bound depends on specific characteristics of the system, we explore three specific possibilities. First we present with an example the validity regimes for different bounds; explicitly in the frame of a quantum Lidar system. Second, we show the dependency of the lower bound on the photonic model selection, showing a discrepancy between two particular models. Third, we study the effects of lossy environments in the informational content of the quantum state.

Additionally, we present the conditions that a measuring strategy must satisfy to allow attainability of the fundamental limit. For specific scenarios of interest, measurement methods based on the use of spatial modes of light allow to asymptotically attain the resolution limit. This has drawn attention to the information carried by specific spatial modes, and has motivated the design of measurement strategies based on probing or sensing using different sets of spatial modes. In this thesis we include an overview of spatial modes of light, their generation and detection, and their use for optical sensing. We present a method for optical beam localization in the transverse plane using spatial mode information. Moreover, we propose a technique to retrieve the full modal decomposition of an arbitrary beam; which combined with the adequate set of modes allows to estimate certain parameters of an optical state with the maximum precision possible.

Finally, motivated by the informational content of an optical beam that is not easily accessible, we explore the use of artificial intelligence to extract information about spatial features of an object from its diffraction pattern; without the need of solving the inverse problem nor using a physical model of scattering.

Resumen

Las mejoras de resolución en técnicas modernas de metrología óptica se deben al significativo progreso tecnológico. El control preciso de la longitud de onda, ancho de banda y potencia de las fuentes de luz; la homogeneidad, los componentes de alta calidad y lisura superficial de los elementos ópticos; mas la alta estabilidad de nanoposicionadores y componentes optomecánicos, permite imagenología y detección más sensible, en ciertos escenarios, incluso más allá del límite de difracción estándar. Esto ha motivado un estudio más detallado de los limites fundamentales de un sistema óptico.

El enfoque elegido para dirigirse a este problema consiste en considerar la imagenología óptica como un problema de estimación de parámetros. Con esto en mente, la teoría de estimación cuántica e inferencia estadística provee las herramientas para determinar los límites de precisión en la estimación. Comenzando por considerar el estado de luz como un estado cuántico que porta información de interés; el límite inferior de Crámer-Rao provee un límite fundamental para la precisión alcanzable. En términos prácticos este límite inferior está diréctamente asociado con la resolución óptica.

En esta tesis, presentamos un resumen de las herramientas útiles de la teoría de estimación cuántica que pueden ser aplicadas a la metrología óptica. Nos enfocamos en el límite inferior de Crámer-Rao y proveemos métodos para calcularlo. Dado que el límite depende de características específicas del sistema, exploramos tres posibilidades específicas. Primero, presentamos con un ejemplo los regímenes de validez de diferentes límites; explícitamente en el marco de un sistema Lidar cuántico. Segundo, mostramos la dependencia en límite inferior de la selección del modelo fotónico, mostrando una discrepancia entre dos modelos particulares. Tercero, estudiamos los efectos de ambientes con pérdidas en el contenido de información de un estado cuántico.

Adicionalmente, presentamos las condiciones que una estrategia de medición debe satisfacer para alncanzar el límite fundamental. Para escenarios específicos de interés, métodos de medición basados en el uso de modos espaciales de luz permiten alcanzar asintóticamente el límite de resolución. Esto ha atraído la atención hacia la información que portan modos específicos, y ha motivado el diseño de estrategias de medición basadas en sondeo y detección usando diferentes conjuntos de modos espaciales. En esta tesis incluímos un resumen sobre modos espaciales de luz, su generación y detección, y su uso en detección óptica. Presentamos un método para localización de haces de luz en el plano tranversal usando informacion de los modos espaciales. Más aún, proponemos una técnica para recuperar la descomposición modal completa de un haz arbitrario, lo cual combinado con el conjunto adecuado de modos permite estimar ciertos parámetros de un estado óptico con la máxima precisión posible.

Finalmente, motivados por la información contenida en haces ópticos que no es fácilmente accesible, exploramos el uso de inteligencia artificial para extraer información de características espaciales de objetos, del patrón de difracción; sin necesidad de resolver el problema inverso ni utilizar un modelo físico de dispersión.

List of publications

The research carried out and presented is dissertation has resulted in eight publications, seven research articles and one conference proceedings hereby presented in the same order as in the text.

- Miren Lamaison, **Arturo Villegas**, Akio Fujiwara and Juan P. Torres, *"The true quantum Crámer-Rao bound of a Lidar systems based on entangled photons."* To be sumitted. *(Chapter 2, section 2.3)*

- **Arturo Villegas**, Marcello H. M. Passos and Juan P. Torres, *"Quantum limits for the precision of optical parameter estimation of arbitrarily shaped phase objects"* Submitted to PRL on 28/02/ 2023. *(Chapter 2, section 2.4).* https://doi.org/10.48550/arXiv.2302.14504

- Oscar Cordero, **Arturo Villegas**, Juan-Rafael Alvarez, Roberto de J. León-Montiel, M. H. M. Passos, and Juan P. Torres, *"Equivalence regimes for geometric quantum discord and local quantum uncertainty"* Phys. Rev. A **104**, 042401 (2021). *(Chapter 2, section 2.5).* https://doi.org/10.1103/PhysRevA.104.042401

- Mirza Karamehmedovc, Kenneth Scheel, Frederik Listov-Saabye Pedersen, **Arturo Villegas**, and Poul-Erik Hansen, *"Steerable photonic jet for super-resolution microscopy"*, Opt. Express, **30**(23), page (2022). *(Chapter 3, section 3.2).* https://doi.org/10.1364/OE.472992

- **Arturo Villegas** and Juan P. Torres. *"Spatial spectroscopy for high resolution imaging."* EPJ Web of Conferences, vol. 238, p. 06005. EDP Sciences, 2020. *(Chapter 3, section 3.3).* https://doi.org/10.1051/epjconf/202023806005

- **Arturo Villegas**, Carmelo Rosales-Guzman, and Juan P. Torres *"Measurement of the position and orientation of arbitrary objects based on projection on spatial modes of light"* To be submitted. *(Chapter 3, section 3.4).*

- **Arturo Villegas**, Silvania F Pereira, Juan P. Torres, *"Optimum parameter estimation of phase objects by spatial mode projection"* To be submitted. *(Chapter 4, section 4.2).*

- **Arturo Villegas**, Mario A. Quiroz-Juárez, Alfred B. U'Ren, Juan P. Torres and Roberto de J. León-Montiel, *"Identification of Model Particle Mixtures Using Machine-Learning-Assisted Laser Diffraction"*, Photonics 2022, **9**(2), 74 (2022). *(Chapter 5)*.
https://doi.org/10.3390/photonics9020074

Contents

Chapter 1

Introduction

Our ability to design new nanometric circuits, in applications that range from the semiconductor industry to point-of-care testing devices for medicine, relies on our capacity to image with substantial resolution at the nanoscale. To achieve great imaging resolution one can make use of different techniques such as short wavelength illumination (UV, EUV, X rays), fluorescent response of chemical compounds added to the samples as markers, or scanning measurements either in the near field or in the far field regime. In the former, the scattered light is sensed very close to the sample where evanescent fields are still present, whereas far field measurements are combined with phase retrieval algorithms or compared to extensive simulations when a priori information of the sample is available. However, these techniques show particular drawbacks and are not generally applicable in many scenarios of interest.

Methods for spatial resolution enhancement

Direct imaging systems with no use of a priori information have optical resolution bounded by the *Rayleigh-Abbe criterion* [1]. This criterion states that, due to diffraction effects, the smallest spatial feature of an object that an imaging system can resolve is approximately $\lambda/2$ for conventional techniques employing direct intensity measurements, where λ is the wavelength of the illumination [2, 3].

When employing visible light the diffraction limit is of the order of hundreds of nanometers, even for the shortest wavelengths and sophisticated optical systems. This implies that, for direct imaging techniques, one way to improve the spatial resolution is to decrease the wavelength of the illumination even beyond the visible light regime, e.g. using extreme ultraviolet radiation (EUV) or X-rays [4]. However, in this wavelength domain the complexity of the imaging system grows. On the one hand the equipment in the UV and X wavelength domains is cumbersome, not only light sources are complex and require careful handling but also optical manipulation is extremely sensitive and optical components are limited. On the

other hand shorter wavelengths result in less sensitivity and shorter penetration depths due to absorption. Moreover, certain physical parameters are not necessarily unveiled at shorter wavelengths, such is the case of many optical transitions of interest.

Besides the use of illumination at shorter wavelengths, another approach is to use fluorescent responses to the probe or illumination beam. With the help of fluorophores, fluorescent chemical compounds that emit light upon optical excitation, super-resolved fluorescence microscopy *(Nobel prize in Chemistry in 2014)* demonstrated that transverse resolution well below the wavelength of the illumination (super-resolution) can be achieved with visible and infrared light in some particular cases. This set the basis for what is referred as *Nanoscopy*.

One of the most relevant techniques for Nanoscopy is Stimulated Emission Depletion (STED) microscopy [5, 6]. In this scheme a light beam is focused onto a diffraction-limited spot illuminating the sample doped with fluorophores. At the sample plane, a second beam is used to induce the fluorescent molecules located on the outer part of the focus to undergo stimulated emission, forcing the transition for those molecules onto the ground state. This results in an emitting spot that is tighter than the diffraction-limited focal spot, which is is equivalent to narrowing down the effective point spread function (PSF) of the optical system causing resolution enhancement. Fluorescent techniques are however not generally applicable and of no use in some cases such as imaging of inorganic materials in the semiconductor sector since they have no natural fluorescent response nor is the contamination with external markers allowed.

Resolution enhancement has also been achieved by measuring the light reflected or transmitted by the objects of interest in a region very close to the object. In the so called near-field regime, the evanescent fields with high spatial frequencies are still present and can be measured [7, 8]. Furthermore, with the use of engineered nanostructures (optical nanoantennas) the electromagnetic field can be locally enhanced due to plasmonic resonance, making possible to obtain high resolution images [9]. Moreover, if the interaction of the probe beam with the sample is confined to a sub-diffraction spot using a narrow aperture, it is possible to resolve features as small as $\lambda/10$, or $\lambda/20$ when using a sharp tip [10, 11]. Near-field scanning microscopy techniques are a major improvement in imaging resolution; however, the very low working distance combined with the need to image large sample areas requires very long scanning times making it unsuitable in many cases.

All the aforementioned techniques rely on measurements of the intensity of the light, considering only the modulus of the electromagnetic field and completely dismissing the complex nature of light. A powerful way to improve spatial resolution is to consider techniques that allow to use or extract information of the phase of the field since it carries very relevant information. When enough information about their geometry and physical parameters is available, the measurements could be compared to a set of simulated predictions generated through extensive and rigorous computation of the complete scattered field.

To generate the set of simulated scattered fields, the light-matter interaction is modelled as function of the parameters of the target and the complete complex field is computed using diffraction theory. The set of parameters is then determined by minimizing a distance between the measurement and the computed field, taking the noise in the measurement into account [12, 13]. This is particularly relevant for characterization or quality control of certain samples of interest in which an approximate value of the parameters is known. It is important to notice that a priori information about the sample is not always available and in many cases a comparison to thorough simulation models can imply a great computational effort.

Intensity measurements of the scattered field do not necessarily prevent extracting information about its phase. Using coherent illumination it is possible to transform phase changes into intensity changes without the need of high-power lenses [14]. These techniques often employ interferometric measurements, which require an independent reference light beam and make the system sensitive to external perturbations such as vibrations or temperature changes. This increases the setup complexity due to the need of stabilization. Nevertheless, one can reconstruct a complex field by calculating the phase relationship between different segments of the scattered field; this is, comparing intensity measurements (Fraunhoffer diffraction patterns) in which the illumination has been shifted with respect to the object. This method is referred to as *Ptychography*, and its main difference with holography consists in the fact that there is no need of an independent reference beam since interference occurs in the object itself [15, 16].

Given the diversity of novel imaging and non-imaging techniques for resolution enhancement in optical metrology, the standard and original definition and conception of resolution associated to Abbe's and Rayleygh's criterion must be modified [17].

Thesis goals and objectives

The aim of this project is to explore and develop novel techniques for optical metrology that allow to surpass the standard resolution limit making possible to extract sub-wavelength spatial information of an object using probe beams in the visible spectral range.

In this context, naturally two question arise. First: *"how far in terms of spatial resolution is it possible to go in the optical domain?"* One can address this question as a parameter estimation problem in which spatial resolution is directly linked to the estimation precision of spatial features as system's parameters. In the frame of quantum estimation theory, quantum mechanics and probability theory provide the tools to determine precision bounds for parameter estimation, allowing to answer this question and define the spatial resolution limit for a particular light-matter interaction scheme. It is important to remark the fact that these results can be obtained for any kind of experiments, even those that can be referred as classical.

This leads to the second question: *"is it possible to find an experimental technique that allows to reach the limit?"* After finding the precision bound and res-

olution limit, to answer this question one needs to explore the conditions for attainability of the limit; taking them into account one can tailor a measurement strategy that fulfils them.

These two questions define the first goal of this thesis, namely to define the fundamental limits of parameter estimation precision for a given light-matter interaction using tools provided by quantum estimation theory [18], as well as designing measurement techniques that allow to achieve or approach the limit. A relevant application of these methods is the measurement of spatial features of nanostructures in the semiconductor industry, where determining critical dimensions is fundamental to verify and control the performance of the nanofabrication process.

The second goal of this thesis is to design schemes based on the use of spatial modes of light (modal methods) for optical metrology. The proposed technique is based on probing using tailored beams as well as selective measurement of the modal components of the field. We consider the measurement of mode projections onto a certain set of spatial modes that carry particularly relevant information about the parameters of interest of the target [19–21]. We refer to this technique as *Spatial Spectroscopy* since it mimics in the spatial domain what conventional spectroscopy methods do in the frequency domain employing many frequencies (also refered to as hyperspectral imaging of wavefront sensing).

As a by-product, the proposed scheme also allows to determine the modal decomposition (amplitude and phase) of any light field in an arbitrary basis. This represents a major contribution since the determination of the phase is not straightforward with the currently available methods, since they require several measurements in which the sample must be displaced with respect to the probe beam.

The third and final goal of this thesis is to explore new approaches for parameter sensing in optical metrology. We consider the use of machine-learning-assisted techniques for improvements in the estimation of spatial features of micro- and nanoscopic objects.

The key objectives carried out in this thesis are the following:

- *Ultimate resolution limits for a given light-matter interaction*
  Using the tools provided by quantum estimation theory and a model for light-matter interaction, we determine the ultimate spatial resolution limits defined as the fundamental precision bounds for the estimators of spatial features of the object of interest.

- *Lower bound applicability conditions*
  We aim to determine the applicability of the fundamental estimation precision bounds considering different scenarios, namely different parameters of interest as well as the dependence of the bound with respect to the photonic-state model selection.

- *Attainability of the resolution limit*
  For a light-matter interaction model and a well defined estimation scheme, we define the conditions that need to be satisfied for the limit to be attainable.

- *Effects of lossy environments on phase estimation protocols*
  We consider the effects of losses in quantum phase estimation by studying the informational variation of quantum correlations.

- *Spatial Spectroscopy*
  We develop a technique for optical metrology using spatial modes of light for both probing and sensing. We evaluate the sensitivity of the technique and compare it with the fundamental limit.

- *Optimal measurements with spatial modes*
  We consider measurement techniques based on spatial modes that lead to the saturation of the the precision bounds. We study the conditions that the set of modes must satisfy for the measurement to be optimal, making possible to extract the maximum amount of information when estimating the parameters of a particular object.

- *Explore computational techniques for sensing*
  We aim at unveiling spatial features of interest from a set of diffraction patterns by using machine learning algorithms. In particular, we study the use neural networks to determine spatial features of objects by looking at its diffraction pattern.

Thesis outline

This thesis is presented as follows: following this introduction, **Chapter 2** contains the fundamental tools and concepts that allow to define the estimation precision lower bounds as the ultimate resolution limits. With the bounds defined, the applicability conditions are also presented in terms of the type and number of parameters to be estimated, as well as the chosen photonic-state model. In these lines, three particular situations are considered.

First, in Section 2.3 we present as an example the case of the estimation of conjugated variables, namely time delay and Doppler shift (position and momentum/velocity) of a target using a quantum lidar system, where the calculation of an attainable precision estimation bound is not straightforward and the validity of a commonly-used bound is proved not to apply.

Second, in Section 2.4 we evaluate the precision bounds for estimation of phases considering two different photonic-state modes, namely N copies of a single photon and a multimode coherent state with average photon number N. We demonstrate a discrepancy between the two models although they have been used equivalently in the literature. We present as an example the estimation of a phase acquired by an optical beam in two cases: propagating through a dispersive medium and reflecting by a cliff-like nanostructure.

Finally, in Section 2.5 we study the effects of lossy environments in the informational content of a quantum state by studying the quantum correlations of a two-photon entangled state in presence of non-symmetric losses.

In **Chapter 3** we introduce the concept of spatial modes of light starting from theory of electromagnetism and discuss some specific types of modes that naturally arise from the choice of coordinates. In Section 3.2 we discuss techniques for generation of spatial modes of light using laser beams, we focus attention on beam shaping techniques relying on computer-generated holograms displayed in liquid crystal spatial light modulators.

In Section 3.3 we propose a technique for optical metrology based on the use of spatial modes of light for both sensing and probing. To measure the modal components, we present an experimental scheme to retrieve the full modal decomposition of a beam by individually measuring each one of its coefficients using homodyne detection. In addition, we consider a different technique based on encoding modal phase information into the beam of interest followed by a projection onto the Gaussian (TEM_{00}) mode. Finally, in Section 3.4 we apply the aforementioned results for two-dimensional localization of optical beams in a transverse plane. We evaluate the sensitivity of the technique in terms of the precision bounds as defined in Chapter 2, and compare the obtained results to other measurement methods.

Combining the results from Chapter 2 and Chapter 3, **Chapter 4** presents the use of spatial modes for optimum parameter estimation. Starting from the most fundamental point of view, Section 4.1 includes a description of differential resolution, i.e. the estimation of the separation of two incoherent optical point sources using the tools provided by quantum estimation theory. Two main relevant results are included in this section. First, for incoherent sources the separation between the sources can be estimated with precision proportional to the number of photons detected, contrary to the standard resolution limit dictated by Rayleigh's diffraction limit. Second, using spatial mode projections one can achieve the ultimate resolution surpassing the limit that can be achieved using direct imaging or intensity measurements.

For a more general parameter estimation problem, in Section 4.2 we present the conditions for modal methods to be optimal; which in particular are satisfied for estimation of phases of quantum states of light or estimation of spatial features of non-absorptive objects in optical metrology. Moreover, we include a method to tailor spatial modes that lead to an optimal estimation and show as an example the estimation of the height and sidewall angle of a cliff-like nanostructure using the homodyne spatial mode analyzer introduced in Section 3.3.

Using a different formalism, in **Chapter 5** we study resolution-enhanced sensing using Machine-Learning-assisted laser diffraction analysis. Using Neural Networks, we present a method to estimate microscopic spatial features directly from diffraction patterns without the need of solving the inverse problem. As an example, we apply the technique to identification of model particle mixtures and retrieve information about the size, shape and ratio concentration of two-component heterogeneous model particle mixtures.

Finally **Chapter 6** contains the conclusions of this thesis as well as the proposed work to be carried out in the future.

Chapter 2

Fundamental precision bounds in optical parameter sensing using quantum estimation theory

A quantum-mechanical approach to parameter estimation and statistical inference allows to determine fundamental precision limits for estimation of the parameters of a system. Furthermore, they allow to define the precision bounds and sensitivity associated to a given measurement strategy [22, 23].

This formalism has been applied to optical metrology since 1970 [18, 24]. It considers optical metrology as a multi-parameter estimation problem in which one aims at extracting information of the spatial and physical parameters of a target of interest by investigating the effects that it has on the (classical or quantum) state of the beam of light used for probing.

This approach became significantly relevant in the past years due the work of M. Tsang and collaborators [25–27]. In their work, they showed that when measuring adequately, it is possible to determine the distance between two incoherent sources regardless how close they are to each other. Similar works have investigated the limitations of these results [28–31]. These contributions lead to concluding that Rayleigh's criterion is an handicap of intensity measurements as imaging technique (direct imaging) and might be overcome using specific measurement strategies.

Given the novel imaging and non-imaging techniques introduced in Chapter 1, a modern description of the resolution limit must be introduced. Using the tools provided by quantum estimation theory it is possible to define a general and fundamental estimation limits regardless the measurement strategy, which allows to redefine the concept of resolution as well as design efficient measurement strategies [32, 33].

In this chapter we introduce the formalism of quantum estimation theory that leads to the definition of estimation precision bounds as well as their applicability and attainability conditions.

2.1 Some concepts of probability and estimation theories

The possible outcomes of a measurement used to determine a parameter θ of a system define a random variable $X(\theta)$ with likelihood function or probability distribution $f(X,\theta)$[1]. We define the *Score* of $X(\theta)$ as the derivative with respect to θ of the logarithmic likelihood[2]:

$$Score \;=\; \frac{\partial}{\partial\theta}\ln f(X;\theta). \tag{2.1}$$

Due to the fact that the probability density function must be normalized, the first moment of the Score function is zero. However, the second moment or variance is not, explicitly

$$F(\theta) = E\left[\left(\frac{\partial}{\partial\theta}\ln f(X;\theta)\right)^2\right] = \int\left(\frac{\partial}{\partial\theta}\ln f(X;\theta\right)^2 f(X;\theta)\,\mathrm{d}X. \tag{2.2}$$

Here $E[\cdot]$ denotes the expectation value integrated over all the possible outcomes of the measurement $X(\theta)$. The quantity in Eq. (2.2) is called *Fisher Information* (FI) and it is non-negative quantity ($0 \leq F(\theta) \leq \infty$) that acts as a measure of the informational content on a random variable X about a certain parameter θ [34]. Note that if the likehood function is twice differentiable, the FI can be written as

$$F(\theta) = -E\left[\frac{\partial^2}{\partial\theta^2}\ln f(X;\theta)\right]. \tag{2.3}$$

Let $\hat{\theta}$ be an estimator of the parameter θ of the system[3] defined as a generalized measurement with expectation value associated to the measurement $X(\theta)$ as:

$$E[X(\theta)] = \int\hat{\theta}\, f(X;\theta)\,\mathrm{d}X. \tag{2.4}$$

[1] $f(X,\theta)$ is considered to be normalized over all the possible outcomes of the measurement as

$$\int f(X,\theta)\,\mathrm{d}X = 1$$

[2] As the probability or likelihood function wants to be maximized it is convenient to use the logarithm as it is a strictly increasing function; maximizing the logarithm is equivalent to maximizing the likelihood function.

[3] For the case of optical metrology, the system is considered to be a sate of light imprinted with information of the parameters of the object after interacting with it.

The measurement X is said to be unbiased if

$$E[X(\theta)] = \theta, \tag{2.5}$$

thus $\hat{\theta}$ is an unbiased estimator. Consider the following quantity

$$E\left[\hat{\theta}(X) - \theta\right] = \int \left(\hat{\theta} - \theta\right) f(X;\theta)\, \mathrm{d}X = 0. \tag{2.6}$$

Using partial integration in the expression above and the fact that the probability density must be normalized, one obtains

$$\int \left(\hat{\theta} - \theta\right)\, f(X;\theta)\, \frac{\partial \log f(X;\theta)}{\partial \theta}\, \mathrm{d}X = 1. \tag{2.7}$$

Squaring and rewriting the expression above, one has

$$1 = \left[\int \left[\left(\hat{\theta} - \theta\right)\sqrt{f}\,\right] \cdot \left[\sqrt{f}\, \frac{\partial \log f}{\partial \theta}\right]\, \mathrm{d}X\right]^2, \tag{2.8}$$

where $f = f(X;\theta)$ is used to avoid notation. Making use of Cauchy-Schwarz inequality, the expression above is transformed to

$$1 \leq \left[\int \left(\hat{\theta} - \theta\right)^2 f(X;\theta)\, \mathrm{d}X\right] \cdot \left[\int \left(\frac{\partial \log f}{\partial \theta}\right)^2 f(X;\theta)\, \mathrm{d}X\right]. \tag{2.9}$$

Notice that the first term on the right hand side of the inequality corresponds to the variance of the estimator i.e. $E[(\hat{\theta}-\theta)^2]$, whereas the second term is the Fisher Information as defined in Eq. (2.2). Thus, the inequality can be expressed as

$$Var(\hat{\theta}) \geq \frac{1}{F(\theta)}. \tag{2.10}$$

The expression in Eq. (2.10) is referred to as the *Cràmer-Rao* (CR) lower bound or inequality [22]. It implies that one can determine a parameter θ using an unbiased estimator $\hat{\theta}$ acting on the measurement outcomes $X(\theta)$ with precision[4] limited by the inverse of the Fisher information. For an optimal estimation of the parameter θ one needs to use an estimator that approaches the lower bound given by expression (2.10). Such an estimator is said to be efficient with a measure of the efficiency ($e(\hat{\theta}) \leq 1$) given by

$$e(\hat{\theta}) = \frac{F(\theta)^{-1}}{Var(\hat{\theta})}. \tag{2.11}$$

[4]We define precision as the degree to which repeated measurements under unchanged conditions show the same result. Precision is reciprocal to the variance.

In analogy to the formalism above presented, for a set of n parameters $\theta \equiv (\theta_1, \theta_2, ..., \theta_N)$ one can define the *Fisher Information Matrix* (FIM) with elements

$$F_{ij}(\theta) = E\left[\left(\frac{\partial}{\partial\theta_i}\ln f(X;\theta)\right)\left(\frac{\partial}{\partial\theta_j}\ln f(X;\theta)\right)\right] \tag{2.12}$$

or equivalently

$$F_{ij}(\theta) = -E\left[\frac{\partial^2 \ln f(X,\theta)}{\partial\theta_i\partial\theta_j}\right]. \tag{2.13}$$

The FIM is a positive definite matrix that defines a Riemaniann metric, which combined with results from differential geometry forms the basis of the Information Geometry [35]. The Fisher information is also a metric used to calculate the informational difference between measurements; it is the infinitesimal form of the relative entropy:

$$g_{ik}(\theta) = \int_X \frac{\partial \log f(X;\theta)}{\partial\theta_i}\frac{\partial \log f(X;\theta)}{\partial\theta_k} f(X;\theta)\,\mathrm{d}X. \tag{2.14}$$

Naturally, making use of the FIM defined in Eq. (2.12), it follows that the variance of any unbiased estimator $\hat{\theta}_i$ of the parameter θ_i is bounded from below by the corresponding element of the inverse FIM as

$$Var(\hat{\theta}_i) \geq \left(F(\theta)^{-1}\right)_{ii}. \tag{2.15}$$

To evaluate the sensitivity of the estimation of the parameters $\theta = (\theta_1, ..., \theta_n)$ from the random variable $X(\theta)$, we consider a Taylor expansion around the mean value θ_0 as

$$\hat{\theta} = X(\theta_0) + (\theta - \theta_0)\Big(\frac{\partial X}{\partial\theta}\Big)\Big|_{\theta_0}. \tag{2.16}$$

Taking the first term on the right-hand side to the left, squaring and taking the expectation value one has that the variance of the measurements distribution is

$$\langle(\hat{\theta} - X(\theta_0))^2\rangle = \langle(\theta - \theta_0)^2\rangle\Big(\frac{\partial X}{\partial\theta}\Big)^2. \tag{2.17}$$

We define the measurement variance $\langle(\Delta X)^2\rangle \equiv \langle(\hat{\theta} - X(\theta_0))^2\rangle$, then

$$\langle(\Delta\theta)^2\rangle = \frac{\langle(\Delta X)^2\rangle}{\left(\frac{\partial X}{\partial\theta}\right)^2}. \tag{2.18}$$

We are interested in the percentage error associated to the parameter estimation, so that we define the error δ standard deviation divided by the mean value:

$$\delta_\theta = \frac{\sqrt{\langle(\Delta\theta)^2\rangle}}{\langle\theta\rangle}. \tag{2.19}$$

Note that, from the CR lower bound in Eq. (2.15), it follows that

$$\delta_{\theta_i} \geq \frac{\sqrt{[F^{-1}]_{ii}}}{\langle\theta_i\rangle}. \tag{2.20}$$

Quantum-mechanical approach to statistical inference and estimation theory

A quantum-mechanical formalism provides two important tools for metrology, a rigorous description of the light-matter interaction scheme, and the probabilistic description of the results of a given measurement. The latter can be treated purely classically while in the former, quantum effects might be taken into account; defining fundamental relations regardless the measurement strategy. The state of the system is assumed to be characterized by a set of parameters $\theta = (\theta_1, ..., \theta_n)$ and it is then considered to belong to a quantum state family $\{\rho_\theta | \theta \in \Theta\}$, further referred as *quantum model*, where Θ is the space of parameters θ.

Formally, let us consider a system defined in the Hilbert space[5] $\mathcal{H}$ such that the state of the system ρ is described by a unit trace ($Tr\rho = 1$)[6] and positive semi-definite[7] Hermitian[8] operator also known as *density matrix*. It is possible to estimate the true state of the system by performing a measurement $M(\theta)$ represented by a *positive operator-valued measure* (POVM) or *probability operator measure* (POM), such that the outcomes f_θ^r define a probability distribution as introduced before.

For a given measurement M one can define an estimator $\hat{\theta}_i^r$ associated to the parameter θ_i of the system with respect to the r-th observation, such that the error associated to the estimation is defined in terms of the covariance matrix as

$$V_{ij}(\hat{\theta}) = \sum_r (\theta_i - \hat{\theta}_i^r)(\theta_j - \hat{\theta}_j^r) f_\theta^r. \tag{2.21}$$

Analogous to Eq. (2.5), the estimator $\hat{\theta} = (\hat{\theta}_1, \hat{\theta}_2, ..., \hat{\theta}_n)$ is said to be unbiased if the following expression is satisfied

$$\sum_r \hat{\theta}_i^r f_\theta^r = \theta_i. \tag{2.22}$$

For any unbiased estimator $\hat{\theta}$, the trace of the covariance matrix in Eq. (2.21) is the sum of the mean square errors of the estimators with respect to their corresponding parameters. Similar to Eq. (2.15), it follows that the covariance matrix is bounded from bellow as

$$[V(\hat{\theta})]_{ij} \geq [F(\theta)]_{ij}^{-1}, \tag{2.23}$$

where F_{ij} is the *Classical Fisher Information Matrix* given by

$$F_{ij} = \sum_r \left(\frac{\partial \log f_\theta^r}{\partial \theta^i} \right) \left(\frac{\partial \log f_\theta^r}{\partial \theta^j} \right) f_\theta^r. \tag{2.24}$$

[5] Linear space $\mathcal{H}$ with a defined inner product s.t. for $\psi, \phi \in \mathcal{H}$, and $\hat{O}$ a linear operator, then $(\phi|\hat{O}\psi) = (\hat{O}^\dagger\phi|\psi)$ and $Tr\hat{O} = \sum_j (\phi_j, \hat{O}\psi_j)$ for $\{\psi_j\}$ a basis of $\mathcal{H}$.

[6] Equivalent to the normalization of the probability distribution.

[7] $\hat{O}$ is positive definite if $\psi|\hat{O}\psi) \geq 0$ for all ψ nonzero.

[8] $\hat{O}$ is an Hermitian operator if $\hat{O} = \hat{O}^\dagger$

Equation (2.23) is a more general matrix form of Eq. (2.15) the *Crámer-Rao inequality* or *Cràmer-Rao Lower Bound*. It defines the precision in the measurement of θ given the corresponding estimator $\hat{\theta}$; it must be understood in matrix form implying that the matrix $[V(\hat{\theta}) - F^{-1}]$, is positive semidefinite[9]. The term "classical" in the name of the quantity above, relates to the fact that it comes from the standard probability theory, containing no quantum-mechanical effects nor considerations besides the formalism hereby presented.

2.2 Quantum Estimation Theory

Using a quantum-mechanical formalism, one can obtain a generalization of the concepts introduced in Section 2.1, with the aim of finding fundamental estimation bounds for the parameters characterizing a system, that would apply to any measurement strategy. More precisely, the goal is to obtain a quantum version of the Crámer-Rao inequality, which requires a description of the Fisher information in a quantum-mechanical scenario. [23, 36]

Let us start by considering a quantum state in density matrix representation depending on a set of n parameters ρ_θ. Given the operator nature of the density matrix, the commutativity between operator has to be verified. Thus, the quantum analogue of the FIM in Eq. (2.24) has to be defined in the frame of *non-commutative probability theory* [37]. A general logarithmic derivative operator K is defined such that it satisfies the following expression:

$$\frac{\partial \rho}{\partial \theta_i} = \frac{1}{2}\left(\rho K_i + K_i^\dagger \rho\right). \tag{2.25}$$

The Quantum version of the FIM, equivalent to equation (2.24) must be then defined for a given logarithmic derivative operator K satisfying (2.25). Since eventually a measurement will be carried out, the accuracy of the estimator $\hat{\theta}$ is more generally defined in terms of weight fields associated to each parameter as

$$Tr[GV] = \sum_{ij} G_{ij} V^{ij}. \tag{2.26}$$

Here and in what follows, the dependency of the matrix on the estimator is no longer explicitly written for the sake of simplifying notation ($V(\hat{\theta}) = V$). The matrix $G \in \mathcal{R}^{n\times n}$ is a positive-definite matrix, containing weight fields in the diagonal. A generalization of the Cràmer-Rao inequality, considering the weight fields matrix G is

$$Tr[GV] \geq C, \tag{2.27}$$

where $Tr[A]$ refers to the trace of the matrix A, and C is a lower bound of the Crámer-Rao type, also referred to as Crámer-Rao-like lower bound. In what follows, we refer as CR lower bound to the generalization in Eq. (2.27).

[9]The matrix $R \in \mathbb{C}^{n\times n}$ is positive semidefinite if: $u^T R\, u \geq 0,\ \forall\, u \in \mathbb{C}^n \neq 0$.

Note that the CR bound is not unique, it depends on the assumptions and properties of the quantum state, the model and selection of the logarithmic derivative operator; as well as the weight fields matrix. Thus, the aim is to obtain the *Most Informative Cràmer-Rao* (MICR) bound C^{MI} defined as the maximum of all the CR bounds for the estimator $\hat{\theta}$ [38]; namely

$$C^{MI} := \min\left\{Tr[GV(\hat{\theta})]\right\}. \tag{2.28}$$

Solving the minimization problem to find the C^{MI} is in general cumbersome. However, in some cases it is rather simple since there are several expressions that have been proved under certain conditions to be tight and the most informative.

2.2.1 Towards finding the most informative precision bound

To find the MICR bound, several considerations are proposed, some related to the Quantum version of the FIM[10] defined in terms of the logaritmic derivative operator K in equation (2.25). The hermiticity of the operators K and its commutativity with the density matrix ρ define two particular logarthmic derivative operators.

Right Logarithmic Derivative Operator bound

Consider a logarithmic derivative operator L^R that commutes with the density matrix, this is $[L_i^R, \rho] = 0$ for all $i \in [1, n]$. Equation (2.25) is reduced to

$$\frac{\partial \rho}{\partial \theta_i} = \rho L_i^R. \tag{2.29}$$

L_i^R is known as the *Right Logarithmic Derivative* (RLD) operator with respect to the estimation of the parameter θ_i. The FIM defined in terms of L^R is

$$[F_Q]_{ij}^R = Tr\left[\rho L_i^R (L_j^R)^\dagger\right]. \tag{2.30}$$

From Eq. (2.27) it follows that the CR bound is [38]

$$C^R = Tr\Big[G\ \mathrm{Re}\left\{[F_Q^R]^{-1}\right\} + \mathrm{abs}\left[G\ \mathrm{Im}\left\{[F_Q^R]^{-1}\right\}\right]\Big], \tag{2.31}$$

where $\mathrm{abs}[A] = T\,\mathrm{diag}(|a_1|, |a_2|, ..., |a_n|)\,T^{-1}$, and $\mathrm{diag}(|a_1|, |a_2|, ..., |a_n|)$ is the diagonal matrix with elements $|a_i|$, and T a matrix satisfying

$$A = T\,\mathrm{diag}(a_1, a_2, ..., a_n)\,T^{-1}. \tag{2.32}$$

[10] The direct computation of the FIM is introduced in Sec. 2.2.2

Symmetric Logarithmic Derivative Operator bound

Consider now a Hermitian logarithmic derivative operator ($L^S = K = K^\dagger$) that does not commute with the density matrix. Eq. (2.25) reduces to

$$\frac{\partial \rho}{\partial \theta_i} = \frac{1}{2}\left(\rho L_i^S + L_i^S \rho\right). \tag{2.33}$$

L^S is known as the *Symmetric Logarithmic Derivative* (SLD) operator. Using L^S, the quantum FIM is

$$[F_Q^S]_{ij} = \frac{1}{2} Tr\left[\rho(L_i^S L_j^S + L_j^S L_i^S\right] = \mathrm{Re}\left\{Tr\left[\rho\, L_i^S L_j^S\right]\right\}. \tag{2.34}$$

From the expression above, F_Q^S is a real valued matrix; thus, one can consider an extension to the FIM beyond the SLD by considering

$$F_Q = F_Q^S + i\tilde{F_Q}, \tag{2.35}$$

where $F_Q^S = \mathrm{Re}[F_Q]$ and $\tilde{F_Q} = \mathrm{Im}[F_Q]$. From Eq. (2.33) and (2.34), it is possible to see that $\tilde{F_Q}$ results from the non-symmetric part of the SLD operator L^S, thus

$$[\tilde{F_Q}]_{ij} = \frac{i}{2}\mathrm{Tr}[\rho(L_i^S L_j - L_j^S L_i^S)]. \tag{2.36}$$

Note that for a pure state $\rho = |\Psi\rangle\langle\Psi|$ and $\mathrm{Tr}[\rho] = 1$, the Quantum FIM (2.34) is reduced to [36]

$$[F_Q]_{ij} = 4\,\mathrm{Re}\left\{\left\langle \frac{\partial\Psi}{\partial\theta_i}\middle|\frac{\partial\Psi}{\partial\theta_j}\right\rangle - \left\langle\frac{\partial\Psi}{\partial\theta_i}\middle|\Psi\right\rangle\left\langle\Psi\middle|\frac{\partial\Psi}{\partial\theta_j}\right\rangle\right\}. \tag{2.37}$$

The CR bound associated to the Symmetric Logarithmic Derivative Fisher Information Matrix F_Q^S is

$$C^S = Tr\left[G[F_Q^S]^{-1}\right]. \tag{2.38}$$

In particular, if:

$$\tilde{F_Q} = 0 \qquad \text{or equivalently} \qquad [L_i, L_j] = 0, \tag{2.39}$$

the inverse of the quantum FIM F_Q^S is a lower bound [39,40]. In the case of a single parameter, the CR bound can be asymptotically saturated [22,41]; this means that the bound is attainable and it is the most informative. For the case of pure states, this happens if [21, 42]:

$$\mathrm{Im}\langle\partial_i\Psi|\partial_j\Psi\rangle = 0, \tag{2.40}$$

for all $i, j = 1...d$, which is equivalent to

$$\mathrm{Im}\langle\partial_i\Psi|\partial_j\Psi\rangle \Longrightarrow \langle\partial_i\Psi|\partial_j\Psi\rangle = \langle\partial_j\Psi|\partial_i\Psi\rangle. \tag{2.41}$$

The Coherent model bound

A quantum model $\{\rho_{\boldsymbol{\theta}}\}$ such that all the eigenvalues of the matrix $D \equiv [F_Q^S]^{-1}\tilde{F}_Q$ are $\pm i$ is said to be coherent. This condition is satisfied if $|\det F_Q^S| = |\det \tilde{F}_Q|$. For a two-parameter estimation problem, the RLD bound in Eq. (2.31) is a lower bound and it can be estimated by means of the following expression [43, 44]

$$C^C = C^S + \frac{\sqrt{\det G}}{\det F_Q^S}\left|\mathrm{Tr}\{\rho[L_1^S, L_2^S]\}\right| \tag{2.42}$$

For a pure state model this bound is shown to be the most informative [38]. Furthermore, if one writes the matrix $D \equiv {F_Q^S}^{-1}\tilde{F}_Q$ in its spectral decomposition form with eigenvalues α_i, the following expression defines a bound

$$C^M = \sum_{\alpha_i \in \{\text{spec. of D}\}} \frac{2}{1 + (1 - |\alpha_i|^2)^{1/2}} \tag{2.43}$$

C^M is further refered as Matsumoto bound [39].

The Holevo bound

Consider the vector $\vec{X} = (X^1, ..., X^n)$ with X^i linear Hermitian operators satisfying $Tr[\rho X^i] = 0$ and $Tr[\partial_i \rho X^j] = \delta_{ij}$ [38]. The Holevo function is defined as

$$h_\theta(\vec{X}, G) = \mathrm{Tr}\Big\{G\,\mathrm{Re}\,Z_\theta[\vec{X}]\Big\} + \mathrm{Tr}\,\mathrm{abs}\left\{\sqrt{G}\,\mathrm{Im}\,Z_\theta[\vec{X}]\sqrt{G}\right\}, \tag{2.44}$$

with $Z_\theta[\vec{X}]$ the $n \times n$ complex matrix with elements $X^{jk} = Tr\{\rho X^j X^k\}$ [45]. By minimization of the Holevo function, the Holevo bound is defined as

$$C^H = \min\{h_{\boldsymbol{\theta}}(\vec{X}, \boldsymbol{G}) | \vec{X} \in X_{\boldsymbol{\theta}}\}. \tag{2.45}$$

The precision of any locally unbiased estimator is bounded by the Holevo bound as in equation (2.27). By definition $C^H \geq C^i$ for any other bound (C^S, C^C). More importantly, this bound is know to be asymptotically attained by an asymptotically unbiased estimator with a collective POVM [46–49].

All the bounds presented above C^R, C^S, C^C, C^M and C^H are bounds of the Cràmer-Rao type. For a given quantum state model ρ_θ these bounds can be computed, providing information about the fundamental limitations for estimating the parameters that characterize a system; however, not all of them are tight bounds.

2.2.2 Computation of the Quantum Fisher Information Matrix

An important quantity to evaluate the CR lower bounds above mentioned is the FIM. To give an expression for it, consider quantum state depending on the set of

parameter θ in its density matrix representation ρ_θ. The state can be written as its spectral decomposition; this is, a linear combination of eigenstates that span its Hilbert space, explicitly

$$\rho_\theta = \sum_k p_k |\varphi_k\rangle\langle\varphi_k|, \tag{2.46}$$

with p_k and φ_k are the eigenvalues and eigenvectors of the density operator, respectively. Notice that p_k and $|\varphi_k\rangle$ depend on the set of parameters θ; however, in order to avoid notation, we omit the explicit dependence. Using Eq. (2.46) in Eq. (2.33), and assuming it to be differentiable one can see that equation (2.33) has solutions

$$L_i = 2 \sum_{p_k+p_l>0} \frac{1}{p_k + p_l} \langle\psi_k| \frac{\partial\rho}{\partial\theta_i} |\psi_l\rangle |\psi_k\rangle \langle\psi_l| \tag{2.47}$$

which can also be written as as [36]:

$$[L_i]_{kl} = \frac{1}{p_k}\frac{\partial p_k}{\partial\theta_i}\delta_{kl} + \frac{2(p_k - p_l)}{p_k + p_l}\langle\frac{\partial\psi_k}{\partial\theta_i}|\psi_l\rangle. \tag{2.48}$$

Thus, the Quantum FIM F_Q reduces to [50, 51]

$$[F_Q]_{ij} = \sum_{m,n} \frac{2}{p_m + p_n}\langle\varphi_n|\frac{\partial\rho}{\partial\theta_i}|\varphi_m\rangle\langle\varphi_m|\frac{\partial\rho}{\partial\theta_j}|\varphi_n\rangle, \tag{2.49}$$

which for a one-dimensional model the FI is reduced to

$$F_Q = \sum_{m,n} \frac{2}{p_m + p_n}\left|\langle\varphi_n|\frac{\partial\rho}{\partial\theta}|\varphi_m\rangle\right|^2. \tag{2.50}$$

If the state is pure ($\rho = \langle\Psi\,|\Psi\rangle$) the spectral decomposition is straightforward and the elements of the FIM matrix are [40]

$$[F_Q]_{ij} = 4\,\mathrm{Re}\left[\langle\frac{\partial\Psi}{\partial\theta_i}|\frac{\partial\Psi}{\partial\theta_j}\rangle - \langle\frac{\partial\Psi}{\partial\theta_j}|\Psi\rangle\langle\Psi|\frac{\partial\Psi}{\partial\theta_i}\rangle\right], \tag{2.51}$$

which in the single parameter estimation case it reads

$$F_Q = 4\,\mathrm{Re}\left\{\langle\frac{\partial\Psi}{\partial\theta}|\frac{\partial\Psi}{\partial\theta}\rangle - \left|\langle\Psi|\frac{\partial\Psi}{\partial\theta}\rangle\right|^2\right\}. \tag{2.52}$$

This procedure is useful when the spectral decomposition of the density matrix is simple. Although this is not always simple, it can be achieved using computational methods.

Lyapunov representation

An alternative solution to give an expression for the SLD operator comes by noticing that Eq. (2.33) is a special form of Lyapunov equation, with a known solution given by

$$L_{ij} = 2\int_0^\infty Tr\Big[e^{-\rho s}\frac{\partial\rho}{\partial\theta_i}e^{-\rho s}\frac{\partial\rho}{\partial\theta_j}\Big]\mathrm{d}s. \tag{2.53}$$

The main advantage of this representation is that it is basis independent; however the required operations (exponentiation and integration) are in general not so simple [52].

Safranek method

When the diagonalization of the density matrix is too costly or Lyapunov equation for the SLD operator too difficult to solve due to the complexity of the exponentiation and integration of the density operator; there exists a different method that allows to give an expression of the Quantum FIM matrix without the need of the previously mentioned operations [53]. The method is as follows:

- If ρ is invertible:
  The Quantum FIM elements can be written as

  $$[F_Q]_{ij} = 2vec(\partial_i\rho)^\dagger M^{-1} vec(\partial_j\rho) \tag{2.54}$$

  and the SLD matrix elements as

  $$vec[L_i] = 2M^{-1}vec\left[\partial_i\rho\right]; \tag{2.55}$$

  where $M \equiv (\rho^* \otimes I + I \otimes \rho)$ is an invertible matrix as a consequence of ρ being invertible; $vec[\cdot]$ represents the vectorization of a matrix, defined as the concatenation of the columns altogether in a column vector; ∂_i is the partial derivative with respect to θ_i, ρ^* is the complex conjugate of the density matrix and the $\dagger$ symbol represents the usual the conjugate transpose operator.

- If ρ is singular
  It is possible to construct an auxiliary matrix ρ_ν as:

  $$\rho_\nu = (1-\nu)\rho + \frac{\nu}{\dim H}I \tag{2.56}$$

  which is invertible by definition. The Fisher Information Matrix A is then defined as

  $$[F_Q]_{ij} = \lim_{\nu\to 0} 2vec(\partial_i\rho_\nu)^\dagger M^{-1} vec(\partial_j\rho_\nu). \tag{2.57}$$

Fisher Information and statistical distance between quantum states

Since the FI gives a measure of the precision when characterizing a quantum state through estimation of its parameters, it is also useful to measure the distance between two states in the corresponding Hilbert space. Consider two quantum states described by the density operators ρ_1 and ρ_2; both of them depending on the n-dimensional sets of parameters $\{\theta_1\}$ and $\{\theta_2\}$. A way to measure the distinguishability between them is through the Bures distance [54]

$$d_B^2(\rho_1, \rho_2) = 2\left[1 - \sqrt{U_F(\rho_1, \rho_2)}\right], \tag{2.58}$$

where $U_F(\rho_1, \rho_2)$ is the Uhlmann fidelity [55] defined as

$$U_F(\rho_1, \rho_2) = Tr\left[\sqrt{\sqrt{\rho_1}\rho_2\sqrt{\rho_1}}\right]^2. \tag{2.59}$$

The Bures distance allows to define a line element d_B^2 by the statistical distance between the state ρ_θ (determined by the parameters θ) and the state $\rho_{\theta+d\theta}$ produced by a differential change in the parameter θ, namely[11]

$$d_B^2(\rho_\theta, \rho_{\theta+d\theta}) = \sum_{ij} g_{ij} d\theta_i d\theta_j, \tag{2.60}$$

with $g_{\mu\nu}$ the Bures metric measuring the distinguisability between two states in the coordinate system of the parameters θ. The Bures metric and the Quantum FIM are often related by

$$F_Q \approx 4g. \tag{2.61}$$

However, in some cases the previous relation does not hold due to singularities where the rank of the density matrix changes, a more general expression is given by [56]

$$[F_Q]_{ij}(\theta) = 4g_{ij}(\theta) - 2\sum_{p_k(\theta)=0} \partial_{ij} p_k(\theta), \tag{2.62}$$

where $p_k(\theta)$ is the k-th coefficient of the spectral decomposition of the density matrix in Eq. (2.46) and the sum[12] goes over all the k whose eigenvalue vanish at the point θ in the parameter coordinate space.

Summary of QET formalism tools

Quantum estimation theory and statistical inference theory provide the tools to define bounds that determine how precisely one can estimate the parameters of

[11] Without lose of generality only one parameter has been considered to avoid notation, however the generalization is straightforward.

[12] Note that the argument of the sum is the Hessian matrix.

a system. On the one hand, a quantum-mechanical description of the system naturally leads to a fundamental limitation for its characterization. A way to quantify this limitation is the study of the variation of the informational content of the state with respect to the parameters; this leads to the Crámer-Rao inequality, stating that the variance on the estimation of the parameters of the system is bounded. In this section we have introduced several bounds and mechanisms to calculate them.

On the other hand, when performing a measurement on the state or the system, the probability distribution of the outcomes of the measurement has also associated a bound for the estimation precision. With these two components, it is of interest to find a measurement strategy whose bound is either equal or at least asymptotically approaches the fundamental bound obtain by means of the quantum-mechanical formalism in the frame of quantum estimation theory. If this is not possible, by comparing the difference between the fundamental and the experimentally-obtainable bounds it is also possible to indicate how efficient a measurement strategy is.

In the following, in Section 2.3 we evaluate with an example the values of different bounds presented in this section, showing their validity and applicability as well as their attainability. In Section 2.4 we show that the lower bounds depend on the quantum state model selection and in Section 2.5 we study the effects of lossy environments in the informational content of a quantum state.

2.3 Comparisson between different lower bounds

The true bound for Quantum Lidar Systems

As introduced in the previous section, there exist several CR (CR-type) lower bounds, and different methods to compute them. Some of them by means of computing the FIM, and others by explicitly solving a minimization problem. To study the differences between those bounds, as well as their validity and applicability, we consider the particular case of quantum lidar system.

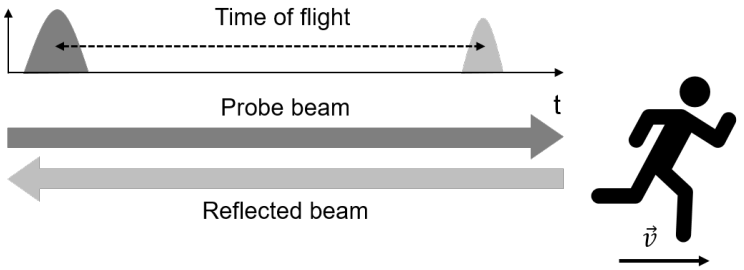

Figure 2.1: Operation principle of Lidar Systems. A pulse of light is reflected by a moving target. The position and speed of the target are determined by the time taken for the pulse to arrive to the sensor and its frequency shift.

A lidar is an optical system used to determine the position at a given time and the radial velocity of a moving target by measuring the Doppler shift of the reflected light as shown in Fig. 2.1. In this section we illuminate the concepts introduced in the previous section, by computing explicitly the CR-like lower bounds and evaluating their validity in the frame of a quantum lidar system; when using a quantum state of entangled photons for simultaneous estimation of the parameters of interest. Two aspects are particularly interesting in this example. First, in the frame of parameter estimation, the measured quantities (time delay and frequency shift) and the parameters to estimate (position and radial velocity) are associated to canonical conjugated variables; meaning that the estimation of the parameters is coupled. Second, we take advantage of the quantum-mechanical formalism to exploit the non-classical phenomena related to quantum correlations using pairs of entangled photons.

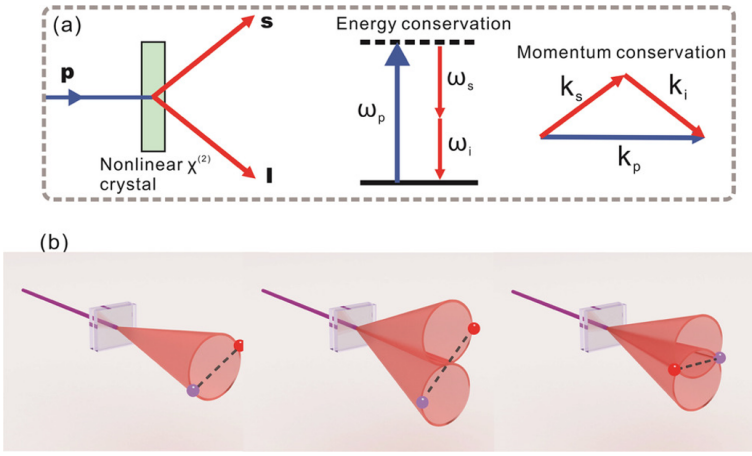

Figure 2.2: Entangled photon pairs generation. a) Schematic Spontaneous Parametric Down Conversion (SPDC) process. b) From left to right: degenerate type I SPDC, collinear type II SPDC, and noncollinear type II SPDC. Figure from Ref. [57].

Consider a lidar system in which the probing light waves are composed by photon pairs generated by spontaneous parametric down-conversion (SPDC). The signal and idler photons are considered to be entangled in frequency as shown in Fig. 2.2 (a). The state of the SPDC photon pairs can be written as

$$\Psi_{in}(t_s, t_i) = N \exp\left[-a^2(t_s + t_i)^2 - b^2(t_s - t_i)^2 \; - i\omega_s^0 t_s - i\omega_i^0 t_i\right], \qquad (2.63)$$

where $t_{s,i}$ are time coordinates and $\omega_{s,i}^0$ are the central frequencies of the signal and idler photons, respectively. The normalization constant depends on the correlation time of the photons and the coherent time of the pump field as $N = 1/\sqrt{2\pi\sigma_{coh}\sigma_{cor}}$. The parameters a and b are associated to the temporal and frequency widths of the photons as $T = \sqrt{\frac{1}{16a^2} + \frac{1}{16b^2}}$ and $W = \sqrt{a^2 + b^2}$. These parameters

determine the quantum nature of the state as it can be factorized as product state $\Psi(t_s, t_i) = \Phi_s(t_s)\Phi_i(t_i)$ only if $a = b$. If that is not the case, then the state (2.63) is said to be non-separable or entangled [58].

The idler photon travels for a time τ_i before detection whereas signal photon interacts with the target located at a certain distance $x_s = c\tau_s/2$ moving at velocity v. Due to the movement of the target, the scattered signal photon suffers a Doppler shift δ. After the interaction the state is written as

$$\Psi(t_s, t_i) \propto \exp \quad \left\{-a^2(t_s - \tau_s + t_i - \tau_i)^2 - b^2(t_s - \tau_s - t_i + \tau_i)^2 - i\omega_s^0(t_s - \tau_s) \right. \\ \left. -i\omega_i^0(t_i - \tau_i) - i\delta(t_s - \tfrac{\tau_s}{2})\right\}. \tag{2.64}$$

Note that the state depends on the two unknown parameters associated to non-commuting variables: the temporal delay τ_s and the Doppler shift δ containing information of the position and velocity of the moving target.

The uncertainty relation for the two canonical conjugated variables in an standard Lidar system is given by the Arthurs-Kelly relation $\sigma_\tau \sigma_\delta \geq 1$, [59, 60] where σ_τ and σ_δ correspond the respective RMS errors of the simultaneously measured variables. The aim of this work is to find a quantum analogue using the state in Eq. o(2.64) and a quantum-mechanical formalism.

2.3.1 Cràmer-Rao lower bounds

Using the concepts introduced in Section 2.2, given the particular characteristics of the system under study defined by the quantum state (2.64); we compute explicitly four bounds: the one based on the SLD operator C^S, the coherent model bounds C^C and C^M, and the Holevo bound C^H.

CR bound based on SLD and FIM

Using the state (2.64) with its corresponding normalization constant ensuring $\langle\Psi|\,\Psi\rangle = 1$. For the parameter vector $\theta = (\theta_1, \theta_2) = (\delta, \tau_s)$, the real and imaginary parts of the FIM in Eq. (2.38) using Eq. (2.37) are:

$$F_Q^S = \begin{pmatrix} 4W^2 & 0 \\ 0 & 4T^2 \end{pmatrix} \quad \text{and} \quad \tilde{F_Q} = \begin{pmatrix} 0 & 2 \\ -2 & 0 \end{pmatrix}. \tag{2.65}$$

Note that as $[\tilde{F_Q}]_{ij} \neq 0 \ \forall i, j$ the bound C^S is not attainable. Without losing generality, one can choose a weight field matrix $G = \mathrm{diag}[W^2, zT^2]$, with $z > 0$, the Cràmer-Rao bound from Eq. (2.38) is reduced to

$$C^S = \frac{1+z}{4}. \tag{2.66}$$

CR bound for coherent model

From Eq. (2.65) one can see that the conditions for the model to be coherent (i.e $|\det F_Q^S| = |\det \tilde{F}_Q|$) are satisfied only if $TW = 1/2$ since $\det F_Q^S = 16W^2T^2$ and

$\det\left(\tilde{F_Q}\right) = 4$. However, for the sake of comparison of the bounds we calculate it form Eq. (2.42) using the same weight field matrix as before, explicitly, (valid only for $TW = 1/2$) it becomes

$$C^C = \frac{1+z}{4} + \frac{\sqrt{z}}{2}. \tag{2.67}$$

CR bound by Matsumoto

Using a weight field matrix $G = F_Q^S$ one can compute the Matsumoto bound explicitly by diagonalizing matrix $D = [F_Q^S]^{-1}\tilde{F}_Q$ are $\alpha = \pm\frac{i}{2TW}$. The bound C^M from Eq. (2.43) is explicitly

$$C^M = \frac{2TW}{2TW + \sqrt{4T^2W^2 - 1}}. \tag{2.68}$$

Note that the eigenvalues of D are $\pm i$ if $TW = 1/2$, making the model to be coherent thus $C^M = C^C$.

CR Holevo bound

By definition $C^H \geq C^i$ for any other bound (C^S, C^C, C^M). More importantly, this bound is know to be asymptotically attained by an asymptotically unbiased estimator with a collective POVM [46–49]. The explicit computation of the Holevo bound by means of the minimization of the Holevo function is reported in appendix A. The result obtained is:

$$C^H = 2WT\left(2WT - \sqrt{4T^2W^2 - 1}\right). \tag{2.69}$$

2.3.2 Minimum indeterminacy bound

It is of interest of this section to evaluate the precision bounds for estimation of the parameters of a system. In this case, the advantages that the quantum properties of the state provide with respect to the classical counterpart. A way to quantify these advantages is by estimating the improvement that a quantum system could allow in terms of estimation precision by comparing the fundamental and attainable bounds from quantum estimation theory to the classical ones. We study the quantum analogue of the Arthurs-Kelly relation [59] giving a lower bound for the precision of the simultaneous measurement of a pair of conjugated variables. The relation has the form

$$V(\delta)V(\tau_s) \geq \sigma^i, \tag{2.70}$$

where the left hand side of the inequality corresponds to the product of the diagonal elements of the covariance matrix V from Eq. (2.21) and σ^i is the chosen bound C^i.

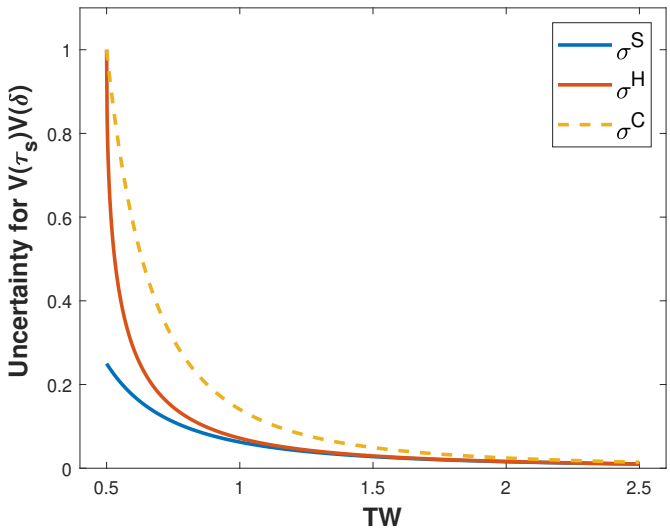

Figure 2.3: Uncertainty lower bound for the product of variances $V(\tau_s)V(\delta) \geq \sigma^i$. The blue line corresponds to the SLD CR bound, a valid bound however not generally attainable. The orange line represents the Matsumoto bound σ^M which coincides with the Holevo bound (most informative) σ^H. Note that for $TW = 1/2$ the Holevo CR bound and the bound of the Coherent model bound σ^C coincide, even though this is not a valid bound, we plot it in dashed yellow here for the sake of comparison.

To obtain the the optimum measurement we consider the minimization of the product of variances using the Cràmer-Rao inequality (2.27); which can be written as

$$g = C^i(z) - W^2 V(\tau_s) - zT^2 V(\delta) \leq 0, \tag{2.71}$$

for $C^i \in \{C^S, C^C, C^M, C^H\}$ and G as above. Using the expression (B.26) for the bound from Appendix B, equation (2.70) is reduced to

$$V(\tau_s)V(\delta) \geq \frac{C^i(z_0)^2}{4(WT)^2 z_0}. \tag{2.72}$$

For z_0 satisfying the minimization condition $2z_0 \left.\frac{dC^i(z)}{dz}\right|_{z=z_0} = C^i(z_0)$. When substituted in Eq.(2.72) each of the expressions for $C^i(z)$ presented in Section 2.3.1 will provide a different bound for the product $V(\tau_s)V(\delta)$; however the Holevo bound C^H is known to be the most informative as $C^H \geq C^i, \forall\, C^i$.

The objective at this point is to compare these bounds to the Arthurs-Kelly relation (2.70) to determine whether the Quantum Lidar offers any advantages over the standard Lidar system.

- Symmetric Logarithmic Derivative bond C^S

$$V(\tau)V(\delta) \geq \frac{1}{16T^2W^2}. \tag{2.73}$$

- Coherent model bound C^C (valid only for $TW = 1/2$)

$$V(\tau)V(\delta) \geq \frac{(1+2TW)^2}{64T^2W^2}. \tag{2.74}$$

- Holevo bund C^H

$$V(\tau)V(\delta) \geq \left(2TW - \sqrt{4T^2W^2 - 1}\right)^2. \tag{2.75}$$

Note that the bound in (2.75) is equivalent when using the Matsumoto bound C^M in equation (2.68), hence $\sigma^H = \sigma^M$. Figure 2.3 shows how each of this bounds behaves as a function of the product TW, which is related to the degree of entanglement between the signal and idler photons as it determins the separability of the two-photon quantum state in Eq. (2.64).

There are essentially two remarks to extract from this figure. First, for a separable (non-entangled) state ($TW = 1/2$), the Holevo bound coincides with the classical Arthurs-Kelly relation $V(\tau_s)V(\delta) \geq 1$, as expected. Second, as $TW \to \infty$ the uncertainty in the product tends to zero. This means the uncertainty reduces as the correlation between the photons increases.

2.4 Precision bound dependence with quantum state model selection

Single photon Vs multimode coherent model

The results presented in Section 2.2 for the determination of estimation precision bounds have been widely applied to metrology. In particular, for estimation of phases of a quantum state, the CR lower bound given by the inverse FIM is attainable and most informative. These results are often used for optical sensing to determine the fundamental precision limit when estimating the characteristic parameters of phase objects, imprinting phase changes to probe beams. In this section, we demonstrate that the limit given by the Cámer-Rao lower bound depends on the selection of the quantum state model. This corresponds to original work that has been submitted to a peer reviewed journal as a research article (Ref. [61]) of which the author of this dissertation is first author. By the time this dissertation was written the article is under revision for publication.

Multi-phase estimation bounds for to different photonic state models

Most of the works investigating the ultimate resolution limit dictated by the quantum Cramér-Rao bound consider imaging of incoherent point-like sources [26,30,62,63]. In most cases the theoretical analysis is made considering N copies of a single-photon state, while experiments are done using intense or attenuated laser sources [64]. This experimental scheme is based on the following arguments [65]:

> *"Considering thermal sources at optical frequencies, we divide the total emission time into short coherence time intervals τ_c, so that within each interval the sources can be assumed weak, i.e., effectively emitting at most one photon...it allows us to describe the quantum state ρ of the optical field on the image plane as a mixture of a zero-photon state ρ_0 and a one-photon state ρ_1 in each time interval (neglecting contributions from higher photon numbers)".*

Another common assumption is that [66]

> *"the probability of more than one photon arriving at the image plane is negligible".*

Moreover, in Ref. [62] the authors state that

> *"(...) although this ultimate resolution follows from the quantum Crámer-Rao lower bound, the quantum nature of light plays no role".*

In most other situations one is interested in using coherent illumination for imaging and optical metrology, then it is necessary to determine the ultimate resolution limits for coherent illumination. This led us to consider in a more detailed way the applicability of the above mentioned claims regarding the relevance of the quantumness of the illumination from a metrology perspective.

In this section we study whether the use of a coherent multimode state with average number of photons N and shape $f(x)$ (where x can designate space or frequency variable) leads to equivalent results than when considering N copies of a single-photon state with the same shape $f(x)$. This analysis is relevant either from a fundamental or practical point of view, since it defines differences/similarities between the two states directly from their quantum nature, and it allows us to determine whether the Crámer-Rao lower bound using a single-photon model is applicable for experiments using conventional (coherent multimode) laser illumination.

Consider the case of the estimation of the phase parameters characterizing an optical beam; for instance the phase gained after propagation through a non absorbing medium or after interacting with a phase object, i.e., an object that introduces a phase shift $\varphi(x, \theta_i)$ to the illumination beam after interaction. It is worth mentioning that for this phase shift, the variable (x) can represent any degree of freedom of interest, for instance, frequency, time, spatial coordinates, or even transverse momentum. In the following, without lose of generality we will assume x to be the spatial variable.

For this particular case of a pure state model, the CR lower bound is tight and attainable, is given by the inverse FIM (2.38). In what follows, we present explicit expressions of the FIM and CR precision bound for estimation of multi-phases using 1) a multimode coherent state and 2) multiple copies of a single-photon state.

2.4.1 Case I: Multimode coherent state with average photon number N

We describe a multimode coherent state in terms of single mode states

$$|\alpha_i\rangle = D(\alpha_i)|\text{vac}\rangle = \exp\left(\alpha_i \hat{a}_i^\dagger - \alpha_i^* \hat{a}_i\right)|\text{vac}\rangle, \tag{2.76}$$

where $D(\alpha_i)$ is the displacement operator and the mode normalization $\langle\alpha_i|\alpha_i\rangle = 1$ holds. The multimode coherent state with mean photon number $N = \sum_{i=1}^{N} |\alpha_i|^2$ is given by

$$\begin{aligned} |\alpha\rangle &= |\alpha_1\rangle ... |\alpha_N\rangle = D(\alpha_1)...D(\alpha_N)|\text{vac}\rangle \\ &= \exp\left(\alpha_1 a_1^\dagger - \alpha_1^* a_1\right) ... \exp\left(\alpha_N a_N^\dagger - \alpha_N^* a_N\right)|\text{vac}\rangle \\ &= \exp\left[\alpha_1 a_1^\dagger + ... + \alpha_N a_N^\dagger - \alpha_1^* a_1 - ... - \alpha_N^* a_N\right]|\text{vac}\rangle. \end{aligned} \tag{2.77}$$

The inner products in Eq. (2.51) in this case take the form

$$\langle \partial_i \Psi | \partial_j \Psi \rangle = \sum_k \langle \frac{\partial \alpha_k}{\partial \theta_i} | \frac{\partial \alpha_k}{\partial \theta_j} \rangle + \sum_{k \neq k'} \langle \frac{\partial \alpha_k}{\partial \theta_i} | \alpha_k \rangle \langle \alpha_k | \frac{\partial \alpha_k}{\partial \theta_j} \rangle, \tag{2.78}$$

and

$$\langle \Psi | \partial_i \Psi \rangle = \sum_k \langle \alpha_k | \frac{\partial \alpha_k}{\partial \theta_i} \rangle. \tag{2.79}$$

The FIM of the multimode state can be written as the sum of the FIM of each mode, namely

$$[F_Q^{Coh}]_{ij} = \sum_k [F_Q^{SM}]_{ij}^k, \tag{2.80}$$

where

$$[F_Q^{SM}]_{ij}^k = 4\langle \partial_i \alpha_k | \partial_j \alpha_k \rangle + 4\langle \alpha_k | \partial_i \alpha_k \rangle \langle \alpha_k | \partial_j \alpha_k \rangle. \tag{2.81}$$

For a coherent state, the derivative with respect to its phase parameters is given by [67]:

$$|\frac{\partial \alpha_k}{\partial \theta_i}\rangle = i\alpha_k \left(\frac{\partial \varphi_k}{\partial \theta_i}\right) a_k^\dagger |\alpha_k\rangle. \tag{2.82}$$

Then the inner products in Eq. (2.81) become

$$\langle \frac{\partial \alpha_k}{\partial \theta_i} | \frac{\partial \alpha_k}{\partial \theta_j} \rangle = |\alpha_k|^2 \left(\frac{\partial \varphi_k}{\partial \theta_i}\right)\left(\frac{\partial \varphi_k}{\partial \theta_j}\right)\left(1 + |\alpha_k|^2\right), \tag{2.83}$$

and

$$\langle \alpha_k | \frac{\partial \alpha_k}{\partial \theta_i} \rangle = i |\alpha_k|^2 \left(\frac{\partial \varphi_k}{\partial \theta_i} \right). \tag{2.84}$$

Note that Eq. (2.83) satisfies the condition in Eq. (2.41). This leads to the FIM elements of each single mode as

$$[F_Q^{SM}]_{ij}^k = 4|\alpha_k|^2 \left(\frac{\partial \alpha_k}{\partial \theta_i} \right) \left(\frac{\partial \alpha_k}{\partial \theta_j} \right). \tag{2.85}$$

Using Eq. (2.80) the total FIM is

$$[F_Q^{Coh}]_{ij} = 4 \sum_k |\alpha_k|^2 \left(\frac{\partial \varphi_k}{\partial \theta_i} \right) \left(\frac{\partial \varphi_k}{\partial \theta_j} \right). \tag{2.86}$$

From the inner products in Eq. (2.83)-(2.84) we see that the condition (2.41) is satisfied, then the FIM given by Eq. (2.86) is the most informative bound. For the sake of comparison, promoting the summation to integration, we make use of a normalized version of $\alpha(x)$, i.e., $\alpha(x) = N^{1/2}\bar{\alpha}(x)$, such that the FI per photon takes form

$$\frac{[F_Q^{Coh}]_{ij}}{N} = 4 \int \mathrm{d}x |\bar{\alpha}(x)|^2 \left[\frac{\partial \varphi(x)}{\partial \theta_i} \right] \left[\frac{\partial \varphi(x)}{\partial \theta_j} \right]. \tag{2.87}$$

Note that the expression for the FIM elements in Eq. (2.87) can be derived alternatively following a slightly different approach. The introduction of a spatially dependent phase $\{\varphi_k\}$ for each spatial coordinate (index k) is an unitary operation that can be represented by the operator

$$U = \exp \Big[i \sum_k \varphi_k(\theta)\, a_k^\dagger a_k \Big], \tag{2.88}$$

so that the output quantum state is thus

$$|\Phi(\theta)\rangle = U(\theta)|\alpha\rangle. \tag{2.89}$$

The derivative of the quantum state with respect parameter θ_i is

$$|\Phi_i\rangle = \left(\frac{\partial U}{\partial \theta_i} \right) |\alpha\rangle = i \sum_k \left(\frac{\partial \varphi_k}{\partial \theta_i} \right) a_k^\dagger a_k \, |\alpha\rangle \tag{2.90}$$

hence

$$\langle \Phi | \Phi_i \rangle = i \sum_k \left(\frac{\partial \varphi_k}{\partial \theta_i} \right) \langle \alpha | a_k^\dagger a_k | \alpha \rangle. \tag{2.91}$$

Similarly we can write

$$\begin{aligned}\langle\Phi_i|\Phi_j\rangle &= \sum_k \sum_{k'} \left(\frac{\partial\varphi_k}{\partial\theta_i}\right)\left(\frac{\partial\varphi_{k'}}{\partial\theta_j}\right) \langle\alpha|a_k^\dagger a_k\, a_{k'}^\dagger a_{k'}|\alpha\rangle \\ &= \sum_k \left(\frac{\partial\varphi_k}{\partial\theta_i}\right)\left(\frac{\partial\varphi_k}{\partial\theta_j}\right) \langle\alpha|a_k^\dagger a_k\, a_k^\dagger a_k|\alpha\rangle \\ &+ \sum_{k\neq k'} \left(\frac{\partial\varphi_k}{\partial\theta_i}\right)\left(\frac{\partial\varphi_{k'}}{\partial\theta_j}\right) \langle\alpha|a_k^\dagger a_k|\alpha\rangle\langle a_{k'}^\dagger a_{k'}|\alpha\rangle\end{aligned} \tag{2.92}$$

The elements of the QFIM are

$$\begin{aligned}F_{ij} &= 4\langle\Phi_i|\Phi_j\rangle - 4\langle\Phi|\Phi_i\rangle\langle\Phi|\Phi_j\rangle \\ &= 4\sum_k \left(\frac{\partial\varphi_k}{\partial\theta_i}\right)\left(\frac{\partial\varphi_k}{\partial\theta_j}\right) \\ &\times\Big\{\langle\alpha|a_k^\dagger a_k\, a_k^\dagger a_k|\alpha\rangle - \Big[\langle\alpha|a_k^\dagger a_k|\alpha\rangle\Big]^2\Big\} \\ &= \sum_k \left(\frac{\partial\varphi_k}{\partial\theta_i}\right)\left(\frac{\partial\varphi_k}{\partial\theta_j}\right)\langle(\Delta N_k)^2\rangle\end{aligned} \tag{2.93}$$

where $N_k \equiv \langle a_k^\dagger a_k\rangle$ and the variance is $\langle(\Delta N_k)^2\rangle = \langle N_k^2\rangle - \langle N_k\rangle^2$. Making use of Eq. (2.93) and that $\langle(\Delta N_k)^2 = |\alpha_k|^2$ for quantum coherent states, we obtain Eq. (2.86).

2.4.2 Case II: *N* copies of a multimode single-photon state

Similarly to the previous section, here we present the explicit expression for the FIM elements leading to the CR bound for multi-phase estimation. Consider a single-photon state $|\Psi_0\rangle$ with spatial shape $f(x)$ given by

$$|\Psi_0\rangle = \int \mathrm{d}x\, f(x)\,|x\rangle. \tag{2.94}$$

The state of the photon is considered to gain a phase $\varphi(x,\theta)$ depending on the n-dimensional parameter vector $\theta = \theta_1, \theta_2, ..., \theta_n)$. The phase is assumed to be caused by interaction with a phase object or propagating through a dispersive medium. The outgoing state is

$$|\Psi_{out}\rangle = \int \mathrm{d}x\, f(x)\, e^{i\,\varphi(x,\theta)}|x\rangle. \tag{2.95}$$

Here we assume that both quantum states satisfy the normalization condition $\langle\Psi_i|\Psi_i\rangle = \int \mathrm{d}x|f(x)|^2 = 1$, with $\Psi_i \in \{\Psi_0, \Psi_{out}\}$. The inner products in the FIM elements in Eq. (2.51) are:

$$\langle\partial_i\Psi_{out}|\partial_j\Psi_{out}\rangle = \int \mathrm{d}x|f(x)|^2 \left(\frac{\partial\varphi}{\partial\theta_i}\right)\left(\frac{\partial\varphi}{\partial\theta_j}\right) \tag{2.96}$$

and

$$\langle \Psi_{out} | \partial_k \Psi_{out} \rangle = \int \mathrm{d}x |f(x)|^2 \left(\frac{\partial \varphi}{\partial \theta_k} \right), \tag{2.97}$$

where $k, i, j \in \{1, .., n\}$ and ∂_i denotes the partial derivative with respect to the parameter θ_i. Note that Eq. (2.96) is symmetric under exchange of indexes i and j. Therefore the quanutm state (2.95) satisfies the condition in Eq. (2.41). Explicitly, the FIM elements of a single photon state take the form

$$[F_Q^{SP}]_{ij} = 4 \int \mathrm{d}x |f(x)|^2 \left(\frac{\partial \varphi}{\partial \theta_i} \right) \left(\frac{\partial \varphi}{\partial \theta_j} \right) \tag{2.98}$$

$$-4 \left[\int \mathrm{d}x |f(x)|^2 \left(\frac{\partial \varphi}{\partial \theta_i} \right) \right] \left[\int \mathrm{d}x |f(x)|^2 \left(\frac{\partial \varphi}{\partial \theta_j} \right) \right]. \tag{2.99}$$

For N independent copies of the single-photon state, we have $[F_Q]_{ij} = N[F_Q^{SP}]_{ij}$.

The expressions for the QFIM in Eqs. (2.86) and (2.99) allow to determine whether a coherent multimode quantum state with mean photon number N is equivalent (or nonequivalent) to N copies of a single-photon multimode quantum state for optical phase estimation. Given the same spatial shape of the illumination beam, i.e., $f(x) \equiv \alpha(x)$, the expressions for the QFIM in both cases are equal ($F_{i,j}^{SP} = F_{i,j}^{Coh}$), if $I_i = 0$ holds for all $i = 1 \dots M$, where

$$I_i = \int \mathrm{d}x |f(x)|^2 \Big[\frac{\partial \varphi}{\partial \theta_i} \Big].$$

Note that this is the case if $f(x)$ is a symmetric function, while the phase $\varphi(x, \theta)$ introduced by the object is antisymmetric. This demonstrates that the equivalence, or nonequivalence, of the QFIM calculated using the two types of quantum states condidered above, depends on the symmetry on the spatial (or frequency) variable x of both the illumination beam and the acquired phase. In what follows, for the sake of illumination of this result and as a word of caution for experiments using weak coherent light sources while use single-photon quantum states in the corresponding theoretical analysis; we discuss some specific examples of parameter estimation of phase objects to show the discrepancy between the CR lower bounds for each case.

2.4.3 Examples of discrepancies between the precision bounds for cases I and II

To show the discrepancy in the fundamental bounds for phase estimation when using a single photons model or a multimode coherent state, we consider two cases of relevance in optical metrology. In both cases, an optical beam gains a phase whose characteristic parameters we want to estimate. The precision bounds for the estimation of those parameters, is given by the inverse Fisher FIM as described in Eq. (2.38); and depending on the symmetry of the phase, the FIM elements might vary according to the photonic model of choice.

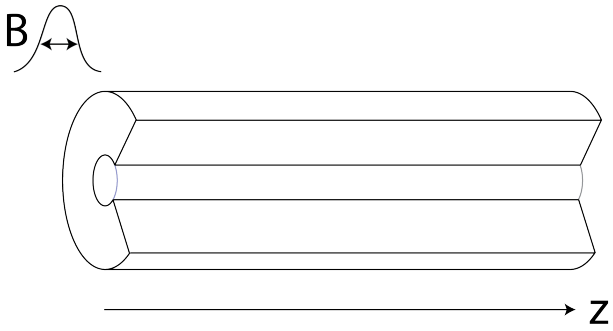

Figure 2.4: Optical fiber as a dispersive medium with dispersion coefficients β_2 and β_3 for a light beam of bandwidh B.

Example 1. Estimation of the parameters of a dispersive medium

Consider a beam propagating through an optical fiber as sketched in figure 2.4. The beam is considered to have a Gaussian spectral profile of the form

$$|f(\Omega)|^2 = \frac{1}{(\pi B^2)^{1/2}} \exp\left(-\frac{\Omega^2}{B^2}\right). \tag{2.100}$$

Here Ω is the central frequency, B is the bandwidth and the normalization condition $\int |f(\Omega)|^2 \, \mathrm{d}\Omega = 1$ holds. For the sake of simplicity and without loss generality we neglect the nonlinear effect in this analysis. After propagation through the fiber, at a distance z beam gains a phase

$$\varphi(\Omega) = \frac{1}{2}\,\beta_2 z\Omega^2 + \frac{1}{6}\,\beta_3 z\Omega^3, \tag{2.101}$$

with $\beta_{2,3}$ the second and third order dispersion coefficients. One can determine the precision bounds for estimation of the dispersion coefficients by computing the FIM elements; to do so, we consider the parameter vector in the following form: $\theta = (\theta_1, \theta_2) = (\beta_2, \beta_3)$.

Multimode coherent state

From Eq. (2.87) one can directly compute the FIM elements by evaluating the inner product integrals (2.83) and (2.84). We make use of integrals of the form:

$$\int_{-\infty}^{\infty} \mathrm{d}x\, x^n \exp\left(-ax^2\right) = \frac{(2k-1)!}{2^k a^k} \left(\frac{\pi}{a}\right)^{1/2} \tag{2.102}$$

with $n = 2k$, k integer. The inner products reduce to:

$$\begin{aligned} \int \mathrm{d}\Omega |\alpha(\Omega)|^2 \left[\frac{\partial\varphi(\Omega)}{\partial\beta_2}\right]^2 &= \frac{1}{(\pi B^2)^{1/2}} \int \mathrm{d}\Omega \left(\frac{1}{2}\Omega^2 z\right)^2 \exp\left(-\frac{\Omega^2}{B^2}\right), \\ &= \frac{3z^2 B^4}{16}, \end{aligned} \tag{2.103}$$

$$\int \mathrm{d}\Omega |\alpha(\Omega)|^2 \left[\frac{\partial\varphi(\Omega)}{\partial\beta_3}\right]^2 = \frac{1}{(\pi B^2)^{1/2}} \int \mathrm{d}\Omega \left(\frac{1}{6}\Omega^3 z\right)^2 \exp\left(-\frac{\Omega^2}{B^2}\right) = \frac{5z^2B^6}{96}, \tag{2.104}$$

$$\int \mathrm{d}\Omega |\alpha(\Omega)|^2 \left[\frac{\partial\varphi(\Omega)}{\partial\beta_2}\right] = \frac{1}{(\pi B^2)^{1/2}} \int \mathrm{d}\Omega \left(\frac{1}{2}\Omega^2 z\right) \exp\left(-\frac{\Omega^2}{B^2}\right) = \frac{zB^2}{4}, \tag{2.105}$$

and

$$\int \mathrm{d}\Omega |\alpha(\Omega)|^2 \left[\frac{\partial\varphi(\Omega)}{\partial\beta_3}\right] = \frac{1}{(\pi B^2)^{1/2}} \int \mathrm{d}\Omega \left(\frac{1}{6}\Omega^3 z\right) \exp\left(-\frac{\Omega^2}{B^2}\right) = 0. \tag{2.106}$$

The FIM elements are:

$$[F_Q^{Coh}]_{11} = 4N\,\frac{3z^2B^4}{16} = \frac{3z^2B^4N}{4}, \tag{2.107}$$

$$\left[F_Q^{Coh}\right]_{22} = 4N\frac{5z^2B^6}{96} = \frac{5z^2B^6N}{24}, \tag{2.108}$$

$$\left[F_Q^{Coh}\right]_{12} = [F_Q^{Coh}]_{21} = 0. \tag{2.109}$$

Single-photon state

Similarly, by comnputing the the inner product integrals in Eqs. (2.96) and (2.97) in an analogous manner, the FIM elements in Eq. (2.99) for N copies of a single-photon states can be written as

$$[F_Q^{SP}]_{11} = 4N\left[\frac{3z^2B^4}{16} - \frac{z^2B^4}{16}\right] = \frac{z^2B^4N}{2}, \tag{2.110}$$

$$\left[F_Q^{SP}\right]_{22} = 4N\frac{5z^2B^6}{96} = \frac{5z^2B^6N}{24}, \tag{2.111}$$

$$\left[F_Q^{SP}\right]_{12} = [F_Q^{SP}]_{21} = 0. \tag{2.112}$$

Estimation errror

To evaluate the discrepancy between the two models more explicitly, we make use of the relative error δ_θ as introduced in Eq. (2.19). Since the conditions for the CR

bound C^S in Eq. (2.38) to be tight are satisfied, the relative error in Eq. (2.20) is

$$\delta_{\theta_i}^2 = \frac{\langle(\Delta\theta_i)^2\rangle}{\theta_i^2} \quad \Longrightarrow \quad \delta_{\theta_i} \geq \frac{1}{\theta_i}\sqrt{[F_Q]_{ii}^{-1}}. \tag{2.113}$$

Explicitly for $\theta = (\theta_1, \theta_2) = (\beta_2, \beta_3)$, the CR lower bound for each parameter is reduced to

$$\langle(\Delta\beta_2)^2\rangle \geq \frac{1}{[F_Q]_{11}(\beta_2)^2} \quad \text{and} \quad \langle(\Delta\beta_3)^2\rangle \geq \frac{1}{[F_Q]_{22}(\beta_3)^2}. \tag{2.114}$$

Hence, the relative errors for a multimode coherent state from Eqs (2.107)-(2.109) are explicitly:

$$\delta_{\beta_2}^2 \geq \frac{1}{\beta_2^2[F_Q^{Coh}]_{11}} = \frac{1}{\beta_2^2}\frac{4}{3z^2B^4N} \tag{2.115}$$

so that the minimum mean number of photons needed to estimate β_2 with relative error δ_{β_2} is given by

$$N^{Coh} \geq \frac{4}{3}\frac{1}{z^2B^4\beta_2^2}\frac{1}{\delta_2^2}. \tag{2.116}$$

On the other hand, the minimum number of single photons N^{SP} required to estimate the parameters with a relative error δ is obtain by substituting Eq. (2.110) in Eq. (2.113), namely

$$\delta_{\beta_2}^2 \geq \frac{1}{\beta_2^2[F_Q^{SP}]_{11}} = \frac{1}{\beta_2^2}\frac{2}{z^2B^4N} \tag{2.117}$$

which leads to

$$N^{SP} \geq 2\,\frac{1}{z^2B^4\beta_2^2}\frac{1}{\delta_2^2}. \tag{2.118}$$

Similarly, for the case of the estimation of β_3, one has

$$\delta_{\beta_3}^2 \geq \frac{1}{\beta_3^2[F_Q^{Coh}]_{22}} = \frac{24}{5z^2B^6\beta_3^2N} \quad \therefore \quad N^{Coh} \geq \frac{24}{5z^2B^6\beta_3^2}\frac{1}{\beta_3^2} \tag{2.119}$$

For the single photon model,

$$\delta_{\beta_3}^2 \geq \frac{1}{\beta_3^2[F_Q^{SP}]_{22}} = \frac{24}{5z^2B^6\beta_3^2N} \quad \therefore \quad N^{SP} \geq \frac{24}{5z^2B^6\beta_3^2}\frac{1}{\beta_3^2} \tag{2.120}$$

In this case, it is straightforward to note that for the estimation of the parameter β_3 the Cramér-Rao bound C^S has the same value either for single-photon or for multimode states. Figures 2.6a shows the discrepancy in the minimum number of photons required to estimate the dispersion coefficient β_2 with relative errors δ_{β_2}, when assuming the quantum state corresponding to N copies of a single photon or a multimode coherent state with mean number of photons N. Similarly, figure 2.6b shows that for the estimation of the parameter β_3 with relative error δ_{β_3}, the number of photons required using a multimode coherent state is equal to the single photon model.

Example 2. Estimation of the height and sidewall angle of a cliff-like nano-structure

Consider an illumination beam with spatial profile $f(x)$ such that

$$|f(x)|^2 = \frac{2}{\sqrt{\pi\sigma^2}} \exp\left\{-\frac{x^2}{\sigma^2}\right\}. \tag{2.121}$$

The beam is reflected by a cliff-like nanostructure made of a highly reflective material and the slope of the cliff-like structure is modeled as a hyperbolic tangent Sigmoid function in the following way

$$S(x) = \frac{h}{2}(1 + \tanh \alpha x), \tag{2.122}$$

such that after interaction with the structure, the optical beam acquires the phase

$$\varphi(x) = kh\,(1 - \tanh \alpha x)\,, \tag{2.123}$$

where h is the height of the cliff structure and $\alpha = 2\tan\beta/h$ is the sidewall angle parameter associated to the sidewall angle β as represented in Fig.2.5. In typical nanostructures, the height is a fraction of the wavelength of the incident light wave, and the sidewall angle is ideally close to 90° [68]. To estimate the precision bounds given by the Crámer-Rao inequality we follow a similar procedure as the one in the previous section.

Single photon state

Let us first consider the illumination beam consisting of N copies of single photons so that the FIM elements are:

$$[F_Q]_{11} = N[F_Q^{SP}]_{11} = 4N\left(\frac{2}{\pi\sigma^2}\right)^{1/2} \frac{\pi^2 - 6}{9}\,\frac{(kh)^2}{\alpha^3}, \tag{2.124}$$

$$[F_Q]_{22} = N[F_Q^{SP}]_{22} = 8k^2N\left[1 - \frac{2}{\pi\sigma^2}\frac{1}{\alpha}\right] - 4k^2N \sim 4k^2N \tag{2.125}$$

since $\alpha\sigma \gg 1$ for $\beta \to 90°$, and

$$[F_Q^{SP}]_{12} = N[F_Q^{SP}]_{12} = 4N\left(\frac{2}{\pi\sigma^2}\right)^{1/2} \frac{k^2h}{\alpha^2}. \tag{2.126}$$

Multimode coherent state

For a multimode coherent state the only difference is that

$$[F_Q^{Coh}]_{22} = 8k^2N\left[1 - \frac{2}{\pi\sigma^2}\frac{1}{\alpha}\right] \sim 8k^2N. \tag{2.127}$$

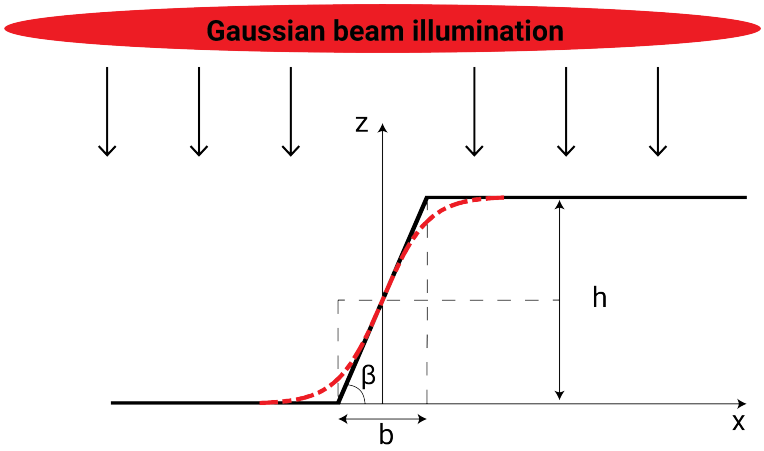

Figure 2.5: Sketch of a Cliff-like nano-structure with sidewall angle β and height h. The red dashed line corresponds to the mathematical model of the slope. The sidewall angle β is related to the parameter α as $\alpha = 2/b = 2\tan\beta/h$.

Estimation error

Since the FIM is no longer diagonal, the elements of the inverse FIM $[F_Q]^{-1}$ must be computed, namely for the single photon case

$$\left[F_Q^{-1}\right]_{11} = \frac{1}{N}\frac{[F_Q]_{22}}{[F_Q]_{11}[F_Q]_{22} - ([F_Q]_{12})^2} \tag{2.128}$$

$$\left[F_Q^{-1}\right]_{22} = \frac{1}{N}\frac{[F_Q]_{11}}{[F_Q]_{11}[F_Q]_{22} - ([F_Q]_{12})^2} \tag{2.129}$$

and

$$\left[F_Q^{-1}\right]_{12} = \left[F_Q^{-1}\right]_{21} = \frac{1}{N}\frac{[F_Q]_{12}}{[F_Q]_{11}[F_Q]_{22} - ([F_Q]_{12})^2} \tag{2.130}$$

Therefore, the minimum number of photons required to estimate α and h with relative errors $\delta_\alpha = \sqrt{\langle(\Delta\alpha)^2\rangle}/\alpha$ and $\delta_h = \sqrt{\langle(\Delta h)^2\rangle}/h$ as in Eqs.(2.19) and (2.20) are

$$N \geq \frac{[F_Q]_{22}}{[F_Q]_{11}[F_Q]_{22} - ([F_Q]_{12})^2}\frac{1}{\alpha^2}\frac{1}{\delta_\alpha^2} \tag{2.131}$$

and

$$N \geq \frac{[F_Q]_{11}}{[F_Q]_{11}[F_Q]_{22} - ([F_Q]_{12})^2}\frac{1}{h^2}\frac{1}{\delta_h^2}. \tag{2.132}$$

Approximation for cases experimentally relevant

Notice that the product of the diagonal elements of the FIM matrix is

$$[F_Q^{SP}]_{11}[F_Q^{SP}]_{22} = 4A\left(\frac{2}{\pi}\right)^{1/2}\frac{\pi^2-6}{9}\,k^4h^2\frac{1}{\sigma\alpha^3} \tag{2.133}$$

with $A = 4$ for a single-photon model and $A = 8$ for a multimode coherent state. Then

$$([F_Q^{SP}]_{12})^2 = \frac{32}{\pi}k^4h^2\frac{1}{\sigma\alpha^3}\,\frac{1}{\sigma\alpha}. \tag{2.134}$$

For angles close to 90°, the product $\sigma\alpha \gg 1$ (the experimentally relevant case):

$$[F_Q^{SP}]_{11}[F_Q^{SP}]_{22} \gg ([F_Q^{SP}]_{12})^2. \tag{2.135}$$

Making use of this result, $\det F_Q \approx [F_Q]_{11}[F_Q]_{22}$. Then, from Eq. (2.131) the minimum number of photons required for estimation of α with relative error δ_α is

$$N \geq \frac{1}{[F_Q]_{11}}\frac{1}{\alpha^2\delta_\alpha^2} = \frac{9\sqrt{\pi}}{4\sqrt{2}\,(\pi^2-6)}\frac{\sigma\alpha}{(kh)^2}\frac{1}{\delta_\alpha^2}. \tag{2.136}$$

Similarly, from Eq. (2.132), the minimum number of photons required for the estimation of the height h with relative error δ_h is

$$N \geq \frac{1}{[F_Q]_{22}}\frac{1}{h^2\delta_h^2} \tag{2.137}$$

From Eqs.(2.125) and (2.127) one can see the discrepancy between the single-photon model and the multimode coherent state; substituting explicitly,

$$N^{Coh} \geq \frac{1}{8(kh)^2}\frac{1}{\delta_h^2}. \tag{2.138}$$

$$N^{SP} \geq= \frac{1}{4(kh)^2}\,\frac{1}{\delta_h^2}. \tag{2.139}$$

Figure 2.6c shows the minimum number of photons required to estimate the side wall angle α with a relative error of δ_α. Since the FI is the same for both coherent multimode states with mean number of photons N and N copies of a single-photon state, the CR bounds yield the same result, whereas for the estimation of the height h, the FI is different for coherent multimode states with mean number of photons N than the one of N copies of a single-photon state.This leads to a difference in the number of photons required to estimate the height of the cliff-like structure, as shown in Fig. 2.6d.

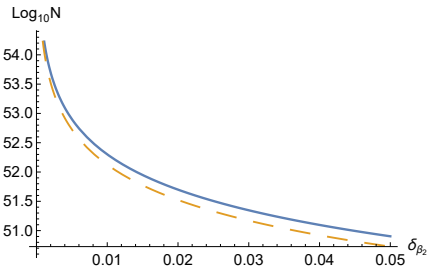

(a) Estimation of β_2

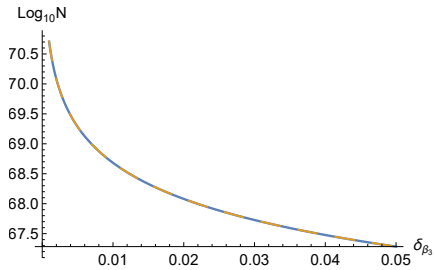

(b) Estimation of β_3

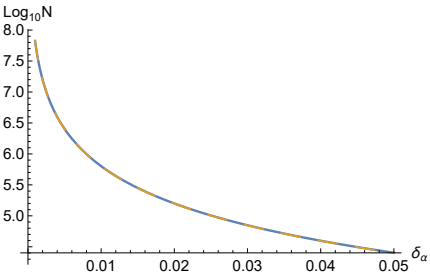

(c) Estimation of α

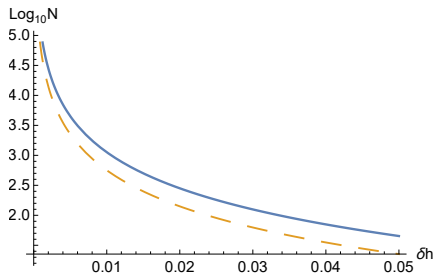

(d) Estimation of h

Figure 2.6: Minimum number of photons required to estimate the parameter θ with precision δ_θ according to the quatum Crámer-Rao bound. The parameters are the a) second-order β_2 and b) third-order β_3 dispersion coefficients of a medium ($B = 10nm$ and $z = 1m$) and the c) sidewall angle parameter and d) height of a cliff-like structure ($h = 150nm$ and $\beta = 88°$). Solid lines correspond to single photon model and dashed lines correspond to multimode coherent state.

2.5 The quantum discord: A measure of deterioration of precision in quantum phase estimation under the presence of loss

As introduced in Section 2.2, it is possible to define the estimation precision bounds when characterizing quantum states. Moreover, when the parameters of interest are encoded in the phase of the state (quantum phase estimation), one can define conditions and protocols for the precision limits to be saturated, hence allowing quantum phase estimation with ultimate precision. In this section, we consider the effects of losses in quantum phase estimation protocols; in particular we study the loss of informational content of a multi-photon quantum state in presence of loses by looking at quantum correlation. The content of this section has been published in a peer reviewed journal as a research article (Ref. [69]) of which the author of this dissertation is second author.

Quantum correlations embedded in entangled states are a resource that facilitate the design of new protocols for parameter estimation. One paradigmatic example of a state of this kind used for quantum-enhanced sensing is a N00N state. This type of states allow to estimate an unknown phase with a resolution that scales as $1/N$, where N is the average number of photons. This is an improvement with respect to the scaling provided by coherent states, like the ones generated by a laser beam, that goes as $\sim 1/\sqrt{N}$.

Quantum correlations that go beyond those described by entanglement can also offer a quantum advantage [70]. Henderson and Vedral [71] as well as Ollivier and Zurek [72] introduced the concept of quantum discord to quantify these type of correlations. They noticed that while there are two equivalent expressions for the mutual information of two random variables that give the same result, their generalizations for measuring the correlations between two quantum systems may yield different results.

The original formulation of quantum discord is difficult to compute [73] even for a simple, although relevant case of two-qubit systems [74–76]. This has led to alternative formulations of the concept that still fulfill a set of conditions expected for a good measure of quantum correlations [77] while being easier to compute in certain scenarios of interest.

One of these alternatives is the geometric measure of quantum discord, or geometric quantum discord (GQD), which is based on the assumption that a bipartite quantum state ρ^{AB} has zero discord [78–81] if and only if there is a Von Neumann measurement $\left\{\Pi_k^A\right\} = |u_k\rangle\langle u_k|$ on the subspace A such that

$$\sum_k \left(\Pi_k^A \otimes I^B\right) \rho \left(\Pi_k^A \otimes I^B\right) = \rho. \tag{2.140}$$

Here I^B designates the identity operator in the subspace B. We restrict ourselves to Von Neumann measurements [82, 83], so all projectors Π_k^A are one-dimensional. In this case we can write the projectors Π_k^A in terms of a set of vectors $\{|u_k\rangle\}$ that is a basis in subspace A.

This implies that zero-discord quantum states are of the form

$$\rho = \sum_k p_k \left|u_k\right\rangle \left\langle u_k\right| \otimes \rho_k^B, \tag{2.141}$$

where ρ_k^B are density matrices in subspace B and p_k are positive real numbers with $\sum_k p_k = 1$. These states are often referred to as *classical-quantum* states [84]. From the definition of classical-quantum states, it naturally follows that the geometric quantum discord is the minimum distance (square norm in the Hilbert-Schmidt space) between the quantum state ρ and the closest classical-quantum state $\sum_k \left(\Pi_k^A \otimes I^B\right) \rho \left(\Pi_k^A \otimes I^B\right)$.

This definition for GQD might show some drawbacks [85] since it can increase under local operations of the party B that is not measured. This undesirable effect can be corrected [86] if one substitutes the density matrix ρ by $\rho^{1/2}$, so that the GQD is now the minimum distance (square norm in the Hilbert-Schmidt space) between $\rho^{1/2}$ and $\sum_k \left(\Pi_k^A \otimes I^B\right) \rho^{1/2} \left(\Pi_k^A \otimes I^B\right)$. In what follows, this is the definition of geometric quantum discord used in this text. One major advantage of this expression is that it can be calculated in closed form for quantum bipartite systems of dimension $2 \times D$ [86, 87].

Simultaneously as the previous correction of the geometric discord was reported, Girolami, Tufarelli and Adesso [88] introduced the local quantum uncertainty (LQU), a new formulation of quantum discord defined as follows: given a specific Von Neumann measurement where each projector Π_k^A is assigned an eigenvalue λ_k (all λ_k are different), the LQU is the minimum over all possible ensembles $\left\{\Pi_k^A\right\}$ of the Wigner-Yanase Skew information, I [89]:

$$I = -\frac{1}{2}\mathrm{Tr}\left\{\left[\rho^{1/2}, M\right]^2\right\}. \tag{2.142}$$

Here $M = \left(\sum_k \lambda_k \Pi_k^A\right) \otimes I^B$ and I^B is the identity on subspace B. Again, as in the case of the geometric quantum discord discussed above, one important advantage of LQU is that it can be calculated in closed form for $2 \times D$ quantum bipartite systems.

For a given Von Neumann measurement $\left\{\Pi_k^A \otimes I^B\right\}$, one can define its quantum uncertainty as $Q = \sum_k I_k$, where

$$I_k = -\frac{1}{2}\mathrm{Tr}\left\{\left[\rho^{1/2}, \Pi_k^A \otimes I^B\right]^2\right\}. \tag{2.143}$$

It turns out that the GQD is the minimum of the quantum uncertainty Q over all possible Von Neumann measurements. This introduces a revealing link between the LQU and the GQD formulations of the quantum discord through the use of similar expressions of the Wigner-Yanase Skew information [83]. In a given Von Neumann measurement, characterized by a set of one-dimensional operators $\left\{\Pi_k^A\right\}$, each one associated with a possible experimental outcome, the intrinsic statistical error associated with the measurement has a quantum contribution. The Skew information, a measure of the non-commutativity between the quantum state ρ and

the set $\{\Pi_k^A \otimes I^B\}$, can be used to quantify this quantum uncertainty. In this context, the local quantum uncertainty and the geometric discord can be understood as the minimum quantum uncertainty that one can have among all possible Von Neumann measurements. However, they differ in how they evaluate the quantum uncertainty. The geometric discord considers the sum of the quantum uncertainties associated with each outcome $\Pi_k^A \otimes I^B$, while the local quantum uncertainty considers the quantum uncertainty associated to an operator that describes the global measurement, $M = \left(\sum_k \lambda_k \Pi_k^A\right) \otimes I^B$, with λ_k the eigenvalues associated to the possible outcomes of the measurement.

Both metrics for quantum discord considered above, namely the local quantum uncertainty and the geometric quantum discord, fulfil similar requirements that the original discord definition does, which make them good discord metrics [77, 88]. These discord quantifiers are non-negative and invariant under local unitary transformations, furthermore they yield zero only for quantum-classical states and the discord reduces to an entanglement monotone, which in the case of pure states it is characterized by the marginal entropy of subsystem A.

As the geometric discord and the local quantum uncertainty can be both explained as the minimum quantum uncertainty that can be attained in a Von Neumann measurement, in what follows we show that they are indeed the same discord metric for the case of bipartite quantum systems whose dimension is $2 \times D$, although this may not be true for systems with other dimensions. Moreover, we take advantage of the fact that both measures can be evaluated in closed form, in sharp contrast to other alternative formulations of quantum discord [70].

The relevance of this study for the scope of this thesis is to explore the Crámer-Rao lower bound for multi-phase estimation precision when using quantum states of light; in particular, states with non-classical correlations that can be explicitly computed.

We show an example the case of N00N states for phase estimation in a lossy environment. Since quantum systems experiencing losses are fragile, this often leads to a worsening of the achievable estimation precision, thus reducing the quantum advantage observed for the lossless case. In general it is possible to consider several measures to characterize the effect of losses, but it is not clear in principle which one is the most convenient or informative for each scenario.

As introduced in Section 2.2, for one-parameter estimation, the Cramér-Rao bound given by the quantum FI in Eq. (2.38) is attainable [22], so it is a good measure of the enhancement provided by a phase-estimation protocol making use of a specific quantum state [39,43]. Remarkably, we demonstrate that the decrease of quantum Fisher information under the presence of losses, with respect to the ideal case with no losses, is precisely the geometric quantum discord. In this sense, the quantum discord is more informative than negativity concerning the spatial resolution achievable under the present of loss, as given by the quantum Fisher information.

2.5.1 Equivalence regimes for Local Quantum Uncertainty and Geometric Quantum Discord

The quantum uncertainty Q defined in [83], whose minimum yields the GQD, can be written as $Q = \sum_j I_j$ where

$$\begin{aligned} I_j &= -\frac{1}{2}\,\mathrm{Tr}\left\{\left[\rho^{1/2}, \Pi_j^A \otimes I^B\right]^2\right\} = \mathrm{Tr}\left[\rho\left(\Pi_j^A\right)^2\right] - \mathrm{Tr}\left(\rho^{1/2}\Pi_j^A\,\rho^{1/2}\Pi_j^A\right) \\ &= \mathrm{Tr}_B\, V_j, \end{aligned} \tag{2.144}$$

and V_j is defined as

$$V_j = \langle u_j|\rho|u_j\rangle - \langle u_j|\rho^{1/2}|u_j\rangle\langle u_j|\rho^{1/2}|u_j\rangle. \tag{2.145}$$

If we make use of the resolution of the identity on subspace A, i.e., $\sum_i |u_i\rangle\langle u_i| = I^A$, we obtain that

$$Q = \sum_j \mathrm{Tr}_B\, V_j = 2\sum_{j<k} \mathrm{Tr}_B\, V_{jk}, \tag{2.146}$$

where

$$V_{jk} = \langle u_j|\rho^{1/2}|u_k\rangle\langle u_k|\rho^{1/2}|u_j\rangle, \tag{2.147}$$

and $V_{jk} = V_{kj}$.

In a similar vein, the quantum uncertainty U defined in [88], whose minimum yields the LQU, can be written as

$$\begin{aligned} U &= \mathrm{Tr}_B\left\{\sum_j \lambda_j^2\langle u_j|\rho|u_j\rangle\ - \sum_{j,k}\lambda_j\lambda_k\langle u_j|\rho^{1/2}|u_k\rangle\langle u_k|\rho^{1/2}|u_j\rangle\right\} \\ &= \sum_j \lambda_j^2 \mathrm{Tr}_B\, V_j - 2\sum_{jk}\mathrm{Tr}_B\,\lambda_j\lambda_k V_{jk} \\ &= \sum_{j<k}(\lambda_j^2+\lambda_k^2)\,\mathrm{Tr}_B V_{jk} - 2\sum_{j<k}\lambda_j\lambda_k\mathrm{Tr}_B\, V_{jk} \\ &= \sum_{j<k}(\lambda_j-\lambda_k)^2\mathrm{Tr}_B\, V_{jk}, \end{aligned} \tag{2.148}$$

where λ_j corresponds to the eigenvalue of the j-th projector constituting a von Neumann measurement.

Equations (2.146) and (2.148) are valid for arbitrary dimensions of the Hilbert spaces of the bipartite quantum states, and for any quantum state described by density matrix ρ. For a Hilbert space with dimension $2 \times D$ the key observation is that

$$\begin{aligned} &\langle u_1|\rho|u_1\rangle - \langle u_1|\rho^{1/2}|u_1\rangle\langle u_1|\rho^{1/2}|u_1\rangle \\ &= \langle u_1|\rho^{1/2}|u_2\rangle\langle u_2|\rho^{1/2}|u_1\rangle \\ &= \langle u_2|\rho|u_2\rangle - \langle u_2|\rho^{1/2}|u_2\rangle\langle u_2|\rho^{1/2}|u_2\rangle. \end{aligned} \tag{2.149}$$

so that $V_1 = V_2 = V_{12}$. In this case,

$$U = (\lambda_1 - \lambda_2)^2 \mathrm{Tr}_B\, V_{12} = \frac{(\lambda_1 - \lambda_2)^2}{2} Q. \tag{2.150}$$

Equation (2.150) shows that the quantum uncertainties Q and U are proportional to each other, thus implying that the measures of quantum discord that derive from them are indeed equivalent for bipartite systems of dimension $2 \times D$.

2.5.2 Non-equivalence between LQU and GQD in systems with arbitrary dimensions

In this section we want to demonstrate that in bipartite systems where the dimension of both subsystems is greater than 2, the LQU and GQD are not proportional to each other. For the sake of simplicity, we restrict ourselves to comparing the values of Q and U for pure states in Hilbert spaces of dimensions $2 \times D$ and $3 \times D$.

We start by noticing that any pure bipartite quantum state can be written as a Schmidt decomposition

$$|\Psi\rangle = \sum_m \sqrt{s_m} |\alpha_m\rangle |\beta_m\rangle, \tag{2.151}$$

where $\{\alpha_m\}$ is a basis in subspace A, $\{\beta_m\}$ is a basis in subspace B and $\{s_j\}$ are the Schmidt coefficients, with the normalization condition $\sum_j s_j = 1$. We can easily derive that

$$\mathrm{Tr}_B\, V_{jk} = \Big[\sum_m s_m \big| \langle \alpha_m | u_j \rangle \big|^2 \Big] \times \Big[\sum_n s_n \big| \langle \alpha_n | u_k \rangle \big|^2 \Big]. \tag{2.152}$$

In Ref. [86] it was demonstrated that for pure states the von Neumann measurement that minimizes the quantum uncertainty Q corresponds to choosing $|u_i\rangle \equiv |\alpha_i\rangle$. In this case $\mathrm{Tr}_B\, V_{jk} = s_j s_k$ so the geometric quantum discord for pure states is $D_G = 2 \sum_{j<k} s_j s_k$. By making use of the normalization of the quantum state we obtain that $2 \sum_{i<j} s_i s_j = 1 - \sum_i s_i^2$ so the quantum discord for pure states can also be written as $D_G = 1 - \sum_i s_i^2$, as reported in [86].

The expression of the quantum uncertainty U for pure states is

$$U = \sum_{j<k} (\lambda_j - \lambda_k)^2 \Big[\sum_m s_m \big| \langle \alpha_m | u_j \rangle \big|^2 \Big] \times \Big[\sum_n s_n \big| \langle \alpha_n | u_k \rangle \big|^2 \Big]. \tag{2.153}$$

We have performed extensive numerical simulations choosing many random von Neumann bases $\{|u_i\rangle\}$ to calculate the range of possible values of the quantum uncertainties Q and U. The von Neumann bases are obtained by choosing random unitary transformations U of the bases $\{|\alpha_i\rangle\}$ so that $\{|u_i\rangle\} = U\,\{|\alpha_i\rangle\}$. For $2 \times D$ and $3 \times D$ quantum systems, one can choose the most general unitary transformation as given in [90].

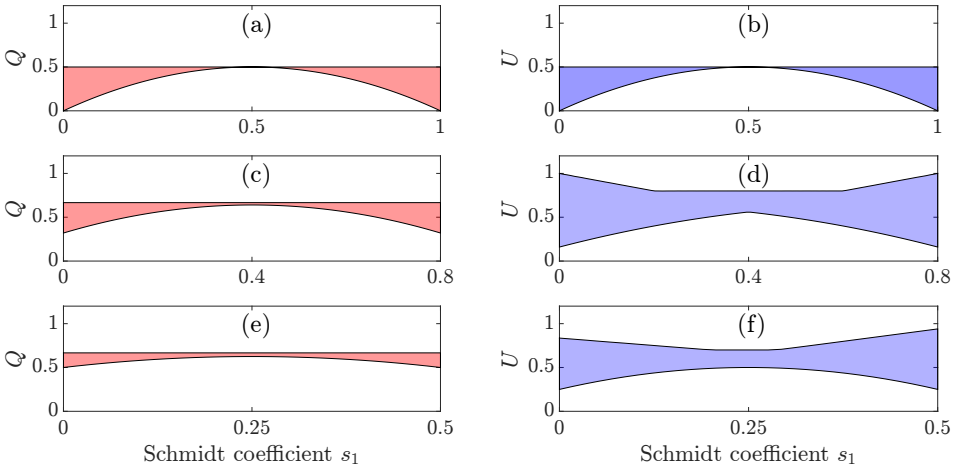

Figure 2.7: All possible values of the Quantum uncertainties Q (left) and U (right) as a function of the Schmidt coefficients s_1 for fixed values of s_2, as indicated in the plot. (a) and (b) show results for $2 \times D$ systems, while (c)-(f) show results for $3 \times D$ systems with $\lambda_1 = 4, \lambda_2 = 3$ and $\lambda_3 = 2$. (c) and (d): Schmidt coefficient $s_2 = 0.2$; (e) and (f): Schmidt coefficient $s_2 = 0.5$. The Schmidt coefficients are dimensionless.

Figure 1(a) shows all possible values of the quantum uncertainty Q obtained numerically for a $2 \times D$ quantum system. The solid lines correspond to the minimum value of Q, that is $D_G = 2s_1(1-s_1)$, and the maximum value, $D_G = 1 - 1/2 = 0.5$ [86]. Fig. 1(b) shows all possible values of U for a $2 \times D$ quantum system with $(\lambda_1 - \lambda_2)^2/2 = 1$. As expected from the results obtained in Section 2.5.1, Figs. 1(a) and (b) show the same results.

Figs. 1(c) to 1(f) correspond to a $3 \times D$ system. The numerical simulations hereby presented show that the minimum of U is attained for von Neumann measurements where the three orthogonal measurement projectors Π_i^A $(i = 1, 2, 3)$ can be written as $\Pi_i^A = |\alpha_{p(i)}\rangle\langle\alpha_{p(i)}|$, where $p(i)$ designates the permutation $\{1, 2, 3\} \longrightarrow \{p(1), p(2), p(3)\}$ that yields the minimum value of U. We have six possibilities corresponding to the six different ways we can associate one vector of the set $|u_i\rangle$ with one vector of the set $|\alpha_i\rangle$. The local quantum uncertainty is

$$LQU = \sum_{j<k} (\lambda_j - \lambda_k)^2 s_{p(j)} s_{p(k)}. \tag{2.154}$$

The eigenvalue λ_i that we associate to each von Neumann state $|\alpha_i\rangle$ now matters. This is in contrast to the case of Q, where there is no eigenvalues associated to each outcome of a measurement and so all outcomes have the same weight.

Note that the maximum value of Q for pure states is independent of the Schmidt coefficients s_i, and it is $1/2$ for $2 \times D$ systems and $2/3$ for $3 \times D$. On the other hand, Figs. 1(d) and (f) show that the maximum value of U for $3 \times D$ systems may change for different values of the Schmidt coefficients- As a conclusion, such

value does not depend only on the dimensions of the subsystems, which is the case of the quantum uncertainty Q.

Figure 2 shows how, for two specific set of values of the eigenvalues λ_i, the correspondence between vectors $|u_i\rangle$ and $|\alpha_i\rangle$ that give the minimum of quantum uncertainty U varies for different values of s_1 and s_2. Each color in the figures stands for a different value of the minimum of U. Fig. 2(a) shows that for the case with eigenvalues $\lambda_1 = 2$, $\lambda_2 = 4$ and $\lambda_3 = 1$, when comparing the minimum of U obtained for each value of s_1 and s_2, up to six different results are obtained. These six minimum values of U can be obtained making use of the six possible permutations in Eq. (13). In Fig. 2(b) we consider the case with eigenvalues $\lambda_1 = 4$, $\lambda_2 = 3$ and $\lambda_3 = 2$. Now one can obtain up to three different minima of U when considering all possible Schmidt coefficients.

2.5.3 Geometric quantum discord of NOON states under the presence of loss

To demonstrate the usefulness of the equivalence between GQD and LQU, we consider the relevant case of N00N states for phase estimation,

$$|\Psi\rangle_{AB} = \frac{1}{\sqrt{2}}\Big(|N\rangle_A |0\rangle_B + \exp(iN\varphi) |0\rangle_A |N\rangle_B \Big), \tag{2.155}$$

where φ is the phase per photon introduced in one of the modes (subsystems A or B), and N is the non-zero number of photons in either of the modes. N00N states can be used to estimate an unknown phase φ with a precision that scales as $1/N$ [91]. Compared with protocols that make use of coherent states, that provide a precision that scales as $1/\sqrt{N}$, N00N states are an important example of quantum-enhanced phase estimation.

We consider the case where there are losses only in subsystem B (non-symmetric losses). The reason for this is that in this scenario the quantum state is a $2\times(N+1)$ system, which allows us to calculate the quantum discord in a straightforward way. As shown in Figure 2.9, we can model such losses by considering that photons travelling in subsystem B traverse a fictitious beam splitter (BS) with reflection coefficient r (photons moving from subsystem B to subsystem C) and a transmission coefficient t (photons that continue in subsystem B) [92]. The overall quantum state after the BS is

$$\begin{aligned} |\Psi\rangle_{ABC} \;=\; & \frac{1}{\sqrt{2}}\big[|N\rangle_A |0\rangle_B |0\rangle_C \\ & + \sum_{n=0}^{N} \sqrt{\binom{N}{n}}\, t^n r^{N-n} \exp(in\varphi) |0\rangle_A |n\rangle_B |N-n\rangle_C \big], \end{aligned} \tag{2.156}$$

with two accessible states for subsystem A ($\{0, N\}$) and $N+1$ for subsystem B ($\{0, ..., N\}$).

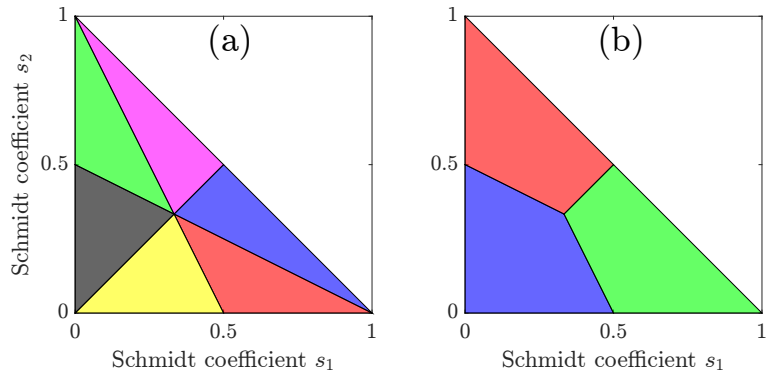

Figure 2.8: Comparison of the values of the minimum of the quantum uncertainty U obtained for different Schmidt coefficients s_1 and s_2. (a) The eigenvalues associated to the Von Neumann measurement are $\lambda_1 = 2$, $\lambda_2 = 4$ and $\lambda_3 = 1$; (b) The eigenvalues associated to the Von Neumann measurement are $\lambda_1 = 4$, $\lambda_2 = 3$ and $\lambda_3 = 2$. Each color designates a given value of the minimum of U. In (a) the value of the minimum of U, for all possible coefficients s_1 and s_2, can yield up to six different results. In (b) one finds only three different values of the minimum of U. The Schmidt coefficients are dimensionless.

The density matrix that describes subsystem AB is obtained calculating the partial trace of the state given by Eq. (2.156) with respect to subsystem C. In this way,

$$\begin{aligned}\rho^{AB} &= \frac{1}{2}\Big(|N\rangle_A|0\rangle_B + t^N \exp(iN\varphi)\,|0\rangle_A|N\rangle_B\Big)\\ &\times\Big(\langle N|_A\langle 0|_B + t^{*N}\exp(-iN\varphi)\,\langle 0|_A\langle N|_B\Big)\\ &+\frac{1}{2}\sum_{n=0}^{N-1}\binom{N}{n}|t|^{2n}|r|^{2(N-n)}\,|0\rangle_A|n\rangle_B\langle 0|_A\langle n|_B\,. \end{aligned} \tag{2.157}$$

The fact that the dimension of the quantum state of subsystems AB is $2 \times D$ with $D = N + 1$ allows us to readily calculate the Local Quantum Uncertainty, or equivalently the Geometric Quantum Discord.

Calculation of the quantum Fisher information

The quantum Fisher Information F_Q associated to the quantum state given by Eq. (2.157) can be calculated by making use of the spectral decomposition of the state: $\rho^{AB} = \sum_i \lambda_i(\varphi)\,|\lambda_i(\varphi)\rangle_{AB}\langle\lambda_i(\varphi)|_{AB}$. Here $\lambda_i(\varphi)$ are the eigenvalues of the decomposition and $|\lambda_i(\varphi)\rangle_{AB}$ are the corresponding eigenvectors. It can be easily demonstrated that all eigenvalues show no dependence on the value of φ and that there are two eigenvectors with a non-zero φ -dependence:

$$|\lambda_1\rangle = \mathcal{N}\left[|N\rangle_A|0\rangle_B + t^N \mathrm{e}^{iN\varphi}|0\rangle_A|N\rangle_B\right], \tag{2.158}$$

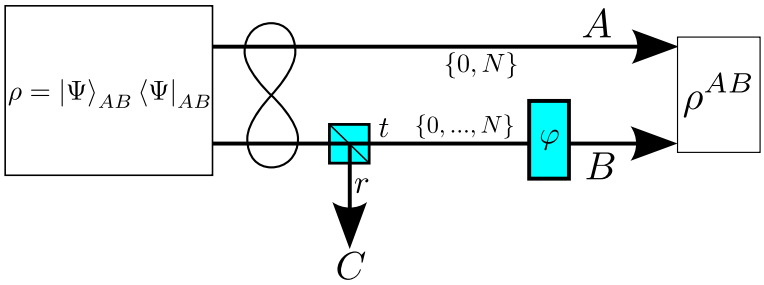

Figure 2.9: We consider the case of a simple $2 \times D$ quantum system with $D = N + 1$: A bipartite N00N state ρ^{AB} with non-symmetric losses. Photon losses are considered in subsystem B, where a fictitious beam splitter with reflectivity r and transmissivity t models the system losses. Subsystem A has only two accessible states $\{0, N\}$ whereas subsystem B has $D = N + 1$ accessible states $\{0, ..., N\}$ given by the combination term in Eq. (2.156).

with $\lambda_1 = \left(1 + |t|^{2N}\right)/2$, and

$$|\lambda_2\rangle = \mathcal{N}\left[-t^{*N}|N\rangle_A|0\rangle_B + \mathrm{e}^{iN\varphi}|0\rangle_A|N\rangle_B\right] \tag{2.159}$$

with $\lambda_2 = 0$. The normalization constant is $\mathcal{N} = (1+|t|^{2N})^{-1/2}$. In this case [92,93] the quantum Fisher information reads $F_Q = \lambda_1 F_1$ with

$$F_1 = 4\left[\left\langle \frac{\partial\lambda_1}{\partial\varphi}\middle|\frac{\partial\lambda_1}{\partial\varphi}\right\rangle - \left|\left\langle\lambda_1\middle|\frac{\partial\lambda_1}{\partial\varphi}\right\rangle\right|^2\right], \tag{2.160}$$

which yields the simple expression

$$F_Q = N^2\frac{2|t|^{2N}}{1+|t|^{2N}}. \tag{2.161}$$

Note that for the ideal lossless case, we obtain the well-known result $F_Q = N^2$.

Calculation of LQU and GQD

Given that LQU and geometric quantum discord are equivalent discord measures for $2\times(N+1)$ quantum systems, in what follows we will refer to them as geometric quantum discord D_G for the sake of simplicity. According to Ref. [88], the LQU of $2 \times (N + 1)$ bipartite quantum systems is $D_G = 1 - \lambda_{\max}$ where $\lambda_{\max}$ is the greatest eigenvalue of the 3×3 symmetric matrix W_{AB},

$$(W_{AB})_{ij} = \mathrm{Tr}\Big(\rho^{1/2}(\sigma_i \otimes \mathbb{1})\rho^{1/2}(\sigma_j \otimes \mathbb{1})\Big). \tag{2.162}$$

Here σ_i designates the three Pauli matrices. We obtain that the greater eigenvalue of the matrix W, considering the quantum state ρ_{AB} described by Eq. (2.157), is

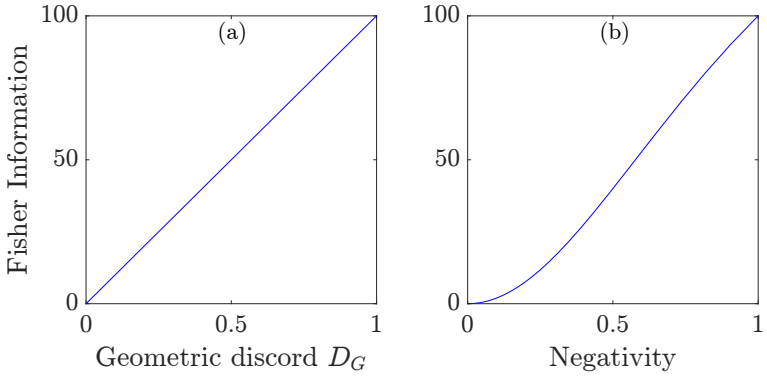

Figure 2.10: Quantum Fisher Information for the N00N state with losses in one subsystem as a function of Geometric Quantum Discord D_G (left) and Negativity (right).

$\lambda_{\max} = (1 - |t|^{2N})/(1 + |t|^{2N})$. Therefore the corresponding geometric quantum discord is

$$D_G = \frac{2|t|^{2N}}{1 + |t|^{2N}}. \tag{2.163}$$

We can thus write a very simple relationship between the quantum Fisher information with and without loss

$$F_Q^{\text{loss}} = D_G \times F_Q^{\text{lossless}}. \tag{2.164}$$

where F_Q^{loss} designates the quantum Fisher information of the N00N state in a lossy environment and F_Q^{lossless} is the quantum Fisher information of the ideal (no losses) N00N state. Remarkably, we have found that the geometric quantum discord (and so the Local quantum uncertainty) quantifies the loss of quantum Fisher information due to losses. Fig. 2.10(a) shows the linear relationship between Fisher information and D_G for a N00N state with $N = 10$. It turns out that the geometric quantum discord is the decrease of quantum Fisher information of a N00N state due to non-symmetric losses.

The quantum state given by Eq. (2.157) is always entangled. This can be demonstrated calculating the negativity, that is an entanglement monotone [94]. Fig. 2.10(b) shows the Quantum Fisher Information as a function of negativity. For high degree of entanglement (low losses and thus negativity close to 1) the Fisher information is a quasi-linear function the negativity of the quantum state. However, for low values of entanglement (high losses and low values of negativity) the relationship between quantum Fisher information and negativity is no longer lineal, contrary to the case of the geometric quantum discord.

We have demonstrated that the geometric quantum discord introduced in [86] and the local quantum uncertainty [88] are equivalent measures of discord for $2 \times D$ quantum bipartite systems. As an example of the relevance of the geometric quantum discord (and local quantum uncertainty) for quantum estimation of

quantum phases we have considered N00N states in non-symmetric lossy environments. Since these states are $2 \times (N+1)$ bipartite quantum systems, LQU and GQD are equivalent measures of quantum discord. Furthermore, we have shown that the geometric quantum discord faithfully quantifies the decrease of quantum Fisher information due to losses, a good indicator of the quantum enhancement provided by N00N states for phase estimation.

Chapter 3

Optical sensing with spatial modes of light

Modal measurements methods have shown to be an efficient strategy to surpass the standard diffraction limit [26,63,95]. The idea comes from the fact that direct imaging techniques, consisting on intensity measurements of the complete field reflected o transmitted by an object, lead to resolution limitations. Hence, the use of spatial modes aims at sensing selectively light that contains relevant information about the object's features and neglect other field contributions. In the case of direct imaging techniques, those contributions still present in the detected field might lead to diffraction effects affecting the estimation of the object's parameters.

Using spatial mode selective sensing, we aim at defining measurement strategies consisting on mapping the effects of light-matter interaction over spatial modes of light. In general, such a technique is reduced to measuring the coefficients of the modal decomposition of the optical beam after interaction with the sample. Since those coefficients are imprinted with the physical characteristics of the target, this allows to directly estimate the spatial features of interest from the mode weights. Although this technique seems to be straightforward, for it to be accurate, it is often needed to measure the coefficients of a very large number of modes depending on the selected set of modes, which can be technically cumbersome.

In this chapter we introduce the concept of spatial modes of light and present some standard examples of modal basis frequently used due to their symmetries. We introduce techniques used to experimentally generate spatial modes of light, focusing specifically on the use of phase-only Spatial Light Modulators (SLM). In Section 3.2 we present the use of spatial modes for optical metrology and sensing, introducing the concept of *Spatial Spectroscopy*. Similar approaches are also refered to in the literature as *wavefront sensing* of *hyperspectral imaging*. We propose schemes for determining the modal decomposition of an optical beam; due to the limitations and implementation challenges of these techniques we propose a method to extract information about the modal decomposition without the need

of complete modal projections but by sensing the field imprinted with a specific phase information. In Section 3.3 we present as an example the two-dimensional localization of an optical beam in a transverse plane using optical vortex field phase projection in the sensing scheme.

3.1 What are spatial modes of light?

To define spatial modes of light, we start from the basis of the theory of electromagnetism, in which Maxwell's equations describe the dynamics of electromagnetic fields. In absence of sources, the dynamics of the field in a homogeneous medium is described by the wave equation

$$\nabla^2 U(r,t) + \frac{1}{c^2}\frac{\partial^2}{\partial t^2} U(r,t) = 0, \tag{3.1}$$

where c is the speed of light satisfying $c^2\mu\epsilon = 1$, with μ and ϵ the magnetic permeability and electric permitivity of the propagation medium. $U(r,t)$ is either the electric or magnetic field assumed to be time harmonic. Throughout this work, we assume linearly-polarized monochromatic fields of the form $U(r,t) = U(r)\exp(i\omega t)$. Under this assumption, the wave equation Eq. (3.1) is reduced to the scalar Helmholtz equation

$$\nabla^2 U(r) + k^2 U(r) = 0, \tag{3.2}$$

where $k = \omega/c = 2\pi/\lambda$ is the wave number, ω the frequency and λ the wavelength of the time-harmonic field whose temporal dependence $\exp(i\omega t)$ has been neglected to simplify the notation.

Assuming homogeneous and isotropic media, the wave vector is predominantly parallel to the electromagnetic energy flux [96]. Without losing generality let us assume the wave vector along the z axis, which defines the electromagnetic wave propagation direction. The vector k satisfies $k_x^2 + k_y^2 + k_z^2 = \omega^2 n^2/c^2$, with n the refractive index of the medium.

In this conditions, one can separate Helmholtz equation in its transverse and longitudinal parts

$$\nabla_T^2 U(r) + \frac{\partial^2}{\partial z^2} U(r) + k^2 U(r) = 0. \tag{3.3}$$

Assuming separation of variables [97], the solution of the z dependence component is of the form $\exp(-ikz)$, such that the field is

$$U(r) = U(r_T)\exp(-ikz), \tag{3.4}$$

where r_T is the coordinate in the transverse plane. Under the *paraxial approximation*, one assumes that the field varies slowly along the propagation direction z, as compared to the variations in the transverse plane, such that

$$\frac{\partial^2}{\partial z^2} U(r) \ll k\frac{\partial}{\partial z} U(r) \qquad \text{and} \qquad \frac{\partial^2}{\partial z^2} U(r) \ll \nabla_T^2 U(r). \tag{3.5}$$

This leads to the paraxial Helmholtz equation

$$\nabla_T^2 U(r) - 2ik\frac{\partial}{\partial z}U(r) = 0. \tag{3.6}$$

A general solution of the paraxial Helmholtz equation in terms of the radial coordinate $\rho = \sqrt{x^2 + y^2}$ has the form

$$U_G(\rho, z) = A\frac{w_0}{w(z)}\ \exp\left\{-\frac{\rho^2}{w^2(z)}\right\}\ \exp\left\{-ikz - ik\frac{\rho^2}{2R(z)} + i\zeta(z)\right\}, \tag{3.7}$$

which corresponds to a field with paraboidal wavefront profile of amplitude A and radius of curvature $R(z)$. The spotsize $w(z)$ is the distance to the optical axis from a point in the transverse plane such that the amplitude of the field falls to $1/e$ of its peak value. The beam waist w_0 is the narrowest spotsize considered to be reached at $z = 0$. The wavefront is nearly flat along a distance z_R known as Rayleyg's range and $\zeta(z)$ is a phase acquired through propagation known as *Gouy phase*. The beam parameters are explicitly given by:

$$\begin{aligned}
w(z) &= w_o\sqrt{1 + (\frac{z}{z_R})^2} && \text{Beam radius}\\
w_0 = w(0) &= \sqrt{\frac{\lambda z_R}{\pi}} && \text{Beam waist}\\
z_R &= \frac{\pi w_0^2 n}{\lambda} && \text{Rayleigh range}\\
R(z) &= z\left[1 + (\frac{z_R}{z})^2\right] && \text{Radius of curvature}\\
\xi(z) &= \arctan\left(\frac{z}{z_R}\right) && \text{Gouy phase}
\end{aligned} \tag{3.8}$$

Furthermore, a solution to the paraxial Helmholtz equation (3.6) can be written as a combination of elements of an orthonormal basis of functions $\{U_m(r)\}$, further referred as modes, such that

$$U(r) = \sum_m \alpha_m U_m(r). \tag{3.9}$$

The modes satisfy the orthonormality condition

$$\int U_m(r)U_n^*(r) = \delta_{m,n'}. \tag{3.10}$$

The complex coefficients of the modal decomposition of the field (3.9) α_m are given by

$$\alpha_m = \int U(r)\, U_m^*(r)\mathrm{d}r. \tag{3.11}$$

Note that the Gaussian solution in Eq. (3.7) contains a phase factor that depends only on the propagation distance z, such that at any plane z_0 the phase is independent of the transverse coordinate. Moreover, the decomposition in Eq. (3.9) and the normalization condition (3.10) allow decompositions into modes with transverse-coordinates-dependent phases, such that combined with complex coefficients are solutions to the paraxial Helmholtz equation.

The paraxial regime defines a general set of modes referred to as *Transverse Electromagnetic modes* (TEM) in which no electric nor magnetic field is present in the direction of propagation ($\hat{k} = \vec{k}/|k|$). Collimated[1] beams generated by lasers with cylindrical symmetry have spatial profile resulting of a combination of a Gaussian contribution as in Eq. (3.7) and a circularly-symmetric Laguerre polynomial. Some other laser systems have instead Cartesian symmetry due to partially reflective windows, this results in spatial profiles with the same Gaussian contribution and a Cartesian-symmetric Hermite polynomials. These two sets of transverse modes can be made to form an orthonormal set of modes further described in what follows.

3.1.1 Hermite-Gauss modes

A solution in Cartesian (x,y) coordinates to the scalar Helmholtz equation under the paraxial approximation Eq. (3.6) are the Hermite-Gaussian ($\mathrm{HG}_{n,m}$) modes, given by

$$\begin{aligned} HG_{n,m}(\rho,z) &= \frac{C_{mn}}{w(z)} H_n\left(\frac{\sqrt{2}x}{w(z)}\right) H_m\left(\frac{\sqrt{2}y}{w(z)}\right) \exp\left[i(n+m+1)\zeta(z)\right] \\ &\quad \times \exp\left(-\frac{\rho^2}{w^2(z)}\right) \exp\left(\frac{-ik\rho^2}{2R(z)}\right) \exp(-ikz) \end{aligned} \tag{3.12}$$

where C_{mn} is the normalization constant satisfying orthonormality condition in Eq. (3.10)

$$C_{mn} = \sqrt{\frac{2^{-(n+m-1)}}{\pi n! m!}} \tag{3.13}$$

H_n, H_m are the corresponding Hermite polynomials of order n and m, respectively. Some examples of HG_{nm} modes are shown in Fig. 3.1.

3.1.2 Laguerre-Gauss modes

Similarly as in Cartesian coordinates, by writing the paraxial Helmholtz equation (Eq. (3.6)) in polar coordinates one obtains the Laguerre-Gauss (LG_{lp}) basis of

[1] A collimated beam consists of an electromagnetic wave that is considered to approximately not diverge within a moderate propagation distance, typically the Rayleigh range for Gaussian beams.

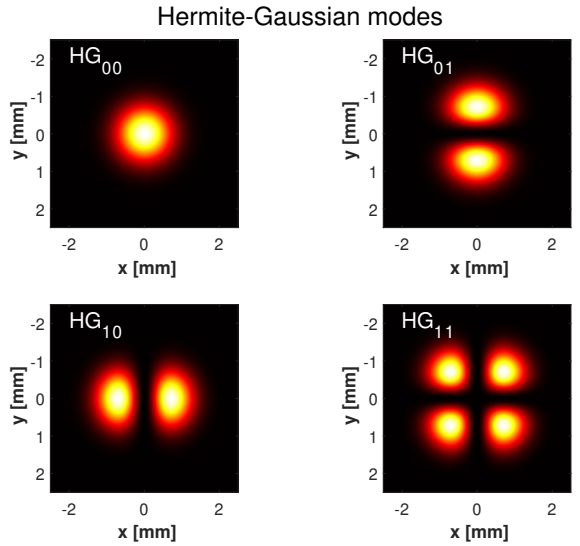

Figure 3.1: Hermite-Gauss HG_{mn} modes of order $m, n = 0, 1$,

modes given by

$$LG_{l,p}(\rho,\varphi,z) = \frac{C_{lp}^{LG}}{w(z)}\left(\frac{\sqrt{2}\rho}{w(z)}\right)^{|l|} L_p^{|l|}\left(\frac{2\rho^2}{w^2(z)}\right)\exp\left(-\frac{\rho^2}{w^2(z)}\right) \times \exp[i\zeta(z)])\exp\left(-\frac{ik\rho^2}{2R(z)}\right)\exp(-il\varphi) \tag{3.14}$$

with $L_p^s(r)$ the Laguerre polynomial, and C_{lp} the normalization constant is

$$C_{lp}^{LG} = \left(\frac{2p!}{\pi(p+|l|)!}\right)^{1/2}. \tag{3.15}$$

The Laguerre-Gaussian modes with $l \neq 0$ contains an azimuthally varying phase factor $\exp(il\varphi)$ with a phase singularity at the optical axis $rho = 0$, such that for the field to be defined, the amplitude must vanish at $\rho = 0$. This leads to a doughnut-shaped intensity profile. The profile of the mode LG_{lp} contains $p + 1$ radial nodes and l discontinuities in the azimuthal direction. Some examples of LG_{lp} modes are shown in Fig.3.2.

3.1.3 Azimuthal p-modes

From the solution to the paraxial Helmholtz equation and the decomposition in TEM modes, one can see that, in polar coordinates (r, φ), an arbitrary beam

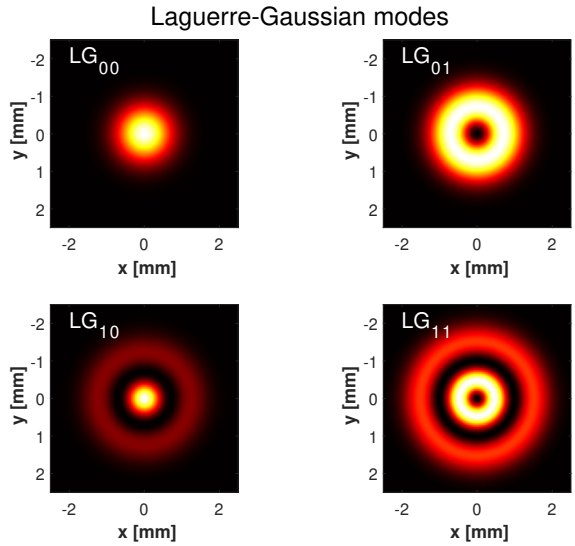

Figure 3.2: Laguerre-Gauss LG_{pl} modes of order $p, l = 0, 1$,

of light with complex amplitude $f(r, \varphi)$ can be expressed as a sum of radially-dependent amplitudes and radially-independent phases as:

$$f(r, \varphi) = \sum_p a_p(r) \exp\left(ip\varphi\right). \tag{3.16}$$

This can be interpreted as a modal decomposition in modes with amplitude $a_p(r)$ and phase $p\varphi$; in what follows, we refer to these modes as p-modes. Using this decomposition there are two parameters of particular interest, namely

$$\beta_p \sim \int r\mathrm{d}r a_p(r), \tag{3.17}$$

$$P_p = 2\pi \int r\mathrm{d}r \left|a_p(r)\right|^2. \tag{3.18}$$

The latter being the weight of the $p-$th mode so that the total power of the optical beam is

$$P = \sum_{p=-\infty}^{\infty} P_p. \tag{3.19}$$

In principle, the radial integral β_p can be zero even though the weight of mode p (i.e. P_p) is different from zero. However it has been noticed that it is difficult to find a realistic example for such a case [98].

3.2 Generation of spatial modes of light

Beam shaping using computer-generated holograms and spatial light modulators

Spatially structuring light beams has been realised by means of diffractive optical elements (DOE) that induce spatial variations to the optical path-length of the beam across its transverse section leading to amplitude and phase modulations [99]. Designing and engineering the corresponding optical element results in the generation of engineered structured beam profiles. Although arbitrary amplitude and phase modulations are often of interest, we particularily care for methods to generate spiral beams with circular symmetry as the LG_{pl} modes introduced in the previous section.

An example of DOE used for the generation of such beams are spiral phase plates (SPP) (see Fig. 3.3a), transparent materials with homogeneous refractive index and height varying azimuthally, resulting on a phase dislocation [100]. Other approach for beam shaping is based on the phase shifts that arise with local polarization of the field is transformed, for instance in inhomogeneous anisotropic media. This phenomena has led to the development of q-plates, liquid-crystal-based birefringent plates with retardation and optical axis unevenly oriented according to a distribution with topological charge q [101,102]. These devices have shown to convert spin to orbital angular momentum, resulting on the generation of an helical vortex with helicity controlled by the input beam polarization [103] (see Fig.3.3b).

Another relevant type of diffractive elements for beam shaping are computer-generated holograms (CGH) [104]. The working principle starts from considering the intensity pattern of a desired structured beam with specific phase profile (including singularities as in the case of vortex beams) combined with a reference plane wave. Initially, these interference patterns were recorded by exposure of a photographic film plate, after development of the film, the resulting device is what initially has been referred to as hologram. A first key relevant point of holograms is that they record both amplitude and phase information of the interference field in form of an intensity pattern (see Fig.3.3c). A second point, relevant for the success of holograms, is the fact that they can be computed computationally by means of inverse scattering and printed in optical filters [105]. When illuminated with a plane wave, the spatially-designed transmittance, proportional to the intensity distribution of the interference pattern, induces changes over the field such

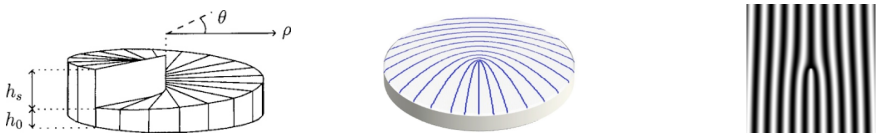

(a) Spiral Phase Plate *(b) Q-plate* *(c) Fork hologram*

Figure 3.3: Diffractive optical elements (DOE) used for beam shaping

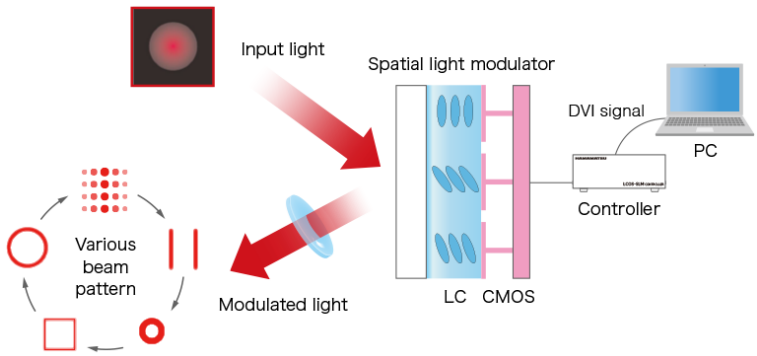

Figure 3.4: Liquid-crystal on Silicon Spatial Light Modulator (LCOS-SLM). Figure from Hamamatsu LCOS-SLM product web page.

that the intensity profile after interaction is the desired one.

Computer-generated holograms obtained big attention with the development of Liquid-Crystal on Silicon (LCoS) Spatial Light Modulators (SLM). These devices work due to fact that liquid crystals (LC) respond mechanically to electric (or magnetic) fields. When a sufficiently strong field is applied, the LC molecules tend to align with the electric field [106].

SLM are pixelated displays consisting on a transparent two-dimensional array of electrode cells filled with LC that can be controlled individually. Depending on the magnitude of the applied voltage in each electrode, the LC molecules reorder within the pixel, effectively resulting in a change of refractive index of the medium, and hence the transmittance function. There are two types of SLM, working on transmission or reflection. The difference between them is that in the latter, instead of two transparent electrode deposited on a glass substrates, one is replaced by a complementary metal–oxide–semiconductor (CMOS) chip plate, in which pixel electrodes are arranged in two dimensions (see Fig.3.4) [107]. These devices allow to display CGHs as gray-scale 8-bits images, allowing to control light digitally [108, 109]. CGH in LCoS-SLM allow to generate complex fields by effectively varying the diffraction efficiency with phase modulations [110–112] or by transferring phase modulations onto amplitude modulations using polarizing optics [113]. In what follows, we present the methods for structuring light beams using LCoS-SLM.

3.2.1 Two-steps amplitude and phase modulation

An arbitrarily shaped light beam can be generated using two SLM and polarization optics as shown in Fig. 3.5 [113]. Consider a linearly polarized light beam of spatial profile $u_0(\mathbf{x})$ propagating along the z direction. With the use of a half-wave plate (HWP) the polarization state of the beam is rotated 45° so that it has equal components of magnitude $A_0/\sqrt{2}$ in the horizontal (H) and vertical (V) direction.

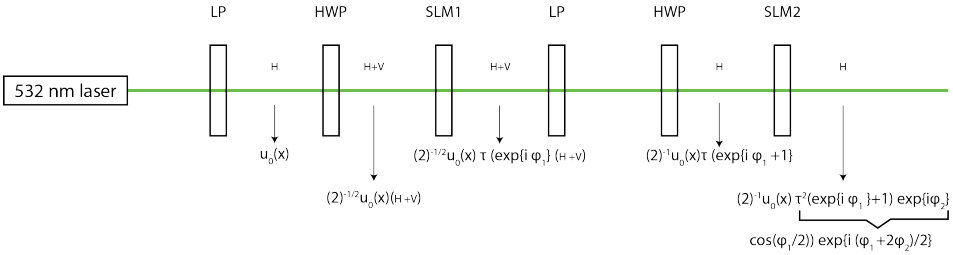

Figure 3.5: Two-step arbitrary amplitude and phase modulation of a beam with spatial profile $u_0(\boldsymbol{x})$. Using two spatial light modulators (SLMs) with transmissivity (or reflectivity) τ and polarization optics, an arbitrary complex field $u(\mathbf{x}) = \Psi(\boldsymbol{x})\exp\{i\Phi(\boldsymbol{x})\}$ is generated by imprinting the phases $\varphi_1(\boldsymbol{x})$ and $\varphi_2(\boldsymbol{x})$, respectively with the SLMs.

The beam reflected (or transmitted) by a fist spatial light modulator SLM_1 with reflectivity (or transmissivity) $\tau = 1$, imprints a phase $\varphi_1(\mathbf{x})$ to the horizontal component of the beam in the following way

$$u(\mathbf{x}) = \frac{1}{\sqrt{2}} u_0(\mathbf{x})(e^{i\varphi_1(\mathbf{x})}H + V), \tag{3.20}$$

With the use of a linear polarizer (LP) and a WHP, the polarization state is set to horizontal and the amplitude of the beam becomes $A_0(\exp(i\phi_1(\mathbf{x})) + 1)/2$. A second spatial light modulator SLM_2 imprints a phase $\varphi_2(\mathbf{x})$ so that the resulting beam is:

$$\begin{aligned} u(\mathbf{x}) &= \frac{1}{2} u_0(\mathbf{x})(e^{i\varphi_1(\mathbf{x})} + 1)\, e^{i\varphi_2(\mathbf{x})} \\ &= u_0(\mathbf{x}) \cos\Big(\frac{\varphi_1}{2}\Big) \exp\Big\{ i\Big(\frac{\varphi_1(\mathbf{x}) + 2\varphi_2(\mathbf{x})}{2}\Big)\Big\}. \end{aligned} \tag{3.21}$$

Hence, after the second SLM the amplitude and phase of the beam can be engineered by selecting the appropiate phases φ_1 and φ_2. To generate abeam with amplitude $\psi(x)$ and phase $\phi(x)$,

$$u(\mathbf{x}) = \psi(\mathbf{x})\exp\{i\phi(\mathbf{x})\}, \tag{3.22}$$

the field must gain the following phases after passing through the SLM,

$$\varphi_1(\mathbf{x}) = 2\arccos\frac{\psi(\mathbf{x})}{u_0(\mathbf{x})}, \tag{3.23}$$

$$\varphi_2(\mathbf{x}) = \frac{\phi(\mathbf{x}) - \varphi_1(\mathbf{x})}{2}. \tag{3.24}$$

Tailoring light beams with this method has been proposed for generation and steering of photonic nanojets (PNJ) when probing micro-scale dielectric lenses

[114]. A handicap of this technique is the fact that SLM are not fully efficient. Due to the pixelated structure of the display, light sees the surface of the SLM as a two-dimensional diffraction grating. Moreover, the spacing between the pixels is not completely negligible, so that a small, but significant component of the beam remains undiffracted by the CGH. Depending on the device, and the wavelenght of the light beam, this can represent between a 5% and a 20% of the power. Although for some applications this effect might be relevant, for beam shaping could be a drawback.

Moreover, SLM can generate pixelated 8-bit and 10-bit phase-maps (such as $\varphi_1(\mathbf{x})$ and $\varphi_2(\mathbf{x})$ above) with an arbitrary phase distribution of values discretized in steps of 2π rad/255 $\approx$ 24.6 mrad ($\approx$1.4°) and 2π rad/1023 $\approx$ 6.1 mrad ($\approx$ 0.35°) respectively. The actual performance depends on the model of the SLM and on the operating wavelength. For example, the 8-bit Hamamatsu LCOS-SLM X13138-07 admits the band of wavelengths from 620 to 1100 nm with 80% light utilization efficiency at 633 nm, resulting in phase steps of approximately 52.7 mrad ($\approx$3°).

3.2.2 One-step amplitude and phase modulation

Complex fields can also be generated using a single phase-only CGH. The method consists on two main principles. The first one is to add a digital blazed grating to the CGH such that the zeroth and the first diffraction orders are spatially separated by an angle proportional to the spatial frequency of the grating (inverse to the period) [110]. The second principle consists on varying the depth of the phase distribution on the CGH as a bias function in such a way that the light that is not diffracted by the hologram into the first order, goes to the zeroth order. These two principles combined allow to effectively tailor the amplitude distribution of either the zeroth or the first diffraction orders [111]. A schematic representation of the phase modulation is presented in figure 3.6. The performance of this technique for complex field generation compromises the relative intensity of the high-order diffraction field contributions that share the spatial frequency domain of the encoded field [112].

Suppose one wants to generate an arbitrary field as in Eq. (3.22). Without losing generality assume that the amplitude $\psi(x)$ and phase $\phi(x)$ take values in the intervals $[0, 1]$ and $[-\pi, \pi]$ respectively. A CGH displayed on a phase-only SLM corresponds to a DOE with transmission function

$$T_h(\mathbf{x}) = \exp[i\eta(\psi(\mathbf{x}), \phi(\mathbf{x}))]. \tag{3.25}$$

Where $\eta(\psi(\mathbf{x}), \phi(\mathbf{x}))$ is the actual hologram modulation depending on the amplitude and phase of the desired field. The keypoint of this technique is to express Eq. (3.25) in terms of its Fourier series in the phase domain as

$$T_h(\mathbf{x}) = \sum c_q \exp(iq\phi), \tag{3.26}$$

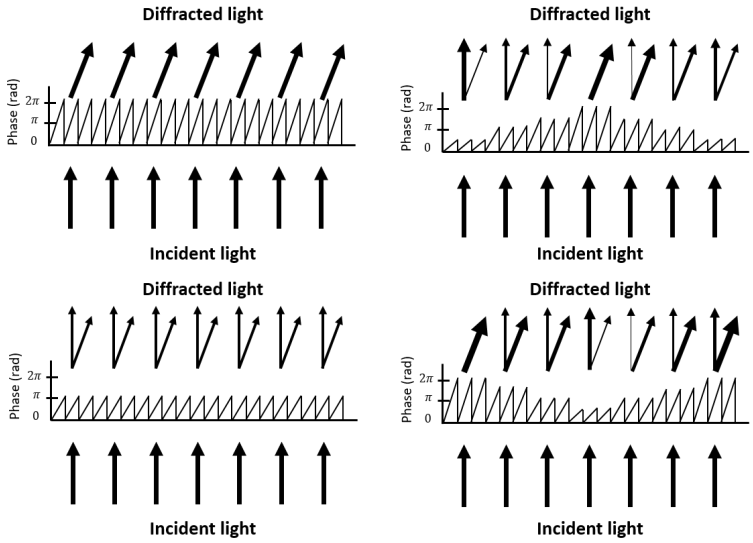

Figure 3.6: Amplitude and phase modulation through modulation depth variations using a single computer generated hologram (CGH).

where

$$c_q = \frac{1}{2\pi}\int_{-\pi}^{\pi} \exp[i\eta(\psi,\phi)]\,\exp[-iq\phi]\mathrm{d}\phi. \tag{3.27}$$

The explicit dependence ($\mathbf{x}$) of the amplitude ψ and phase ϕ is not included to avoid notation. After integration of Eq. (3.27), c_q explicitly depend on the amplitude $\psi(x)$. Thus, keeping the first term of the expansion in Eq. (3.26), one sees that $c_1 = \alpha\,\psi(\mathbf{x})$. Note that the maximum value of the integral (3.27) is 2π, thus the maximum value of α is 1, which limits the efficiency of the CGH.

Consider the phase modulation given by

$$\eta(\psi,\phi) = f(\psi)\,\sin(\phi). \tag{3.28}$$

Substituting in the Fourier expansion in Eq. (3.26), one gets

$$T_h(\mathbf{x}) = \sum_{m=-\infty}^{\infty} J_m[f(\psi)]\,\exp(im\phi). \tag{3.29}$$

Where J_m denotes the Bessel function of integer order m according to the Jacobi–Anger identity [115]:

$$\exp\Big(iz\sin\varphi\Big) = \sum_{m=-\infty}^{\infty} J_m(z)\exp\Big[im\varphi\Big], \tag{3.30}$$

or similarly

$$\exp\Big(iz\cos\varphi\Big) = \sum_{m=-\infty}^{\infty} i^m\, J_m(z)\exp\Big[im\varphi\Big]. \tag{3.31}$$

From the expanssion it follows that

$$c_q = J_q[f(\psi)], \tag{3.32}$$

which implies

$$c_1 = J_1[f(\psi)] = \alpha\psi. \tag{3.33}$$

The value of α is such that the maximum value for Eq. (3.33) to hold is for $\alpha \approx 0.5819$, which corresponds to the maximum value of the first Bessel function $J_1(x)$. This is valid for every value of the amplitude ψ in the interval $[0, 1]$ by taking the appropriate value of $f(\psi)$ in the domain $[0, x_1]$, where $x_1 \approx 1.84$. The function $f(\psi)$ can be computed by numerically inverting Eq. (3.33). It is important to note that this CGH can be implemented with phase modulation in a reduced domain $[-f_0\pi, f_0\pi]$, with $f_0 \approx 0.586$, thus, the phase range necessary for the SLM to cover is $\Delta\phi = 2f_0\pi \sim 1.17\pi$.

3.3 Spatial spectroscopy. Using spatial modes for metrology and sensing.

In this section we explore the use of spatial modes in optical metrology either for detection of spatial mode components as introduced in Section 3.1 (spatial mode demultiplexing, wavefront reconstruction or hyperspectral imaging) or probing with specific spatial modes generated using computer-generated holograms displayed on liquid crystal spatial light modulators as presented in Section 3.2.

Let us start by consider an arbitrary field of interest characterized by a set of parameters $\{\theta_i\}$. In the frame of optical metrology, the field could be associated to a probe beam scattered by an object with specific spatial features of interest. As pointed out in Eq. (3.9), the field can be decomposed as a linear combination of spatial mode components $\{\gamma_i(x)\}$ as

$$U(r;\theta) = \sum_{i=-\infty}^{\infty} \Gamma_i(\theta)\,\gamma_i(x), \tag{3.34}$$

where $C_i(\theta)$ are the complex decomposition coefficients that depend on the set of parameters $\theta = (\theta_1, \theta_2, ..., \theta_n)$ and can be computed as:

$$\Gamma_i(\theta) = \int U(r;\theta)\,\gamma_i^*(r)\,\mathrm{d}r. \tag{3.35}$$

It is of interest of this section, to address techniques to measure the modal components of the field (3.34). Note that, since the complex coefficients carry information

of the parameters, one can select an adequate set of modes so that sensing some of the components might be sufficient to determine the parameters of interest. Two considerations are relevant for a convenient selection of the set of modes:

- The accurate experimental realization of the spatial modes must be feasible
- The number of modes carrying the most of the information about the parameters must be countable and as small as possible

Concerning the first consideration, a convenient set of spatial modes with cylindrical symmetry that has received a lot of attention in the last two decades is the Laguerre-Gauss (LG) basis [116]. These modes have been used for imaging purposes [117–120]. Furthermore, these modes can be realised using laser beams and CGH in LCoS-SLMS as described in Section 3.2.

By measuring combinations of different modes one can also have access to the phase of the coefficients. For instance, this has been done to estimate the size and orientation of an object (opening angle). With the amplitude of the coefficients one can determine the aperture angle, whilst by measuring the phase one has access to its orientation [119]. The decomposition of a beam has also been measured using other basis of functions as the Hermite-Gaussian basis [63, 95] or some other engineered basis [121].

Regarding the second consideration, in general the field expansion is a superposition of an infinite (or at least very large) number of modes. To measure all the coefficients of a large number of modes is neither easy nor ideal. Previous knowledge about what are the most relevant modes would simplify the measurement. Determining only those mode coefficients could be sufficient to estimate the desired parameters [122].

To measure the amplitude and phase of such modes experimentally, Delaubert et al. [19,20] considered a *homodyne detection scheme* to measure the displacement and tilt of a Gaussian beam. In this particular case, the beam can be seen as a sum of an on-axis Gaussian beam (TEM_{00}) plus an Hermite-Gaussian mode of order one (TEM_{10}) whose amplitude and phase contains information on the displacement and tilt parameters. By combining the tilted and displaced beam with a local oscillator beam with the TEM_{10} mode shape, they estimated the two parameters of interest. In their experiments there are two particular aspects that it is not evident how, if possible, can be applied to more general scenarios:

- First, even though there are two parameters to be estimated (displacement and tilt), the spatial mode associated to both parameters turns out to be the same. This is not the case in general.
- Second, the values of both parameters were determined by the real (displacement) and imaginary (tilt) parts of the TEM_{10} coefficient. Therefore varying the phase of the local oscillator they could estimate independently the two parameters. It is not obvious that this scheme applies generally.

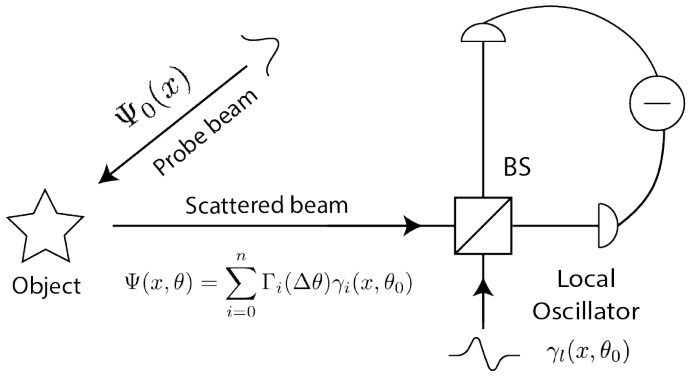

Figure 3.7: Optical metrology through spatial mode sensing using a homodyne spatial mode analyzer. A probe beam with spatial distribution $\Psi_0(x)$ illuminates an object characterized by n parameters $\theta = (\theta_1, \theta_2, ..., \theta_n)$. The spatial shape of the scattered beam can be decomposed as $\Psi(x, \Delta\theta) = \sum_{i=0}^{n} \Gamma_i(\Delta\theta)\gamma_i(x, \theta_0)$. Here $\Delta\theta = \theta - \theta_0$, with θ_0 a value of reference of the parameters close to θ, the unknown spatial feature imprinted in the probe beam after interaction with the object. The beam is combined with a local oscillator holding a single spatial mode $\gamma_l(x, \theta_0)$ of the particular set of modes. The signals at the output ports of the beamsplitter are subtracted in a standard homodyne detection scheme. By varying the phase of the local oscillator one can retrieve the real and imaginary parts of the coefficients $\Gamma(\Delta\theta)$ and determine the system's parameters θ.

In the following, we generalize these results to implement a *homodyne spatial mode analyzer*. The general concept is shown in figure 3.7, in which combining the signal beam with a local oscillator holding different engineered spatial modes, one could determine the parameters of interest optimally. This technique in what we call *Spatial Spectroscopy*. In the standard (time domain) spectroscopy one illuminate the sample of interests with light containing many appropriate wavelengths (frequencies) components across the spectrum (hyperspectral imaging might consider a hundred or more wavelengths). In spatial spectroscopy one chooses several engineered spatial modes to extract particular information about the structure of the object. The results hereby presented have been presented have been published in a conference proceedings publication of which the author of this dissertation is first author [123].

3.3.1 Homodyne spatial mode analyzer

To measure the coefficients in Eq. (3.35) of the modal decomposition in Eq. (3.34) we consider a homodyne spatial mode analyzer as schematized in figure 3.8 [63, 95]. With the help of a beamsplitter, the beam of interest is combined with a local oscillator holding the spatial mode γ_i. The two output signals of the beamsplitter are subtracted from each other in a standard homodyne detection scheme. The so called *differential signal* contains the mode component of the

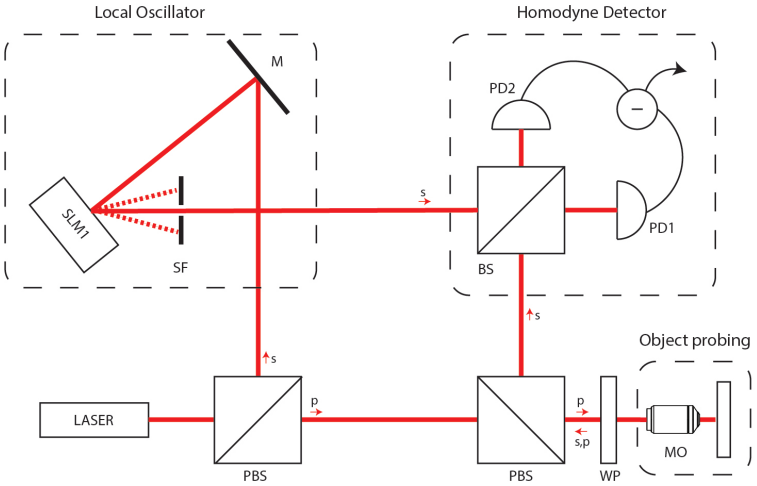

Figure 3.8: Homodyne spatial mode analyzer. A probe beam with linear polarization state (p) illuminates a sample using a microscope objective (MO). The reflected (transmitted) beam is combined with a local oscillator (LO) mode generated with a spatial light modulator (SLM) using a beam splitter (BS). The output signals are subtracted in a standard homodyne detection scheme.

probe beam corresponding to the local oscillator mode [19, 20, 122, 124, 125].

Without losing generality, let us consider a quantum-mechanical formulation to describe the working principle of the proposed technique. Needless to say, the formalism applies classically as well. Let us express the positive frequency electric field operator of the local oscillator holding the spatial mode $\gamma_l(x)$ in the following way

$$\hat{\mathcal{E}}_l^+(x) = i\sqrt{\frac{\hbar\omega}{2\varepsilon_0 cT}}\hat{a}_l\,\gamma_l(x). \tag{3.36}$$

Here $\hbar\omega/2\varepsilon_0 cT$ is the intensity of a single photon, T the integration time of the detector, $\hat{a}_j$ are the annihilation field operators of the electromagnetic modes. Similarly, the operator defining the probe beam in state (3.34) is

$$\hat{\mathcal{E}}_a^+(x) = i\sqrt{\frac{\hbar\omega}{2\varepsilon_0 cT}}\sum_j c_j\hat{a}_j\gamma_j(x). \tag{3.37}$$

The average homodyne differential signal when setting the mode $\gamma_l(x)$ in the local oscillator is

$$\langle\hat{S}\rangle = \frac{\hbar\omega}{\varepsilon_0 cT}\sqrt{N\,N_{LO}}\,\left[\mathrm{Im}\{\Gamma_l\}\cos\Delta\varphi - \mathrm{Re}\{\Gamma_l\}\sin\Delta\varphi\right], \tag{3.38}$$

where $\Delta\varphi = \varphi_l(x) - \varphi_{LO}$ is the phase difference between the two inputs of the beam splitter. N and N_{LO} are the number of photons collected by the detector

in the time T from the signal beam and the local oscillator, respectively. The variance of the differential signal is defined by

$$Var(\hat{S}) = \langle \hat{S}^2 \rangle - \langle S \rangle^2 = \left(\frac{\hbar\omega}{2\epsilon_0 cT} \right)^2 (N|\Gamma_l|^2 + N_{LO}). \tag{3.39}$$

Considering the number of photons in the local oscillator to be much larger than the number of photons of the scattered beam ($N_{LO} \gg N$) the signal to noise ratio (SNR) is approximately $\sqrt{N}|\Gamma_l|$. Note that by varying the phase difference φ_{LO} and measuring at the critical values $(0, \pi/2, \pi, 3\pi/2, 2\pi)$ one can determine the component of the field in the mode of the local oscillator since the complex coefficients Γ_l are retrieved. By selecting different modes, one at a time, one can determine the full (amplitude and phase) modal decomposition of the field from Eq. (3.34).

3.3.2 Encoding phase information of azimuthal modes

We consider an optical beam that passes through a phase-only SLM encoding a CGH as in Eqs.(3.25) and (3.28) from Section 3.2. Explicitly, let us consider a transmission function of the form [126]

$$T_0(x,y) = \exp\left[i\alpha_0 \sin\left(p\varphi - \frac{2\pi}{\Lambda} x \right) \right] = \exp\left[i\alpha \sin\left(p\varphi - \frac{2\pi}{\Lambda} r\cos\varphi \right) \right] \tag{3.40}$$

where α_0 is the amplitude of the modulation, p is an integer associated to the winding number of the azimuthal mode, Λ is the period of the digital blazed grating as introduced in Section 3.2.2. A different type of transmission function to generate vortex beams is considered in Appendix C where a comparison to the results discussed in this section are included. For a phase hologram with global phase $k\beta$ and modulation depth $k\alpha$ one has

$$\begin{aligned} T(x,y) &= \exp\left[ik\delta + ik\alpha \sin\left(p\varphi - \frac{2\pi}{\Lambda} r\cos\varphi \right) \right] \\ &= \exp\left(ik\delta \right) \sum_m J_m(k\alpha) \exp\left[im\left(p\varphi - \frac{2\pi}{\Lambda} r\cos\varphi \right) \right] \end{aligned} \tag{3.41}$$

We have made use of the Jacobi-Anger expansion (3.30). Let us consider a 2f imaging system with focal length f after the hologram as shown in figure 3.9. For an input beam $U_0(r,\varphi)$ the field at the Fourier plane after the Fourier lens, using with cylindrical coordinates (ρ,θ), is

$$U(\rho,\theta) = \frac{i\exp(2ikf)}{\lambda f} \int r\mathrm{d}r\, \mathrm{d}\varphi\, U_0(r,\varphi) T(r,\varphi) \exp\left[i\frac{k\rho}{f} r\cos(\theta-\varphi) \right]. \tag{3.42}$$

Considering the transmission function is as in Eq. (3.40) we get

$$\begin{aligned} U(\rho,\theta) &= iq_f \int r\mathrm{d}r\, \mathrm{d}\varphi\, U_0(r,\varphi) T(r,\varphi) \exp\left[i\frac{k\rho}{f} r\cos(\theta-\varphi) \right] \\ &= iq_f \sum_m t_m \int r\mathrm{d}r\, \mathrm{d}\varphi\, U_0(r,\varphi) \exp\left[imp\varphi \right] \exp\left[i\frac{k\rho_m}{f} r\cos(\theta_m-\varphi) \right] \end{aligned} \tag{3.43}$$

where $q_f = \frac{\exp(2ikf)}{\lambda f}$ and we have used the coordinates of the m-th diffraction order (ρ_m, θ_m) [126–128]

$$\rho_m^2 = \rho^2 + \Big(\frac{m\lambda f}{\Lambda}\Big)^2 \mp \frac{2m\lambda\rho f}{\Lambda}\cos\theta \tag{3.44}$$

and

$$\tan\theta_m = \frac{\rho\sin\theta}{\rho\cos\theta \mp m\frac{\lambda f}{\Lambda}}. \tag{3.45}$$

The $\mp$ signs corresponds to positive and negative diffraction orders m, respectively. From Eqs. (3.44) and (3.45) we have

$$\rho_m \sin\theta_m = \rho\sin\theta \tag{3.46}$$

and

$$\rho_m \cos\theta_m = \rho\cos\theta \mp m\frac{\lambda f}{\Lambda} \tag{3.47}$$

To verify the equivalence of the coordinates in Eqs. (3.44) and (3.45) according to Eqs.(3.46) and (3.47), we have

$$\begin{aligned}
&\frac{k\rho_m}{f} r\cos(\theta_m - \varphi) = \frac{k\rho_m}{f} r\Big[\cos\theta_m\ \cos\varphi + \sin\theta_m\ \sin\varphi\Big] \\
&= \frac{k\rho_m}{f} r\Big[\frac{\cos\varphi}{\rho_m}\Big(\rho\cos\theta - m\frac{\lambda f}{\Lambda}\Big) + \sin\varphi\frac{\rho\sin\theta}{\rho_m}\Big] \\
&= \frac{k\rho}{f}\, r\cos\Big(\varphi - \theta\Big) - m\frac{2\pi}{\Lambda} r\cos\varphi,
\end{aligned} \tag{3.48}$$

which shows that the equivalence holds in Eq. (3.44).

Determination of the coefficients at the Fourier plane origin

Consider an arbitrary input beam

$$U_0(\rho,\varphi) = A_0(\rho)\exp(il\varphi) \tag{3.49}$$

The field in the Fourier plane after the $2f$ system is

$$U(\rho,\varphi) = \sum U_m(\rho_m, \varphi_m) \tag{3.50}$$

where

$$\begin{aligned}
&U_m(\rho_m,\theta_m) = t_m q_f \int r\mathrm{d}r\,\mathrm{d}\varphi\, A_0(r)\exp\Big[imp\varphi\Big]\exp\Big[i\frac{k\rho_m}{f} r\cos(\theta_m - \varphi)\Big] \\
&= it_m q_f \int r\mathrm{d}r\,\mathrm{d}\varphi\, A_0(r)\exp\Big[i(l+mp)\varphi\Big]\sum_n i^n J_n\Big(\frac{k\rho_m}{f} r\Big)\exp\Big[in(\theta_m - \varphi)\Big] \\
&= i^{s+1}\, 2\pi\, t_m q_f \int r\mathrm{d}r\, A_0(r) J_s\Big(\frac{k\rho_m}{f} r\Big)\exp\Big[is\theta_m\Big]
\end{aligned} \tag{3.51}$$

with $s = l + mp$. Note that the field (3.51) corresponds to a vortex beam with topological charge $s = l + mp$. For the sake of simplicity, we restrict to the case $m > 0$. If we express the input beam (3.49) as a decomposition of azimuthal modes

$$U_0(\rho, \varphi) = \sum_l a_l(r) \exp\big(il\varphi\big). \tag{3.52}$$

Substituting explicitly q_f, the field of the m-th diffraction order is:

$$U_m(\rho_m, \theta_m) = \frac{2\pi\, it_m \exp(2ikf)}{\lambda f} \int r\mathrm{d}r\, a_l(r) \exp\Big[i\frac{k\rho_m}{f} r\cos(\theta_m - \varphi)\Big], \tag{3.53}$$

where the integration over the angular variable has been carried out. At $\rho_m = 0$ we have

$$U_m(\rho_m = 0) = \frac{2\pi\, it_m \exp(2ikf)}{\lambda f} \int r\mathrm{d}r\, a_p(r) \tag{3.54}$$

Note that when measuring the intensity at $\rho_m = 0$ we obtain

$$|U_m(\rho_m = 0)|^2 = \Big(\frac{2\pi}{\lambda f}\Big)^2 |t_m|^2 \Big| \int r\mathrm{d}r\, a_p(r)\Big|^2 \tag{3.55}$$

The complex coefficients of interest are

$$\beta_m = \frac{1}{\lambda f} \int r\mathrm{d}r\, a_m(r). \tag{3.56}$$

In principle, the radial integral β_m can be zero even though the weight of mode m, i.e., P_m, is different from zero. However it has been noticed that it is difficult to find a realistic example of when this is the case [98].

Projection onto the Gaussian mode

To measure coefficients of the azimuthal mode decomposition (3.52), we project the field $U_m(\rho_m, \theta_m)$ into the (TEM_{00}) Gaussian mode

$$V_0(\rho_m) = \frac{1}{\sqrt{\pi w_1^2}} \exp\Big[-\frac{\rho_m^2}{2w_1^2}\Big], \tag{3.57}$$

which can be done by coupling into a single-mode fiber with the help of the appropriate optical system (see Fig. 3.9). The power detected after projection (propagation through the fiber) is

$$P_d = |\gamma_{mp}|^2 |t_m|^2 P_0, \tag{3.58}$$

where

$$\gamma_{mp} = 4\pi^2\, q_f\, \frac{i^{1-mp}}{\sqrt{\pi w_1^2}} \int r\,\mathrm{d}r \int \rho_m\,\mathrm{d}\rho_m\, a_{mp}(r)\, J_0\Big(\frac{k\rho_m}{f} r\Big) \exp\Big[-\frac{\rho_m^2}{2w_1^2}\Big]. \tag{3.59}$$

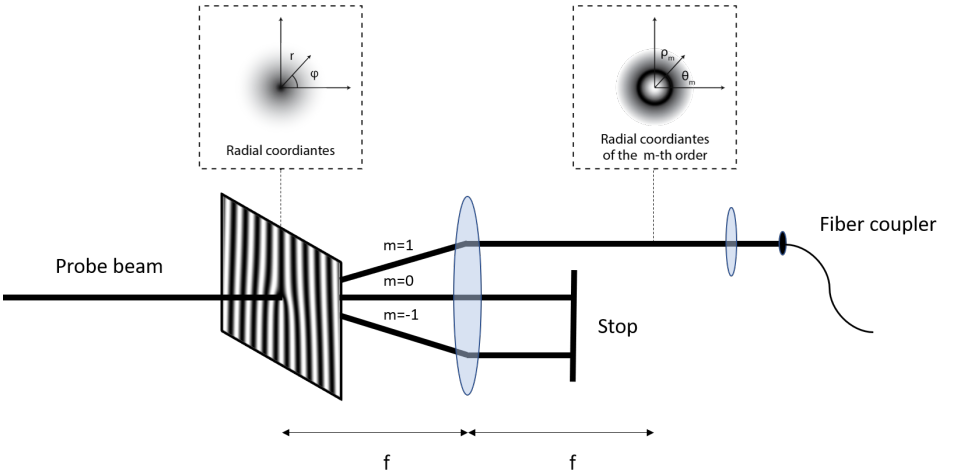

Figure 3.9: Experimental scheme for projection of the the $m-th$ diffraction order $U_m(\rho_m, \theta_m)$ of an input beam $U_0(\rho, \theta)$ after passing through an SLM with transfer function $T(r, \varphi)$ encoding information of an azimuthal mode.

Using the identity

$$\int x\,\mathrm{d}x\, J_0(\alpha x) \exp\Big[-\gamma^2 x^2\Big] = \frac{1}{2\gamma^2} \exp\Big[-\frac{\alpha^2}{4\gamma^2}\Big], \tag{3.60}$$

substituting q_f and excluding the overall and constant phase factor $\exp(2ikf)$ i^{1-mp} since the measurable quantity is in fact $|\gamma_{mp}|^2$, the projection γ_{mp} becomes

$$\gamma_{mp} = \frac{(2\pi)^2}{\lambda f} \frac{w_1^2}{\sqrt{\pi w_1^2}} \int r\,\mathrm{d}r\, a_{mp}(r) \exp\Big[-\Big(\frac{2\pi}{\lambda f}\Big)^2 w_1^2 \frac{r^2}{2}\Big]. \tag{3.61}$$

3.4 Measurement of the position of a Gaussian beam using spatial mode projections

Delaubert et al. [19, 20] considered a *homodyne detection scheme* to measure the displacement and tilt of a Gaussian light beam. They restricted their attention to the case of displacements along a line, in which the beam can be seen as a sum of an on-axis Gaussian beam (TEM_{00}) plus an Hermite-Gaussian mode of order one (TEM_{10}). The amplitude and phase of the mode projection into the mode TEM_{10} contains information on the displacement and tilt parameters.

In this section, we aim at going further from Delaubert's results, this is, to localize the beam in the transverse plane by encoding modal information in the phase of the beam, not relying in the fact that only one mode contains the desired information.

We start by considering a Gaussian beam with waist w_0 displaced from $\vec{\rho} = (\rho\cos\varphi, \rho\sin\varphi)$ to $\vec{\rho'} = (\rho\cos\varphi - d_x, \rho\sin\varphi - d_y)$. Using polar coordinates the beam can be written as:

$$\Psi(\rho,\varphi) = \left(\frac{2}{\pi w_0^2}\right)^{1/4} \exp\left\{\frac{-|\vec{\rho'}|^2}{w_0^2}\right\} \tag{3.62}$$

with $|\vec{\rho'}| = (\rho^2 + d_x^2 + d_y^2 - 2\rho d_x\cos\varphi - 2\rho d_y\sin\varphi)^{1/2}$. In order to estimate the position (ρ,φ) in the transverse plane of a Gaussian light beam, we consider the use of Laguerre-Gauss spatial modes, that can be written as

$$LG_m(\rho,\varphi) = A_m U_m(\rho)\exp(im\varphi)\,. \tag{3.63}$$

A_m is a coefficient related to the power carried by the spatial mode, U_m describes the radial dependence of the spatial shape and m is the winding number that describes the characteristic azimuthal dependence of the spatial shape of the mode. Projecting the light beam described by equation (3.62) onto the $LG(\rho,\varphi)$ modes (3.63), one can determine the position of the beam by measuring the amplitude (or the phase) of the coefficients of the LG mode components if the beam is displaced radially (or azimuthally).

Furthermore, it is possible to measure the orientation of an object irrespective of its shape by measuring the phase φ_m of the Laguerre-Gauss (LG_m) component of the light scattered by the object. The function $f(\rho,\varphi)$ designates the spatial shape of the light scattered from the object. The coefficients C_m of the mode decomposition are

$$C_m = \int_0^\infty \rho\mathrm{d}\rho \int_0^{2\pi} \mathrm{d}\varphi\, f(\rho,\varphi)U_m(\rho)\exp(-im\varphi) \tag{3.64}$$

A change of orientation φ_0 of the object is reflected in a corresponding change of the spatial shape of the scattered beam that now is $f(\rho,\varphi-\varphi_0)$. The new coefficient C'_m is

$$\begin{aligned} C'_m &= \int_0^\infty \rho\mathrm{d}\rho \int_0^{2\pi} \mathrm{d}\varphi\ f(\rho,\varphi-\varphi_0)U_m(\rho)\exp(-im\varphi) \\ &= \int_0^\infty \rho\mathrm{d}\rho \int_{-\varphi_0}^{2\pi-\varphi_0} \mathrm{d}\varphi\ f(\rho,\varphi)U_m(\rho)\exp(-im\varphi - im\varphi_0) \\ &= C_m\exp(-im\varphi_0) \end{aligned} \tag{3.65}$$

In other words, the modulus of the coefficient C_m remains unchanged when the object changes its orientation, while its phase changes as $m\varphi_0$. This result allows us to differentiate, by mere inspection of the phase of a coefficient of the mode expansion, between two objects of identical shape but being oriented differently. One can make use or two or more modes with different values of m, and confirm the expected m dependence of the phase measured, to check that the phase observed in coming from a change of orientation indeed. In this section we combine the two results mentioned above for two-dimensional localization of an optical beam along a transverse plane.

3.4.1 Measurement of the beam displacement

Consider a Gaussian beam displaced a distance $d = \sqrt{d_x^2 + d_y^2}$ in the transverse plane, in the direction $\varphi_0 = \arctan(d_y/d_x)$ with respect to the horizontal axis. We can write the field of the beam as

$$U(r,\varphi) = \sqrt{\frac{P_0}{\pi w_0^2}}\, \exp\Big[-\frac{r^2}{2w_0^2}\Big] \exp\Big[\frac{rd\cos(\varphi-\varphi_0)}{w_0^2}\Big] \exp\Big[-\frac{d^2}{2w_0^2}\Big]. \tag{3.66}$$

Using

$$\exp\Big[\frac{rd\cos(\varphi-\varphi_0)}{w_0^2}\Big] = \sum_l I_l\Big(\frac{rd}{w_0^2}\Big) \exp\Big[il(\varphi-\varphi_0)\Big], \tag{3.67}$$

where I_l is the first-order modified Bessel functions or order l, the field is reduced to

$$\begin{aligned} U(r,\varphi) &= \sqrt{\frac{P_0}{\pi w_0^2}}\, \exp\Big[-\frac{d^2}{2w_0^2}\Big] \\ &\quad \times \sum_l \exp\Big[-\frac{r^2}{2w_0^2}\Big] I_l\Big(\frac{rd}{w_0^2}\Big) \exp\Big(-il\varphi_0\Big) \exp\Big(il\varphi\Big). \end{aligned} \tag{3.68}$$

For $d_x = d_y = 0$, using the decomposition in Eq. (3.16) we have $U_0(r,\varphi) = \sqrt{P_0}\, a_0(r)$, which corresponds to a single term for $p = 0$

$$a_0(r) = \frac{1}{\sqrt{\pi w_0^2}} \exp\Big[-\frac{r^2}{2w_0^2}\Big]. \tag{3.69}$$

Consider the first diffraction order $m = 1$ and the projection onto the Gaussian mode in Eq. (3.57), from Eq. (3.61) we obtain

$$\gamma_0 = \frac{(2\pi)^2}{\lambda f} \frac{1}{\sqrt{\pi w_0^2}} \frac{w_1^2}{\sqrt{\pi w_1^2}} \int r\,\mathrm{d}r\, \exp\Big(-\frac{r^2}{2w_0^2}\Big) \exp\Big[-\Big(\frac{2\pi}{\lambda f}\Big)^2 w_1^2 \frac{r^2}{2}\Big]. \tag{3.70}$$

Note that if the waist of the Gaussian projection mode in Eq. (3.57) is

$$w_1 = w_0' = \frac{\lambda f}{2\pi} \frac{1}{w_0}, \tag{3.71}$$

we obtain

$$\gamma_0 = \frac{2\pi}{\lambda f} \frac{\pi[w_0']^2}{\sqrt{\pi[w_0']^2}} \frac{w_1^2}{\sqrt{\pi w_1^2}} = \frac{2\pi}{\lambda f}\, w_0 w_0' = 1 \tag{3.72}$$

The power detected is $P_d = |t_1|^2 P_0$, as expected for this case. We notice that the important parameter to determine is γ_p for an arbitrary beam $U(r,\varphi)$, explicitly

$$\gamma_p = \frac{(2\pi)^2}{\lambda f} \frac{w_1}{\sqrt{\pi}} \int r\,\mathrm{d}r\, a_p(r) \exp\Big[-\frac{1}{2}\Big(\frac{2\pi}{\lambda f}\Big)^2 w_1^2\, r^2\Big], \tag{3.73}$$

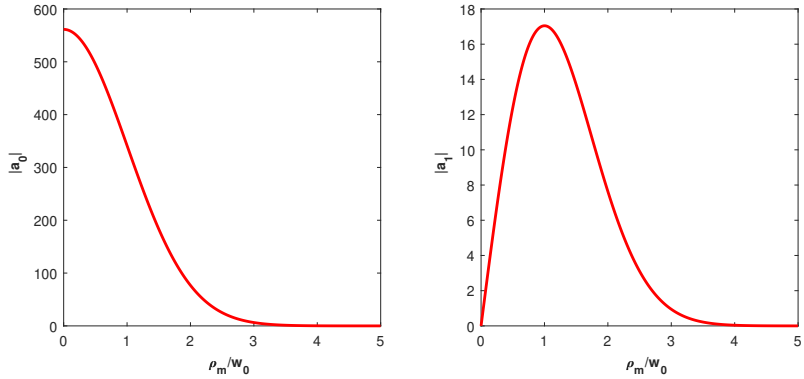

Figure 3.10: Radially-dependent amplitudes $a_0(\rho)$ and $a_1(\rho)$ of the azimuthal mode decomposition of a Gaussian beam of waist w_0 displaced a distance d.

where the radially-dependent amplitudes of the decomposition $a_p(r)$ as shown in figure 3.10 are given by

$$a_p(r) = \frac{1}{2\pi}\int \mathrm{d}\varphi\, U(r,\varphi)\, \exp(-ip\varphi). \tag{3.74}$$

Since the total power of the beam is $P_0 = \sum_l P_p = 2\pi\, P_0 \sum_p \int r\mathrm{d}r|a_p(r)|^2$, we should have

$$2\pi \sum_p \int r\,\mathrm{d}r\,|a_p(r)|^2 = 1. \tag{3.75}$$

Note that for non-zero displacements, the radially-dependent amplitude function $a_p(r)$ in Eq. (3.74) reduces to

$$a_p(r) = \frac{1}{\sqrt{\pi w_0^2}}\, \exp\Big[-\frac{r^2}{2w_0^2}\Big] I_p\Big(\frac{rd}{w_0^2}\Big) \exp\Big[-\frac{d^2}{2w_0^2}\Big]\, \exp\Big(-ip\varphi_0\Big). \tag{3.76}$$

In Figure 3.10 we show the functions a_0 and a_1 for the case in which the displacement is $d < 0.1\, w_0$.

We are specially interested the small displacement regime, in particular, for $rd/w_0^2 \ll \sqrt{p+1}$ the following identity follows

$$I_p\Big(\frac{rd}{w_0^2}\Big) = \frac{1}{\Gamma(p+1)}\Big(\frac{rd}{2w_0^2}\Big)^p. \tag{3.77}$$

The parameter of interest γ_p in this case is

$$\gamma_p = \frac{(2\pi)^2}{\lambda f}\frac{w_1}{\pi w_0}\, \exp\Big\{-\frac{d^2}{2w_0^2}\Big\}\, \exp\{-ip\varphi_0\}\, \Omega_p(d), \tag{3.78}$$

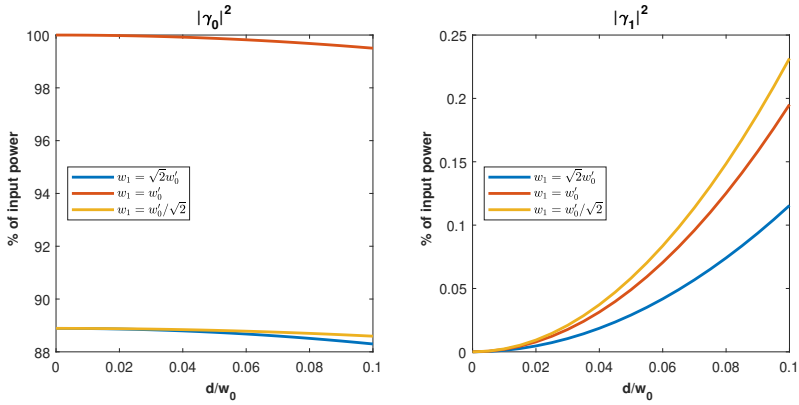

Figure 3.11: Power in the first diffraction order ($m = 1$) detected (as % of $P_0|t_1|^2$). The probe is a Gaussian beam with waist w_0 displaced a distance d that passes through a SLM with transfer function $T_p(r, \varphi)$. The beam is then projected onto a Gaussian mode with beam waist $w_1 = w_0' = \frac{\lambda f}{2\pi}\frac{1}{w_0}$, $w_1 = \sqrt{2}w_0'$ and $w_1 = w_0'/\sqrt{2}$.

where

$$\Omega_p(d) = \frac{1}{\Gamma(p+1)} \int_0^\infty r dr \, \exp\Big[-\frac{r^2}{2w_0^2}\Big] \Big(\frac{rd}{2w_0^2}\Big)^p \exp\Big[-\frac{1}{2}\Big(\frac{2\pi}{\lambda f}\Big)^2 w_1^2 \, r^2\Big]. \tag{3.79}$$

For the cases of interest $p = 0$ and $p = 1$, using Eq. (3.78) we have

$$\gamma_0 = \frac{(2\pi)^2}{\lambda f}\frac{w_1}{\pi w_0} \exp\Big\{-\frac{d^2}{2w_0^2}\Big\} \Omega_0(d), \tag{3.80}$$

and

$$\gamma_1 = \frac{(2\pi)^2}{\lambda f}\frac{w_1}{\pi w_0} \exp\Big\{-\frac{d^2}{2w_0^2}\Big\} \exp\{-i\varphi_0\} \Omega_1(d). \tag{3.81}$$

We show in Fig. 3.11 the behaviour of $|\gamma_0|^2$ and $|\gamma_1|^2$ as function of d/w_0 for three values of the beam waist w_1 of the projection mode. In Fig. 3.12 we see that the maximum values of $|\gamma_p|$ depend on the Gaussian projection mode waist w_1 and the azimuthal charge p; $|\gamma_0|^2$ is maximal for $w_1 = w_0'$ whereas $|\gamma_1|^2$ is for $w_1 = w_0'/\sqrt{2}$.

Solving the integral in Eq. (3.79) for $p = 1$, using Eq. (3.81) and $\Gamma(n) = (n-1)!$, one can see that

$$\gamma_1(d) = \frac{\pi\sqrt{2\pi}}{\lambda f} \frac{w_1}{\big[1 + (2\pi)^2 w_1^2 w_0^2/(\lambda f)^2\big]^{\frac{3}{2}}} d \exp\Big\{-\frac{d^2}{2w_0^2}\Big\} \exp\{-i\varphi_0\}. \tag{3.82}$$

Note that for the case $w_1 = w_0' = \lambda f/(2\pi w_0)$ we get

$$\gamma_1(d) = \frac{\sqrt{\pi}}{4w_0} d \exp\Big\{-\frac{d^2}{2w_0^2}\Big\} \exp\{-i\varphi_0\} \tag{3.83}$$

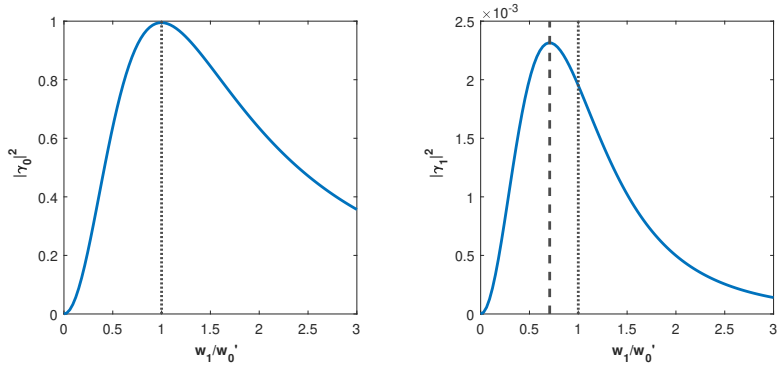

Figure 3.12: Coefficients $|\gamma_0|^2$ and $|\gamma_1|^2$ (normalized by $P_0|t_1|^2$) for a beam displacement $d/w_0 = 0.1$ as function of the waist of the Gaussian mode projection w_1. The power of the mode $p = 0$ is maximum at $w_1 = w_0'$ (dotted line), however the mode $p = 1$ has its maximum at $w_1 = w_0'/\sqrt{2}$ (dashed line).

which corresponds to the red curve in the right panel of Fig. 3.11. Note that although this value of the projection mode waist maximizes $|\gamma_0|^2$, there exist other values of w_1, in particular $w_1 < w_0'$ that reach higher values for $|\gamma_1|^2$. Furthermore, measuring the projection, with a given waist value w_1, one can determine the value of the displacement d of the Gaussian beam.

3.4.2 Localization in the transverse plane

To fully localize the optical beam by determining its position with respect to a reference axis it is necessary to determine both the distance to the axis and the direction of the displacement. We hereby propose a technique to estimate the displacement direction by extracting phase information from the $p-$mode projection.

We consider the same experimental configuration as before shown in Fig. 3.9. The beam interacts with the SLM at a given plane in which the coordinates transverse to the beam propagation are (r, φ). The SLM is divided in two zones, from $r = 0$ to $r = R$ we encode the digital blazed grating only, corresponding to a transfer function with $p = 0$ (see Eq. (3.41)) and a constant phase δ. From $r = R$ to $r = \infty$ we encode the phase $-ip\varphi$ together with the grating. The resulting holograms are included in figure 3.13. The coefficients γ_p from Eq. (3.78) are then modified due to the two regions of integration. Similarly, we define the measurable quantities

$$\gamma_0^R = \frac{(2\pi)^2}{\lambda f}\,\frac{w_1}{\sqrt{\pi}}\int_0^R r\,\mathrm{d}r\,a_0(r)\exp\Big[-\frac{1}{2}\Big(\frac{2\pi}{\lambda f}\Big)^2 w_1^2\,r^2\Big] \tag{3.84}$$

and

$$\gamma_p^R = \frac{(2\pi)^2}{\lambda f}\,\frac{w_1}{\sqrt{\pi}}\int_R^\infty r\,\mathrm{d}r\,a_p(r)\exp\Big[-\frac{1}{2}\Big(\frac{2\pi}{\lambda f}\Big)^2 w_1^2\,r^2\Big]. \tag{3.85}$$

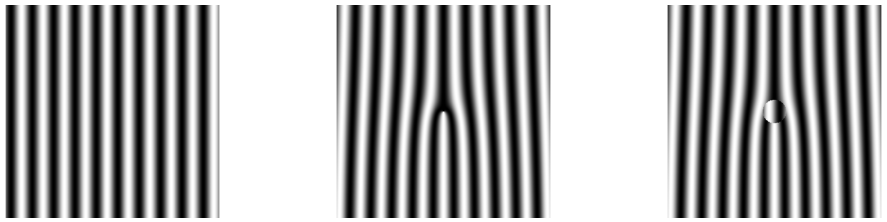

(a) Digital blazed grating *(b) $p = 1$* *(c) Resulting hologram*

Figure 3.13: Combination of holograms including the digital blazed grating (a), the azimuthal mode o (b) and the combination of both up to a certain radius R (c) for localization of the beam in the transverse plane.

The detected signal after projection to the Gaussian mode is $S_p(\delta)/P_0\,|t_1|^2$, explicitly

$$S_p(\delta) = |t_1|^2\,P_0\left|\exp(i\delta)\,\gamma_0^R(d) + \exp(-ip\varphi_0)\gamma_p^R(d)\right|^2. \tag{3.86}$$

Choosing the phases at the SLM to be $\delta \in \{0, \pi/2, \pi, 3\pi/2\}$, we can estimate the diplacement direction φ_0 as

$$\varphi_0 = \frac{1}{p}\tan^{-1}\frac{S(3\pi/2) - S(\pi/2)}{S(0) - S(\pi)}. \tag{3.87}$$

Furthermore, by selecting the value for R at which $|\gamma_0^R|$ matches $|\gamma_1^R|$, and varying the phase δ in the SLM, Eq. (3.86) for the mode $p = 1$ reduces to

$$S_1(\delta) = 2\,P_0\,|t_1|^2\,|\gamma_{0,1}^R|^2\left[1 + \cos(p\varphi_0 + \delta)\right], \tag{3.88}$$

which is maximum for $\delta = -p\varphi_0$ and has minima for $\mathrm{mod}(\delta + p\varphi_0, 2\pi) = \pi$.

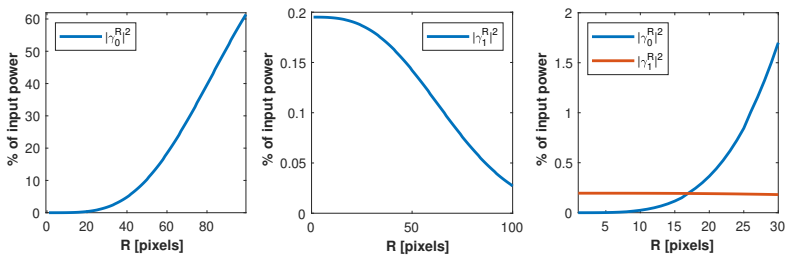

Figure 3.14: Measured signal as percentage of input power corresponding to the sections $\rho < R$ ($p = 0$) and $\rho > R$ ($p = 1$) as function of R in number pixels of the SLM (Hamamatsu X13138-07 with pixel size of 12.5μm). The probe is a Gaussian beam with waist $w_0 = 1$mm displaced a distance $d = 0.1w_0$. The power of each section shows similar values for $R \sim 17$ pixels$\sim 212.5\mu$m.

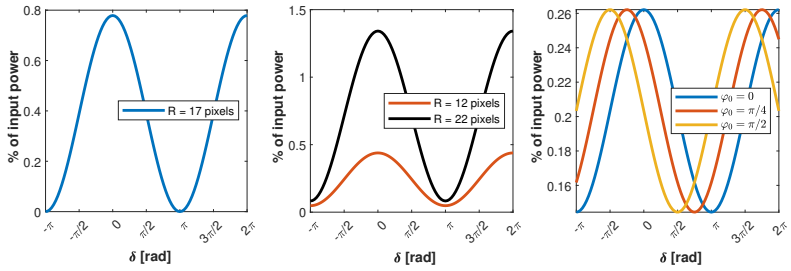

Figure 3.15: Detected signal $S_1(\delta)$ normalized by $|t_1|^2 P_0$ as percentage of the input power when varying the SLM phase δ. Left panel: Signal for $R = 17$ SLM pixels. Central panel: for $R \neq 17$ pixels the amplitudes of $\alpha_0^R(d)$ and $\alpha_1^R(d)$ unbalance and the amplitude of the oscillation changes, decreasing the visibility so the signal never vanishes. Right panel:Signal for different displacement directions φ_0, each curve has maxima in $\delta = \text{mod}\,(-p\varphi_0, 2\pi)$. All cases consider a displacement of $d = 0.1w_0$.

Hence, one can estimate the phase φ_0 associated to the direction of the beam displacement. Figure 3.14 shows the measurable quantities $|\gamma_0^R|^2$ and $|\gamma_1^R|^2$ that lead to the estimation of φ_0 when choosing R accordingly. Moreover, Figure 3.15 show the detected signals S_p when varying the SLM phase δ. The middle panel of figure 3.15 show that for values of R different to the optimal one in which $|\gamma_0^R| = |\gamma_1^R|$, when varying the phase δ the curve does not reach a zero if $\text{mod}(\delta + p\varphi_0, 2\pi) = \pi$. Figure 3.16 shows the visibility $(S_1^{max} - S_1^{min})/(S_1^{max} + S_1^{min})$ attained for different values of the beam displacement using different radius R.

3.4.3 Sensitivity and comparison with other methods

To evaluate the capabilities of this technique, we make use of the concepts introduced in Section 2.1 to describe the minimum error of the estimation of the beam displacement, and we compare with the standard technique using quadrant detectors.

Coherent multimode state of average number of photons N

Considering the displaced beam in Eq. (3.68) as a coherent beam

$$|\alpha_i\rangle = D(\alpha_i)|\text{vac}\rangle = \exp\left(\alpha_i \hat{a}_i^\dagger - \alpha_i^* \hat{a}_i\right)|\text{vac}\rangle, \tag{3.89}$$

where $D(\alpha_i)$ is the displacement operator and in the spatial domain we have

$$\alpha(x) = N^{1/2} \frac{1}{(\pi w_0^2)^{1/4}} \exp\Big[-\frac{(x-d)^2}{2w_0^2}\Big]. \tag{3.90}$$

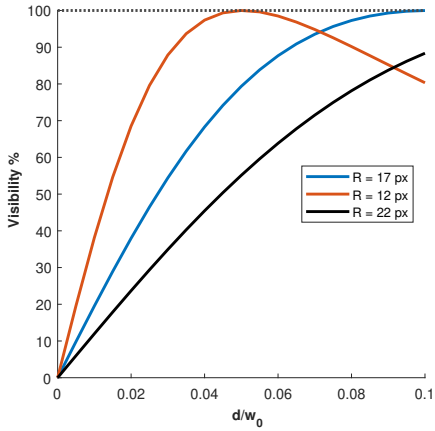

Figure 3.16: Signal visibility as function of the beam displacement d when projecting onto the mode $p = 0$ for $r < R$ and $p = 1$ for $r > R$, with $R = 17$ pixels.

In the transverse wavenumber domain we have

$$\begin{aligned}\alpha(q) &= N^{1/2}\,\frac{1}{\sqrt{2\pi}}\,\frac{1}{(\pi w_0^2)^{1/4}}\int \mathrm{d}x\,\exp\Big[-\frac{(x-d)^2}{2w_0^2}-iqx\Big]\\ &= \frac{N^{1/2}}{\sqrt{2\pi}}\,\frac{1}{(\pi w_0^2)^{1/4}}\sqrt{2\pi w_0^2}\exp\Big(-\frac{q^2w_0^2}{2}\Big)\exp\big(-iqd\big)\\ &= N^{1/2}\Big(\frac{w_0^2}{\pi}\Big)^{1/4}\exp\Big(-\frac{q^2w_0^2}{2}\Big)\exp\big(-iqd\big).\end{aligned} \tag{3.91}$$

The last term in the expression above relates the displacement d as a phase in the wavenumber space $\varphi(d) = -qd$. In this domain, the Quantum Fisher information associated to the estimation of the (phase) parameter d, for a multimode coherent state is

$$F_Q^{Coherent} = 4N\int \mathrm{d}q|\alpha(q)|^2\Big[\frac{\partial\varphi(q)}{\partial d}\Big]^2 \tag{3.92}$$

so we have

$$F_Q^{Coh} = 4N\Big(\frac{w_0^2}{\pi}\Big)^{1/2}\int \mathrm{d}q\,q^2\,\exp\Big(-q^2w_0^2\Big) = 4N\Big(\frac{w_0^2}{\pi}\Big)^{1/2}\frac{1}{2}\sqrt{\frac{\pi}{w_0^6}}\frac{2N}{w_0^2}. \tag{3.93}$$

The Cramer-Rao inequality $\sigma_d^2 \geq F_Q^{-1}$ implies

$$\sigma_d^{QCR} = \frac{w_0}{\sqrt{2N}}. \tag{3.94}$$

N copies of a single photon

On the other hand, if one considers the field in Eq. (3.68) corresponding to N copies of the single photon state

$$|\Psi\rangle = \int \mathrm{d}x\, U_0(x,d)\,|x\rangle = \int \mathrm{d}q\, \Psi(q,d)\,|q\rangle\,, \tag{3.95}$$

where $\Psi(q,d)$ is the Fourier transform of $U_0(x,d)$ so that the displacement d in the space domain becomes a phase in the spatial frequency domain. The Fisher Information per photon is

$$F_Q^{sp} = 4\int \mathrm{d}q|\Psi(q)|^2 \left(\frac{\partial\varphi}{\partial d}\right)^2 - 4\left[\int \mathrm{d}q|\Psi(q)|^2 \left(\frac{\partial\varphi}{\partial d}\right)\right]^2. \tag{3.96}$$

Since $\partial\varphi(d)/\partial d = -q$, the second term in the expression above vanishes due to the antisymmetric nature of the argument, then we get

$$F_Q^{sp} = 4\int \mathrm{d}q|\Psi(q)|^2 \left(\frac{\partial\varphi}{\partial d}\right)^2 = \frac{N}{2w_0^2}, \tag{3.97}$$

which is equal to the quantum Fisher Information in Eq. (3.93) corresponding to the coherent multimode case, therefore

$$\sigma_d^{QCR} = \sigma_d^{sp} = \sigma_d^{coh} = \frac{w_0}{\sqrt{2N}} \tag{3.98}$$

The Classical Crámer-Rao bound

Considering a direct measurement of the intensity of the light beam in Eq. (3.68), the detection probability distribution is

$$P(x|d) = \frac{1}{\sqrt{\pi w_0^2}} \int_{-\infty}^{\infty} \exp\Big\{-\frac{(x-d)^2}{w_0^2}\Big\}, \tag{3.99}$$

the Classical Fisher Information [129] is then given by

$$F_C(d) = -\int \mathrm{d}x P(x|d)\ \partial_d^2 \log P(x|d) = \frac{2N}{w_0^2}, \tag{3.100}$$

where the displacement is assumed to be along the x direction and N is the total number of detected photons of energy $\hbar\omega$ in the integration time T_d is $N = P_0 T_d/\hbar\omega$. The classical CR bound is

$$\sigma_d^{CCR} = \frac{w_0}{\sqrt{2N}}, \tag{3.101}$$

which is equal to the Quantum bound in Eq. (3.98) implying that the use of the intensity distribution of the Gaussian beam can provide an optimum measurement. Indeed it can be demonstrated [129] that the estimator

$$\hat{d} = \frac{1}{N}\sum_i x_i \tag{3.102}$$

is optimum for measuring the position of the Gausssian beam.

Projection onto $p-$modes

The signal (number of photons) detected after projecting onto the Gaussian beam of width w_1 the beam reflected (or transmitted) by the SLM is

$$N_d^p = |\gamma_p|^2 N \tag{3.103}$$

We can calculate

$$\frac{\partial N_d^p}{\partial d} = 2N|\gamma_p|\frac{\partial|\gamma_p|}{\partial d} \tag{3.104}$$

so that the variance σ_d^2 of the estimation of the distance d is

$$\sigma_d^2 = \frac{\langle(\Delta N_d^p)^2\rangle}{\left(\partial N_d^p/\partial d\right)^2} = \frac{1}{4N}\left(\frac{\partial|\gamma_p|}{\partial d}\right)^{-2}. \tag{3.105}$$

Here we have used $\langle(\Delta N_d)^2\rangle = N_d$, which is valid for coherent beams or long detection times. Therefore the error in the estimation of the distance d is

$$\sigma_d^p = \frac{1}{2\sqrt{N}}\left(\frac{\partial|\gamma_p|}{\partial d}\right)^{-1} \tag{3.106}$$

For $p = 1$, using Eq. (3.82) we have

$$\left(\frac{\partial|\gamma_1|}{\partial d}\right)^{-1} = \frac{\lambda f}{\pi\sqrt{2\pi}}\frac{1}{w_1}\left[1+\left(\frac{2\pi\, w_0}{\lambda f}\right)^2 w_1^2\right]^{\frac{3}{2}}\frac{w_0^2}{(w_0^2-d^2)}\,\exp\left\{\frac{d^2}{2w_0^2}\right\}. \tag{3.107}$$

Note that Eq. (3.107) has a minimum as function of w_1 for

$$w_1 = w_1' = \frac{1}{\sqrt{2}}\frac{\lambda f}{2\pi w_0} = \frac{w_0'}{\sqrt{2}}. \tag{3.108}$$

For this value of the projection Gaussian beam waist, the error is

$$\sigma_d^{SLM} = \frac{3}{2}\sqrt{\frac{3}{\pi}}\frac{w_0}{\sqrt{2N}}\frac{w_0^2}{(w_0^2-d^2)}\,\exp\left\{\frac{d^2}{2w_0^2}\right\}. \tag{3.109}$$

In the limit ($d \to 0$),

$$\sigma_d^{SLM}\Big|_{\min} = \frac{3}{2}\sqrt{\frac{3}{\pi}}\frac{w_0}{\sqrt{2N}} = 1.46,\ \ \frac{w_0}{\sqrt{2N}} = 1.46\ \sigma_d^{CR} \tag{3.110}$$

corresponding to a estimation efficiency ($\sigma_d^{CR}/\sigma_d^{SLM}$) of 68% [122]. We write Eq. (3.110) in this way for easier future comparison with the sensitivity that can be achieved with a quadrant detector.

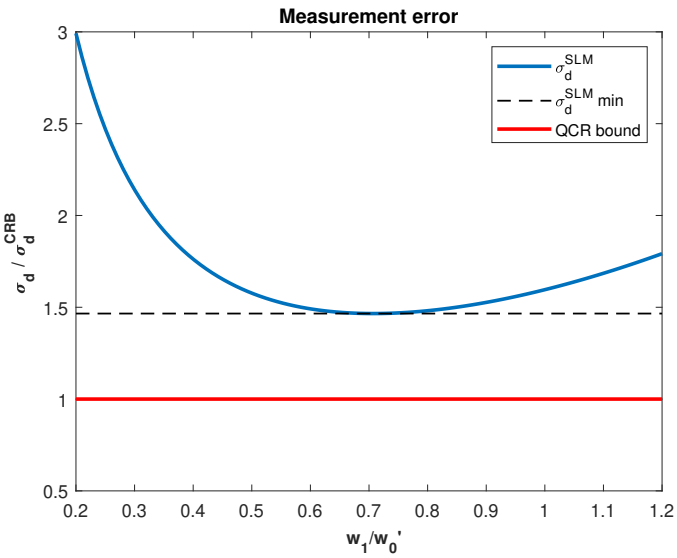

Figure 3.17: Error as function of the Gaussian beam projection waist w_1

Comparison with a quadrant detector

Let us compare this result with the sensitivity of a quadrant detector. The signal is

$$\begin{aligned} N_d^{quad} &= \frac{N}{\sqrt{\pi w_0^2}} \Big\{ \int_{-\infty}^{0} \mathrm{d}x \, \exp\Big[-\frac{(x-d)^2}{w_0^2} \Big] - \int_{0}^{\infty} \mathrm{d}x \, \exp\Big[-\frac{(x-d)^2}{w_0^2} \Big] \Big\} \\ &= \frac{N}{\sqrt{\pi w_0^2}} \Big| \Big\{ \int_{-\infty}^{-d} \mathrm{d}y \, \exp\Big[-\frac{y^2}{w_0^2} \Big] - \int_{-d}^{\infty} \mathrm{d}y \, \exp\Big[-\frac{y^2}{w_0^2} \Big] \Big\} \Big| \\ &= \frac{N}{\sqrt{\pi w_0^2}} \Big\{ \sqrt{\pi w_0^2} \, \mathrm{Erf}\Big(\frac{d}{w_0} \Big) \Big\} = N \, \mathrm{Erf}\Big(\frac{d}{w_0} \Big). \end{aligned} \tag{3.111}$$

The variance of the signal is

$$\langle (\Delta N_d)^2 \rangle = N \tag{3.112}$$

The derivative of the signal is

$$\frac{\partial N_d^{quad}}{\partial d} = \frac{2N}{\sqrt{\pi w_0^2}} \, \exp\Big(-\frac{d^2}{w_0^2} \Big) \tag{3.113}$$

The variance σ_d^2 of the estimation of the distance d is

$$\sigma_d^2 = \frac{1}{4N} \, \pi w_0^2 \, \exp\Big(\frac{2d^2}{w_0^2} \Big) \tag{3.114}$$

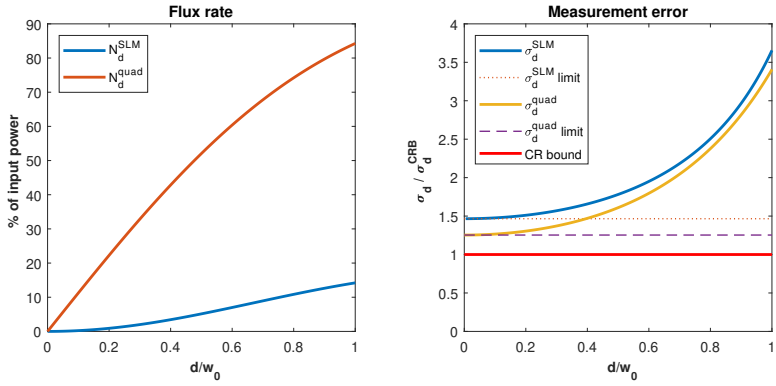

Figure 3.18: Flux rate as percentage of the input power (left) and measurement error (right) normalized by the quantum Crámer-Rao lower bound as function of the displacement d when projecting onto the $p = 1$ mode (blue) and when using a quadrant detector (yellow).

The error in the estimation of the distance d when using a quadrant detector is

$$\sigma_d^{quad} = \frac{1}{2\sqrt{N}} \sqrt{\pi w_0^2}\, \exp\Big(\frac{d}{w_0}\Big) \tag{3.115}$$

Note that when $d \to 0$ it corresponds to 80% efficiency [122]

$$\sigma_{d\to 0}^{quad} = \sqrt{\frac{\pi}{2}}\, \frac{w_0}{\sqrt{2N}} = 1.25\, \sigma_d^{CR} \tag{3.116}$$

Key expressions for comparison using a SLM and a quadrant detector

- The power measured:

$$N_d^{slm} = P_0\, |t_1|^2 |\gamma_1|^2 \tag{3.117}$$

$$N_d^{quad} = P_0\, \mathrm{Erf}\Big(\frac{d}{w_0}\Big) \tag{3.118}$$

- The errors associated to the two measurements:

$$\sigma_d^{slm} = \frac{1}{2\sqrt{N}}\, \frac{1}{|t_1|} \Big(\frac{\partial |\gamma_p|}{\partial d}\Big)^{-1} \tag{3.119}$$

$$\sigma_d^{quad} = \frac{1}{2\sqrt{N}} \sqrt{\pi w_0^2}\, \exp\Big[\Big(\frac{d}{w_0}\Big)^2\Big] \tag{3.120}$$

If we compare the expressions for $d \to 0$:

$$\sigma_d^{slm} = 1.46\, \frac{w_0}{\sqrt{2N}} \;>\; \sigma_d^{quad} = 1.25\, \frac{w_0}{\sqrt{2N}} \;>\; \sigma_d^{qcr} = \frac{w_0}{\sqrt{2N}}. \tag{3.121}$$

Chapter 4

Modal methods for optimum parameter estimation

Quantum estimation theory and its application to optical metrology have been very well known and studied for about fifty years [18]. However, in the past few years the interest re-emerged leading to evaluation of the maximum resolution achievable in diverse imaging systems [25, 130–132].

Through the quantum Crámer-Rao lower bound one can realistically determine the improvements in resolution when proposing novel techniques, as well as to quantify the obtained improvement. Given that the CR limit depends on the light-matter interaction and the quantum state of the illumination beam, it depends on the physical properties of the light; some classical properties such as spatial and temporal mode, wavelength, polarization, spatial shape, power; or some quantum-related properties such as degree of coherence, squeezing, entanglement, to name some. These properties influence the fundamental estimation precision limit and they can be exploited to obtain better resolution.

A measurement strategy that saturates the CR bound defines the ultimate resolution limit. Such a measurement strategy exists if the system fulfills certain conditions, then the measurement is referred to as *optimal* [21]. For an optimal measurement the quantum and classical CR bounds are equal and the ultimate resolution is attainable.

Modal measurements methods have shown to be efficient as strategy for parameter estimation [26, 63, 95]. The aim of this chapter is to present measuring strategies based on spatial modes of light and evaluate the set of modes that allow to perform an optimal measurement and achieve the ultimate resolution. We start by considering the problem of determining the distance between two point sources since it sets the basis for optical resolution. For a more general imaging scenario, we define the conditions for a modal measurement strategy to be optimal and we apply the results to an example relevant for the semiconductor industry, the estimation of the height and sidewall angle of cliff-like nanostructure.

4.1 Differential resolution: estimation of the separation between two point sources

Due to the progress in optical microscopy and the significant improvements in terms of resolution that modern techniques can achieve, it is relevant to investigate the fundamental limitations. Most of the so called super-resolution microscopy techniques that are able to surpass the diffraction limit ($\sim \lambda/2$) consist on intensity measurements in the far field that effectively locate optical point sources. This concept, sets the basics for the study of the resolution limitations of imaging systems. In this section we elaborate the fundamental concept of resolution in terms of the ability to estimate the distance between two point sources.

Although the Abbe-Rayleigh criterion has been the standard measure of resolution in many imaging scenarios, the formalism is found to be heuristic and not general enough [1, 3]. Instead, using the classical and quantum theory of electromagnetic fields, together the tools presented in Sections 2.1 and 2.2, it is possible to derive the fundamental limits for estimation of the distance between point sources. This defines a modern description of Rayleigh's criterion [32].

A thorough description of the problem from the perspective of quantum metrology allows to determine the fundamental quantum limit to the precision of locating two weak thermal sources. Surprisingly, this formalism shows that, for incoherent sources, the fundamental precision limit given by the quantum CR bound is inversely proportional to the number of photons. This result implies that Rayleigh's curse can be beaten, in contrast to what happens with coherent optical sources [25, 26].

4.1.1 Lower bounds for differential resolution

Following up Rayleigh's premises, consider two dim (incoherent) thermal source so that the number of photons arriving at the image plane for each short coherence time interval is smaller than 1. The quantum state in its density matrix representation can be written as

$$\rho = (1-\epsilon)\rho_0 + \epsilon\rho_1 + O(\epsilon^2). \tag{4.1}$$

ρ_0 and ρ_1 are the states with zero and one detected photons respectively. The zero photons state is just the Kronecker product of the vacuum with itself whereas the diffraction limited one-photon state can be written as

$$\rho_1 = \frac{1}{2}\left(|\Psi_+\rangle\langle\Psi_+| + |\Psi_-\rangle\langle\Psi_-|\right), \tag{4.2}$$

where Ψ_+ and Ψ_- are the states of the photons emitted by the sources located at $x_+ = d/2$ and $x_- = -d/2$, respectively. We neglect the $O(\epsilon^2)$ term since it is assumed to be considerably small. Since the sources are incoherent[1], if a photon

[1] In general, the spatial modes excited by two sources are not orthogonal $\int \Psi_1(x)\Psi_2^*(x)\mathrm{d}x \neq 0$, specially for sub-wavelength separated sources. For incoherent sources, we assume the orthogonality of the modes.

is detected, the probability distribution of the photon in the position x at the detector (image) plane is

$$f(x) = \frac{1}{2}\Big(|\Psi_+(x)|^2 + |\Psi_-(x)|^2\Big). \tag{4.3}$$

Note that $f(x)$ corresponds to intensity measurements at the image plane (direct imaging) and it is equivalent to the likehood function in Section 2.1. Assuming that the only parameter to be estimated is the separation ($\theta = d$) between the sources located at $x_+ = d/2$ and $x_- = -d/2$ respectively, to compute the quantum FI we make use of the point spread function (PSF) $\Psi(x)$ of the imaging system, so that $\Psi_s(x) = \Psi(x - x_s)$ is the spatial distribution in the image plane of the photon state emitted by the source s. At the image plane the state of the phton is given by

$$|\Psi\rangle = \int |x\rangle\langle x|\Psi\rangle \mathrm{d}x = \int \Psi(x)|x\rangle \mathrm{d}x. \tag{4.4}$$

Let us assume a Gaussian PSF of the form

$$\Psi(x) = \frac{1}{(2\pi\sigma^2)^{1/4}} \exp\left(-\frac{x^2}{4\sigma^2}\right), \tag{4.5}$$

where $\sigma = \lambda/2\pi NA$ is the width of the distribution and NA the numerical aperture of the optical system. The classical FI in Eq. (2.24) for a single parameter becomes

$$F_C(\theta) \quad = \quad N \int \frac{1}{f(x)} \Big[\frac{\partial f(x)}{\partial \theta}\Big]^2 \mathrm{d}x \tag{4.6}$$

Here $N = M\epsilon$ and M being the number of intervals in which the photons were detected. Explicitly, the intensity distribution in Eq. (4.3) considering the adequate normalization becomes

$$f(x) = \frac{1}{2}\frac{1}{\sqrt{2\pi\sigma^2}}\Big[\exp\left(-\frac{(x-d/2)^2}{2\sigma^2}\right) + \exp\left(-\frac{(x+d/2)^2}{2\sigma^2}\right)\Big] \tag{4.7}$$

Figure 4.1a shows that the classical Fisher information vanishes as the distance between the incoherent sources goes to zero. From the CR bound in Eq. (2.10) it follows that for direct imaging, as the distance decreases, the estimation is highly undetermined.

To find the quatum FI we make use of Eq. (2.50) and the spectral decomposition of the state (4.2) [26]. The quantum FI ends up being

$$F_Q = N\int_{-\infty}^{\infty} \Big(\frac{\partial \Psi(x)}{\partial x}\Big)^2 \mathrm{d}x = \frac{N}{\sqrt{2\pi\sigma^2}} \int_{-\infty}^{\infty} \frac{x^2}{4\sigma^4} \exp\big(-\frac{x^2}{2\sigma^2}\big) = \frac{N}{4\sigma^2}. \tag{4.8}$$

From Eq. (2.38) the CR lower bound for estimation of the distance between the incoherent sources is

$$C^S = \frac{1}{F_Q} = \frac{4\sigma^2}{N}. \tag{4.9}$$

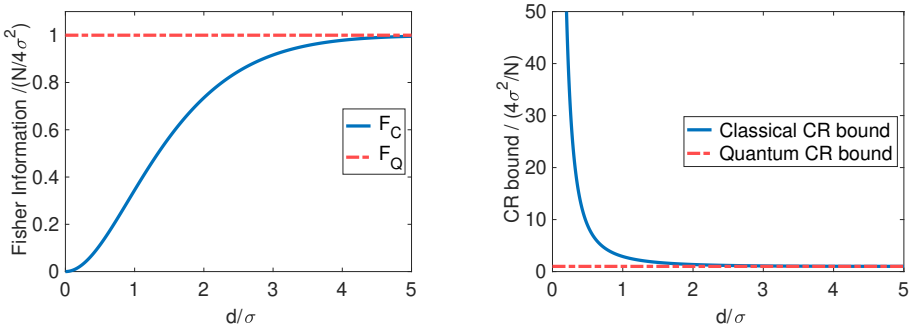

(a) Fisher Information *(b) CR bound*

Figure 4.1: Fisher Information and Crámer-Rao lower bound for the estimation of the distance between two incoherent point sources (differential resolution).

The great relevance of this result relies on the fact that the estimation precision bound is constant, independent of the distance between the sources, and it is inversely proportional to the number of photons used. This means that for an arbitrarily large number of photons and an unbiased estimator, one could asymptotically estimate the distance between two incoherent point sources with any desired precision using an optimal measurement strategy.

Although we are only considering the case of incoherent sources, in general the state of the photons at the image plane could be written in its density matrix representation as a sum of the coherent and the incoherent parts, namely

$$\hat{\rho} = (1-p)\hat{\rho}_i + p\hat{\rho}_c, \tag{4.10}$$

where p is a probability parameter related to the degree of coherence. In Ref. [133] it is shown that for any degree of coherence $p > 0$, Rayleigh's curse resurges.

4.1.2 Asymptotic attainability using spatial modes

Assuming a Gaussian PSF, the photon distribution of each incoherent point source in the image plane can be decomposed in Hermite-Gauss functions as [122]

$$\Psi(x) = \sum_{n=0}^{\infty} c_n(d) HG_n(x), \tag{4.11}$$

where $HG_n(x)$ is the Hermite-Gauss mode (see Section 3.1) of order n and the corresponding coefficients are given by:

$$c_n(d) = \int_{-\infty}^{\infty} \Psi(x) HG_n(x) \mathrm{d}x = \frac{d^n}{\sqrt{n!}} \frac{1}{(4\sigma)^n} \exp\left(-\frac{d^2}{32\sigma^2}\right). \tag{4.12}$$

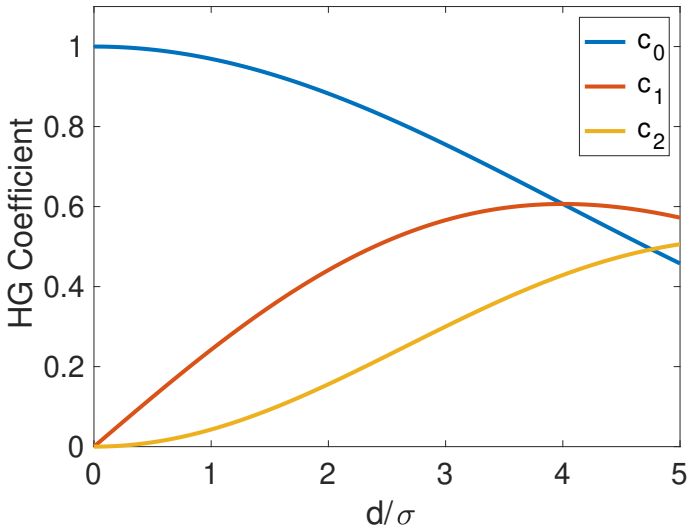

Figure 4.2: HG Coefficient dependence on the normalized distance d/σ

Figure (4.2) shows the dependence of the mode coefficients as function of the dimensionless variable d/σ, showing that for small values of d the most significant mode components are $n = 0, 1$. Let us assume that d/σ is small so it is valid to consider the infinite sum (4.11) up to m terms, as the high order coefficients become negligible. Consider the contribution of the first m modes; without losing generality, let us assume m to be an even number, the state is then approximated by

$$\Psi(x) \approx \sum_{n=0}^{m} c_n(d) HG_n(x). \tag{4.13}$$

Figure (4.3) shows the values of d/σ for which the approximation (4.13) holds for different values of m, this is, values of d/σ for which the state is still close to the normalization, namely

$$\sum_{n=0}^{m} |c_n(d)|^2 \approx 1. \tag{4.14}$$

The coefficients $c_n(d)$ in the expansion (4.11), given by expression (4.12) have the same parity than the index n with respect to the position inversion $d \to -d$. The states of each one of the sources is obtained by directly substituting expression

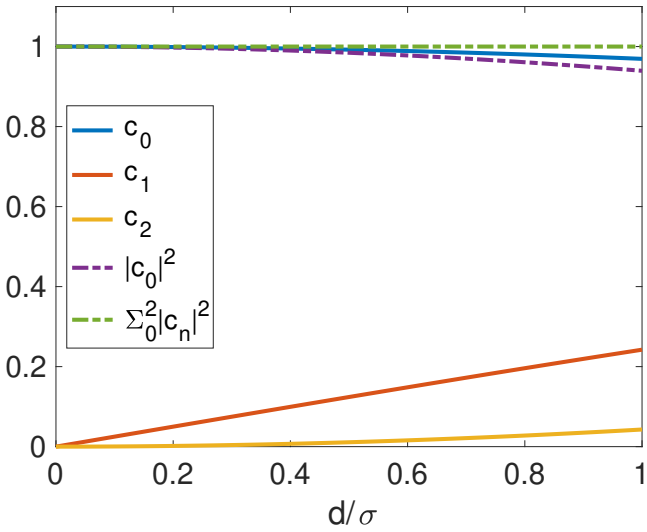

Figure 4.3: Verification of normalization condition validity. Solid lines correspond to the coefficients of the Hermite-Gauss decomposition and dashed lines correspond to the sum of the square coefficients, showing that for $d/\sigma < 1$ the decomposition up to the mode $n = 2$ is sufficient.

(4.13) in the state (4.4) and it is convenient to write them as:

$$|\Psi_+\rangle = \sum_{n=0}^{m/2} c_{2n}(d)\,|\Psi_{2n}\rangle + \sum_{n=0}^{m/2-1} c_{2n+1}\,|\psi_{2n+1}\rangle \tag{4.15}$$

and

$$|\Psi_-\rangle = \sum_{n=0}^{m/2} c_{2n}(d)\,|\psi_{2n}\rangle - \sum_{n=0}^{m/2-1} c_{2n+1}\,|\psi_{2n+1}\rangle\,, \tag{4.16}$$

where the basis vectors $\{|\psi_n\rangle\}$ are given by the Hermite-Gauss orthonormal functions

$$|\psi_n\rangle = \int HG_n(x)\,|x\rangle\,\mathrm{d}x, \tag{4.17}$$

and the coefficients $c_n(d)$ are given by equation (4.12). For small distance between the sources, it is sufficient to take a finite number of modes. As shown in figure 4.3, for $d < \sigma$ it is sufficient to consider the first three modes ($m = 2$). The state can be considered approximately normalized and it reduces to

$$\hat{\rho}_i = \frac{1}{2}\left[c_0^2\,|\psi_0\rangle\langle\psi_0| + c_0c_2\,|\psi_0\rangle\langle\psi_2| + c_1^2\,|\psi_1\rangle\langle\psi_1| + c_0c_2\,|\psi_2\rangle\langle\psi_0| + c_2^2\,|\psi_2\rangle\langle\psi_2|\right]. \tag{4.18}$$

which can be written in matrix form as:

$$\hat{\rho}_i = \frac{1}{2}\begin{bmatrix} c_0^2 & 0 & c_0c_2 \\ 0 & c_1^2 & 0 \\ c_0c_2 & 0 & c_2^2 \end{bmatrix}.$$

As introduced in Section 2.2, if the density matrix is non-singular, the FI can be obtained in a simple way if one expresses the density matrix in its spectral decomposition, this means, in terms of its eigenvectors as in equations (2.46) and (2.49). Performing the spectral decomposition one obtains:

$$\hat{\rho}_i = \sum_i P_i \left|\varphi_i\right\rangle \left\langle\varphi_i\right| = c_1^2 \left|\varphi_1\right\rangle \left\langle\varphi_1\right| + (c_0^2 + c_2^2) \left|\varphi_2\right\rangle \left\langle\varphi_2\right|, \tag{4.19}$$

where the eigenvalues are $P_0 = 0$, $P_1 = c_1^2$ and $P_2 = c_0^2 + c_2^2$, and the normalized eigenvectors are:

$$\left|\varphi_0\right\rangle = \frac{1}{\sqrt{c_0^2 + c_2^2}}[-c_2 \left|\psi_0\right\rangle + c_0 \left|\psi_2\right\rangle], \tag{4.20}$$

$$\left|\varphi_1\right\rangle = \left|\psi_1\right\rangle, \tag{4.21}$$

$$\left|\varphi_2\right\rangle = \frac{1}{\sqrt{c_0^2 + c_2^2}}[c_0 \left|\psi_0\right\rangle + c_2 \left|\psi_2\right\rangle]. \tag{4.22}$$

Using the spectral decomposition of the density matrix (4.19), the FI for the single parameter is given by equation (2.50). Explicitly, the derivative of the density matrix with respect to the parameter is

$$\Gamma = \frac{d\hat{\rho}}{d\theta} = \begin{bmatrix} 2c_0\frac{dc_0}{d\theta} & 0 & c_0\frac{dc_2}{d\theta} + c_2\frac{dc_0}{d\theta} \\ 0 & 2c_1\frac{dc_1}{d\theta} & 0 \\ c_0\frac{dc_2}{d\theta} + c_2\frac{dc_0}{d\theta} & 0 & 2c_2\frac{dc_2}{d\theta} \end{bmatrix} = \begin{bmatrix} \Gamma_0 & 0 & \Gamma_{02} \\ 0 & \Gamma_1 & 0 \\ \Gamma_{02} & 0 & \Gamma_2 \end{bmatrix}. \tag{4.23}$$

Substituting explicitly in (2.50), the FI is.

$$F_Q = \frac{\Gamma_1^2}{c_1^2} + \frac{\left(c_0^2\Gamma_0 + 2c_0\Gamma_{02}c_2 + c_2^2\Gamma_2\right)^2}{\left(c_0^2 + c_2^2\right)^3} + \frac{2\left(c_0^2\Gamma_{02} + c_0c_2(\Gamma_2 - \Gamma_0) - \Gamma_{02}c_2^2\right)^2}{\left(c_0^2 + c_2^2\right)^3} \tag{4.24}$$

Substituting explicitly the elements of the matrix Γ and taking the limit $d \to 0$ we see that $F_Q \to N/4\sigma^2$, equivalent to Eq. (4.8).

To measure the mode components of the field at the image plane, two methods are mainly used; Spatial-mode Demultiplexing (SPADE) and Superlocalization by Image Inversion Interferometry SILVER. SPADE consists of a selective measurement of the number of photons per mode of the field, which could be for instance expressed in terms of the Hermite-Gauss basis $\{|\psi_q\rangle\}$. In order to measure independently the number of photons per mode, the image plane field could be coupled to

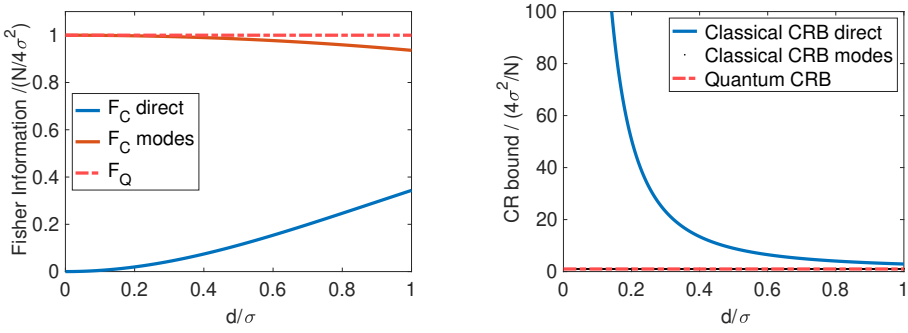

(a) Fisher Information *(b) CR bound*

Figure 4.4: Fisher Information and Crámer-Rao lower bound for differential resolution sensing with Hermite-Gauss spatial modes.

a multimode optical fiber, such that the longitudinal propagation constant of each mode is different. Each mode can be focused onto different spots along the optical axis by using a grating coupler and a lens [26], and thus measured independently.

SILVER insted, uses pixel arrays[2] in the two outputs of a Mach-Zehnder interferometer that separates the field in its symmetric and antisymmetric components with respect to spatial inversion.

Note that both techniques rely in the fact that the measurements can be performed in a projective manner through a POVM of the form $|\psi_n\rangle\langle\psi_n|$. As discussed in chapter 3, this is not a simple task.

Assuming the mode components are measured, the probability of detecting a photon in the $n-$th mode is

$$f_n = \frac{1}{2}\left(|\langle\psi_n|\Psi_+\rangle|^2 + |\langle\psi_n|\Psi_-\rangle|^2\right) = |c_n|^2. \tag{4.25}$$

The classical FI as in Eq. (4.6), usin explicitly Eqs.(4.15) and (4.16) is

$$F_C = \sum_{n=0}^{m} f_n \left(\frac{\partial}{\partial d}\ln f_n\right)^2 \simeq \frac{N}{4\sigma^2}, \tag{4.26}$$

which is equal to the Quantum FI in Eq. (4.8) and does not suffer from Rayleigh's curse. This means that if one employs a measuring strategy to detect the coefficients of the modal decomposition in the Hermite-Gauss basis, as the ones described above, one can determine the distance between two incoherent point sources with the maximum precision possible regardless the distance between them.

[2]For a given distance between the sources, the Fisher Information can be better approached by increasing the number of pixels in the array [27].

4.2 Optimal measurements based on modal methods

The interest of this section is to study measurement strategies based on modal methods that are optimal and allow to estimate the parameters of interest with ultimate resolution, this is, with the maximum estimation precision allowed by the quantum CR bound.

The state of the system $|\Psi_\theta\rangle$ can be expressed as a decomposition in an arbitrary set of orthonormal functions $\{|u_l\rangle\}$ with complex coefficients C_l that are functions of the n parameters of the system (see Section 3.3), namely

$$|\Psi_\theta\rangle = \sum_l C_l(\theta)\,|u_l\rangle\,. \tag{4.27}$$

In general both the amplitude and phase of the complex coefficients depend on the parameters of the system as $C_l(\theta) = A_l(\theta)\exp\{i\varphi_l(\theta)\}$. When projecting the state onto the mode $|u_l\rangle$, the probability of measuring the state in the l-th mode is A_l^2, thus the FIM in Eq. (2.24) is reduced to

$$[F_C]_{ik} = \sum_l \frac{1}{A_l^2}\partial_i A_l^2 \partial_k A_l^2 = 4\sum_l \partial_i A_l \partial_k A_l. \tag{4.28}$$

Additionally, since the state is considered to be pure, the QFIM from Eq. (2.37) is reduced to

$$\begin{aligned}[F_Q]_{ik} = 4\Big\{ &\sum_l \partial_i A_l \partial_k A_m - \sum_{l,m} A_l A_m \partial_k\varphi_l \partial_k \varphi_m \\ &+ \sum_l \Big[A_l^2 \partial_i\varphi_l\partial_k\varphi_l + i\big(\partial_i A_l \partial_k\varphi_l - \partial_k A_l \partial_i \varphi_l\big)\Big]\Big\}.\end{aligned} \tag{4.29}$$

Note that if the phases of each one of the coefficients of the decomposition are independent of the parameters ($\partial_j\varphi_l = 0,\ \forall\ \{j,l\}$) the classical FIM F_C is equal to the quantum FIM F_Q,

$$[F]_{ik} = [F_Q]_{ik} = 4\sum_l \partial_i A_l \partial_k A_l. \tag{4.30}$$

This result implies that if one can express the state as a sum of spatial modes with coefficients independent of the system's parameters (i.e. $C_l(\theta) = A_l(\theta)\exp\{i\varphi_l\}$, $\forall\, l$), sensing through a projective measurment onto those spatial modes is optimal, it allows to attain the fundamental precision bound. As relevant as this result is, finding such basis of modes is technically cumbersome and its experimental implementation is not always feasible.

Moreover, if it happens that for a given basis modes $\{u_i\}$ the information of the system's parameters is carried only by the phase of the coefficients of the modal decomposition in Eq. (4.27), (i.e. $C_l(\theta) = A_l\exp\{i\varphi_l(\theta)\},\ \forall\ l$) the optimality condition in Eq. (2.40) is satisfied; so that the Crámer-Rao bound associated to the QFIM is tight and attainable.

4.2.1 Tailoring an optimal mode decomposition

We consider the state of a single photon depending on n parameters $\theta = (\theta_1, ..., \theta_n)$ of the form

$$|\Psi_\theta\rangle = \int \mathrm{d}x\, \Psi(x,\theta)\, \hat{a}^\dagger(x)\, |\mathrm{vac}\rangle \tag{4.31}$$

where $\hat{a}^\dagger$ is the field operator of the mode of the illumination beam and $|\mathrm{vac}\rangle$ is the electromagnetic vacuum state, and $\Psi(x,\theta)$ is the spatial profile of the photon. Assume the conditions (2.39) and (2.41) are satisfied, so that the bound C^S is attainable. The state can be expanded around a point in the parameter space θ_0,

$$|\Psi_\theta\rangle \approx |\Psi_{\theta_0}\rangle + \sum_{i=1}^{n} \Delta_{\theta_i} |\partial_i \Psi\rangle. \tag{4.32}$$

Here $\Delta_{\theta_i} = \theta_i - \theta_{i_0}$ and $|\partial_i \Psi\rangle$ corresponds to the derivative with respect to the i-th element of the parameter vector θ_i evaluated in θ_0

$$|\partial_i \Psi\rangle = \int \mathrm{d}\mathbf{x}\, \frac{\partial \Psi(\mathbf{x},\theta)}{\partial_{\theta_i}}\Big|_{\theta_0} a^\dagger(\mathbf{x})\, |\mathrm{vac}\rangle. \tag{4.33}$$

Consider the set of modes $\{|\omega_i\rangle\}$ spanning the space orthogonal to Ψ_θ defined as $|\omega_i\rangle = |\partial_i \Psi\rangle + \langle \partial_i \Psi |\, \Psi_0\rangle\, |\Psi_0\rangle$ as defined in Eq. (4.33). To generate an orthonormal set of modes $\{|v_i\rangle\}$ we make use of the Gramm-Schmidt process. Using $|\omega_0\rangle = |\Psi_0\rangle$ and $|v_1\rangle = |\omega_1\rangle$, the vectors for $i > 1$ are given by:

$$|v_i\rangle = |\omega_i\rangle - \sum_{j=1}^{i-1} \frac{\langle v_j\, |\omega_i\rangle}{\langle v_j\, |v_j\rangle}\, |v_j\rangle\,. \tag{4.34}$$

We define the normalized vectors $|\gamma_i\rangle$ holding $|v_i\rangle = N_i\, |\gamma_i\rangle$, with $N_i^2 = \langle v_i\, |v_i\rangle$ such that $\langle \gamma_i |\, \gamma_j\rangle = \delta_{ij}$. From Eqs. (4.34) and (4.33) it follows that:

$$|\partial_i \Psi\rangle = N_i\, |\gamma_i\rangle - \langle \partial_i \Psi\, |\Psi_0\rangle\, |\Psi_0\rangle + \sum_{j=1}^{i-1} \langle \gamma_j |\omega_i\rangle |\gamma_j\rangle. \tag{4.35}$$

Using Eqs. (4.32) and (4.35) one can express $|\Psi_\theta\rangle$ as the decomposition in terms of the orthonormal set of spatial modes $\{|\gamma_i\}\rangle$:

$$|\Psi_\theta\rangle = \Gamma_0(\theta)\, |\Psi_0\rangle + \sum_{i=1}^{n} \Gamma_i(\theta)\, |\gamma_i\rangle\,. \tag{4.36}$$

At this point it is important to note the following: on the one hand, we note that from Eq. (4.36) the coefficients Γ_j directly depend on the parameters of interest; however, it is not direct that by measuring the coefficients one can estimate the parameters by comparing to the values obtained when solving the expressions in Eqs. (4.32) and (4.35). This is because a re-normalization of the state due to

the Taylor expansion in Eq. (4.32) is required. On the other hand, it is proven that a modal measurement based on projection onto the modes γ_j is optimal [21]. Note that an optical projection onto the modes $\{\gamma_i\}$ relies on the feasibility of the spatial mode realisation and the accuracy of the initial guess θ_0, which is not generally the case due to technical limitations of the equipment and the fact that a priori information about the sample is not always available. Assuming that it is indeed possible to perform the optical projection, the probabilities of detecting a photon in the mode $\gamma_i(x)$ are given by

$$P_i = |\langle \Psi_\theta | \gamma_i(\theta_0) \rangle|^2. \tag{4.37}$$

It is relevant to see that using full-field measuring techniques as Ptychography or interferometry, in which both the amplitude and the phase of the field are measured; the projections in Eq. (4.37) can be performed computationally, leading to optimal estimation of the parameters; either by comparing the value of the projection to the expected value given the refence parameter, or by varying the initial guess parameters θ_0 to maximize or minimize the projections.

Two parameter case

Considering a two-parameter estimation problem, this is, a state characterized by $\theta = (\theta_1, \theta_2)$. Using Taylor expansion in Eq. (4.32), the state can be written as

$$|\Psi_\theta\rangle \approx |\Psi_0\rangle + \Delta_{\theta_1} |\partial_1 \Psi\rangle + \Delta_{\theta_2} |\partial_2 \Psi\rangle . \tag{4.38}$$

The set of vectors $|\omega_k\rangle$ orthogonal to $|\Psi_0\rangle$ are

$$|\omega_1\rangle = |\partial_1 \Psi\rangle + \langle \partial_1 \Psi | \Psi_0 \rangle |\Psi_0\rangle \tag{4.39}$$

$$|\omega_2\rangle = |\partial_2 \Psi\rangle + \langle \partial_2 \Psi | \Psi_0 \rangle |\Psi_0\rangle . \tag{4.40}$$

Using the Gram-Schmidt orthogonalization process, we have:

$$|v_1\rangle = |\omega_1\rangle \tag{4.41}$$

$$|v_2\rangle = |\omega_2\rangle - \frac{\langle v_1 | \omega_2 \rangle}{\langle v_1 | v_1 \rangle} |v_1\rangle = |\omega_2\rangle - \frac{\langle \omega_1 | \omega_2 \rangle}{\langle \omega_1 | \omega_1 \rangle} |\omega_1\rangle . \tag{4.42}$$

Using the normalization constants, it follows that

$$N_1 |\gamma_1\rangle = |\partial_1 \Psi\rangle + \langle \partial_1 \Psi | \Psi_0 \rangle |\Psi_0\rangle \tag{4.43}$$

$$N_2 |\gamma_2\rangle = |\partial_2 \Psi\rangle + \langle \partial_2 \Psi | \Psi_0 \rangle |\Psi_0\rangle - \frac{\langle \omega_1 | \omega_2 \rangle}{N_1} |\gamma_1\rangle . \tag{4.44}$$

The normalization constants N_k are explicitly:

$$\begin{aligned} N_1^2 \quad &= \langle v_1 | v_1 \rangle = \langle \omega_1 | \omega_1 \rangle \\ &= \langle \partial_1 \Psi | \partial_1 \Psi \rangle + \langle \partial_1 \Psi | \Psi_0 \rangle^2 + \langle \Psi_0 | \partial_1 \Psi \rangle^2 + |\langle \Psi_0 | \partial_1 \Psi \rangle|^2 \end{aligned} \tag{4.45}$$

and

$$\begin{aligned} N_2^2 &= \langle v_2 \,|v_2\rangle = \Big[\, \langle \omega_2| - \frac{N_{12}^*}{N_1}\,\langle \omega_1| \,\Big]\Big[\, |\omega_2\rangle - \frac{N_{12}^*}{N_1}\,|\omega_1\rangle \,\Big] \\ &= \langle \omega_2 \,|\omega_2\rangle - \frac{N_{12}}{N_1^2}\langle \omega_2 \,|\omega_1\rangle - \frac{N_{12}^*}{N_1^2}\langle \omega_1 \,|\omega_2\rangle + \frac{|N_{12}|^2}{N_1^2} \\ &= \langle \omega_2 \,|\omega_2\rangle - \frac{|N_{12}|^2}{N_1^2}. \end{aligned} \tag{4.46}$$

Where

$$\langle \omega_2 \,|\omega_2\rangle = \langle \partial_2\Psi \,|\partial_2\Psi\rangle + \langle \partial_2\Psi \,|\Psi_0\rangle^2 + \langle \Psi_0 \,|\partial_2\Psi\rangle^2 + |\langle \Psi_0 \,|\partial_2\Psi\rangle\,|^2 \tag{4.47}$$

and $N_{12} = \langle \omega_1 \,|\omega_2\rangle$, explicitly

$$N_{12} = \langle \partial_1\Psi \,|\partial_2\Psi\rangle + 2\,\mathrm{Re}\{\langle \partial_1\Psi \,|\Psi_0\rangle\,\langle \partial_2\Psi \,|\Psi_0\rangle\} + \langle \Psi_0 \,|\partial_1\Psi\rangle\,\langle \partial_2\Psi \,|\Psi_0\rangle\,. \tag{4.48}$$

4.2.2 Example. Height and sidewall angle estimation of a cliff-like nanostructure

Consider a cliff-like nostructure of height h and sidewall angle α as shown in figure 2.5 in Section 2.4. Due to the fabrication process the sharpness of the structure suffers of rounding effects and lose of sharpness. The actual transverse section of the object's surface can be modeled by a differentiable function

$$f(x) = \frac{h}{2}(1 + \tanh \alpha x). \tag{4.49}$$

The center of the slope is assumed to be at $x = 0$ and the side wall angle β is such that $f'(x)_{|_{x=0}} = \tan\beta$, and $\alpha = 2/b$. We consider the estimation of the parameters $\theta_1 = \alpha$ and $\theta_2 = h$. Assuming that the object is probed with a Gaussian beam of width $w_0 = \lambda/\pi NA$ consisting of M independent photons. λ is the wavelength of the illumination and NA the effective numerical aperture of the optical system. The state of the photons is $|\Psi_0\rangle$ with $\Psi_0(x) = \big(2/\pi w_0^2\big)^{1/4}\exp\big\{-x^2/w_0^2\big\}$ the Gaussian distribution. The phase added to the probe after the interaction with the object is $\varphi(x;\theta) = kh(1 - \tanh\alpha x)$, so that the state of a scattered photon from Eq. (4.31), has spatial distribution

$$\Psi(x;\theta) = \Psi_0(x)\exp\big\{ikh\big(1 - \tanh\alpha x\big)\big\}. \tag{4.50}$$

The derivatives in Eq. (4.33) with respect to $\theta_1 = h$ and $\theta_2 = \alpha$ are explicitly

$$|\partial_1\Psi\rangle = |\partial_h\Psi\rangle = ik\int \Psi(x;\theta_0)\,(1 - \tanh\alpha_0 x)\,|x\rangle\,\mathrm{d}x. \tag{4.51}$$

$$|\partial_2\Psi\rangle = |\partial_\alpha\Psi\rangle = -ikh_0\int \Psi(x;\theta_0)\,x\,\operatorname{sech}^2\alpha_0\,x\;\,|x\rangle\,\mathrm{d}x. \tag{4.52}$$

The corresponding inner products are

$$\langle \Psi_0 | \, \partial_h \Psi \rangle = ikN_0^2 \int_{-\infty}^{\infty} (1 - \tanh \alpha_0 x) e^{-\frac{2x^2}{\omega_0^2}} \, \mathrm{d}x = ik, \tag{4.53}$$

$$\langle \Psi_0 | \, \partial_\alpha \Psi \rangle = -ikh_0 N_0^2 \int_{-\infty}^{\infty} x \mathrm{sech}^2 \alpha_0 x \, e^{-\frac{2x^2}{\omega_0^2}} \, \mathrm{d}x = 0, \tag{4.54}$$

$$\begin{aligned} \langle \partial_h \Psi | \, \partial_h \Psi \rangle &= N_0^2 k^2 \int_{-\infty}^{\infty} \left(1 + \tanh^2 \alpha_0 x\right) e^{\frac{2x^2}{\omega_0^2}} \, \mathrm{d}x \\ &= 2k^2 - N_0^2 k^2 \frac{2}{\alpha_0} = 2k^2 - \left(\frac{2}{\pi}\right)^{1/2} \frac{2k^2}{\alpha_0 w_0} \sim 2k^2, \end{aligned} \tag{4.55}$$

$$\begin{aligned} \langle \partial_\alpha \Psi | \, \partial_\alpha \Psi \rangle &= N_0^2 k^2 h_0^2 \int_{-\infty}^{\infty} x^2 \mathrm{sech}^4 \alpha_0 x e^{-\frac{2x^2}{\omega_0^2}} \, \mathrm{d}x \\ &= N_0^2 k^2 h_0^2 \frac{\pi^2 - 6}{9\alpha_0^3}, \end{aligned} \tag{4.56}$$

$$\begin{aligned} \langle \partial_h \Psi | \, \partial_\alpha \Psi \rangle &= N_0^2 k^2 h_0 \int_{-\infty}^{\infty} x \mathrm{sech}^2 \alpha_0 x \tanh \alpha_0 x \, e^{\frac{2x^2}{\omega_0^2}} \, \mathrm{d}x \\ &= \frac{N_0^2 k^2 h_0}{\alpha_0^2}, \end{aligned} \tag{4.57}$$

where $N_0 = \left(2/\pi w_0^2\right)^{1/4}$ such that the normalization condition $\langle \Psi \, | \Psi \rangle = 1$ holds and we make use of the conditions $w_0 \alpha_0 \gg 1$, which is in most experiments the relevant case. In equation (4.56) the relation $\tanh^2\theta + \mathrm{sech}^2\theta = 1$ and the following integrals have ben used

$$\int_{-\infty}^{\infty} \tanh \alpha_0 x \, e^{-\frac{2x^2}{\omega_0^2}} \, \mathrm{d}x = 0 \tag{4.58}$$

and

$$\int_{-\infty}^{\infty} \mathrm{sech}^2 \alpha_0 x \, e^{-\frac{2x^2}{\omega_0^2}} \, \mathrm{d}x \simeq \int_{-\infty}^{\infty} \mathrm{sech}^2 \alpha_0 x \mathrm{d}x = \frac{2}{\alpha_0}. \tag{4.59}$$

Similarly, in equation (4.57) we have used

$$\int_{-\infty}^{\infty} x \, \mathrm{sech}^2 \alpha_0 x \, e^{-\frac{2x^2}{\omega_0^2}} \, \mathrm{d}x = 0. \tag{4.60}$$

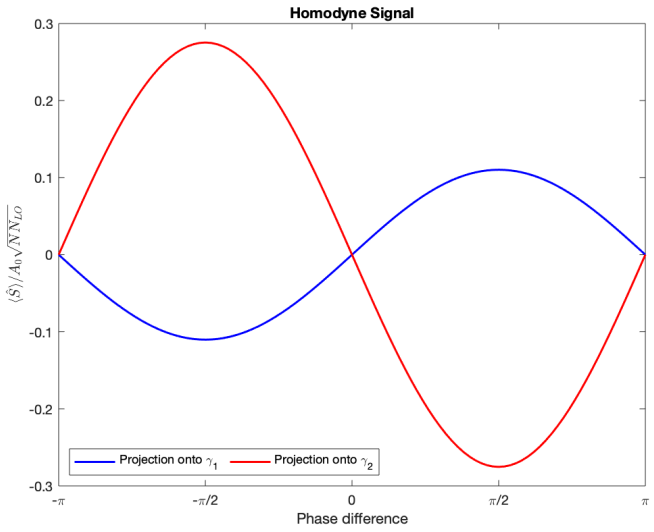

Figure 4.5: Homodyne differential signal as a function of the phase difference for the two-parameter estimation of the spatial features of a cliff-like nanostructure. The local oscillator holds the spatial mode $\gamma_1 = \gamma_\alpha$ (blue curve) or $\gamma_2 = \gamma_h$ (red curve). The projection state parameters are $\beta_0 = 85°$, $h_0 = 150nm$ and the true state parameters differ from the true parameter by 10%, $\Delta\theta_i = \theta_i/10$. The signal is normalized by the single photon intensity is $A_0 = \frac{\hbar\omega}{\varepsilon_0 cT}$. N, N_{LO} are the number of photons of the probe and LO beam, respectively detected within the integration time T of the photodetector.

Substituting these inner products explicitly in Eqs.(4.45) to (4.48) one gets

$$N_{h\alpha} = \langle \partial_1 \Psi | \partial_2 \Psi \rangle = N_0^2 \frac{k^2 h_0}{\alpha_0^2}, \tag{4.61}$$

$$N_h = k \left[1 - \left(\frac{2}{\pi} \right)^{1/2} \frac{2}{\alpha_0 w_0} \right]^{1/2} \sim k, \tag{4.62}$$

$$N_\alpha = \frac{N_0 k h_0}{3\alpha_0^{3/2}} \left[\pi^2 - 6 - \left(\frac{2}{\pi} \right)^{\frac{1}{2}} \frac{9}{\alpha_0 w_0} \right]^{1/2} \sim \frac{N_0 k h_0}{3} \sqrt{\frac{\pi^2 - 6}{\alpha_0^3}}, \tag{4.63}$$

where it has been used that $\langle \omega_2 | \omega_2 \rangle = \langle \Psi_2 | \Psi_2 \rangle$, since $\langle \Psi_2 | \Psi_0 \rangle = 0$ and the experimentally relevant condition $w_0 \alpha_0 \gg 1$ has been taken into account. The projection states $|\gamma_1\rangle$ and $|\gamma_2\rangle$ from Eqs. (4.43) and (4.44) are

$$|\gamma_1\rangle = \frac{1}{N_h} |\omega_1\rangle = \frac{1}{N_h} \left[|\partial_1 \Psi\rangle + \langle \partial_1 \Psi | \Psi_0 \rangle |\Psi_0\rangle \right] \tag{4.64}$$

$$|\gamma_2\rangle = \frac{1}{N_\alpha} \left[|\partial_2 \Psi\rangle + N_{20} |\Psi_0\rangle - \frac{N_{h\alpha}}{N_h} |\gamma_1\rangle \right]. \tag{4.65}$$

Substituting explicitly the inner products, the modes are

$$|\gamma_1\rangle = -i \int \Psi(x;\theta_0) \tanh \alpha_0 x \; |x\rangle \; \mathrm{d}x \tag{4.66}$$

$$|\gamma_2\rangle = \frac{3}{N_0 k h_0} \sqrt{\frac{\alpha_0^3}{\pi^2 - 6}} \int \Psi(x,\theta_0) \left[\frac{N_0^2 h_0^2}{\alpha_0^2} \tanh \alpha_0 x - i k h_0 \, x \, \mathrm{sech}^2 \alpha_0 x \right] |x\rangle \; \mathrm{d}x. \tag{4.67}$$

Measuring the state in this basis is known to satisfy $F = F_Q$, leading to the optimal estimation of α and h. This can be done by means of optical projection using the homodyne spatial mode analyzer introduced in the previous section. Since the coefficients are real, the homodyne detection signal from Eq. (3.38) when combining the scattered beam with each one of the modes γ_l is directly proportional to Γ_l modulated by the sine of the phase difference. Namely, when varying the phase of the local oscillator, the amplitude of the measured signal is maximal and proportional to the coefficient Γ_l when the phase difference is $\pi/2$, and zero when it is multiple of π. These result is plotted in in Figure 4.5 for the cases in which the local oscillator holds the mode γ_1 (blue curve) and γ_2 (red curve).

Comparison with one-dimensional models

If one is interested exclusively in the estimation of either the height or the side wall angle, the problem is reduced to a single parameter estimation. In each case, the optimal mode is given by Eq. (4.39) and the derivative vectors (4.51) and (4.52). For the estimation of the height ($\theta = h$), assuming $\alpha = \alpha_0$, one has

$$|\gamma_h\rangle = ik \int \mathrm{d}x \Psi_0(x) \Big[1 - \tanh(\alpha_0 x) \Big] |x\rangle. \tag{4.68}$$

Where $\Psi_0(x) = \Psi(x,\theta_0) = \Psi(x,h_0)$, with $\Psi(x)$ as in Eq. (4.50). Projecting the state of the probing light wave (either optically of computationally after full-field measurements) as in Eq. (4.37) one gets

$$\begin{aligned} \langle \gamma_h | \Psi \rangle &= i \int \mathrm{d}x |\Psi_0(x)|^2 \tanh(\alpha_0 x) \exp(i\varphi - i\varphi_0) \\ &= i \int \mathrm{d}x |\Psi_0(x)|^2 \tanh(\alpha_0 x) \exp\Big[ik\Delta h (1 - \tanh(\alpha_0 x) \Big] \end{aligned} \tag{4.69}$$

where $\Delta h = h - h_0$. If we expand this expression to second order in Δh, we obtain

$$\langle \gamma_h | \Psi \rangle = k\Delta h + i \, (k\Delta h)^2. \tag{4.70}$$

Here we have made use of the Taylor expansion of the exponential term in Eq. 4.69) and the fact that $\int \mathrm{d}x |\Psi(x,h_0)|^2 \tanh^2(\alpha_0 x) \sim 1$ when $\sigma\alpha_0 \gg 1$. Finally,

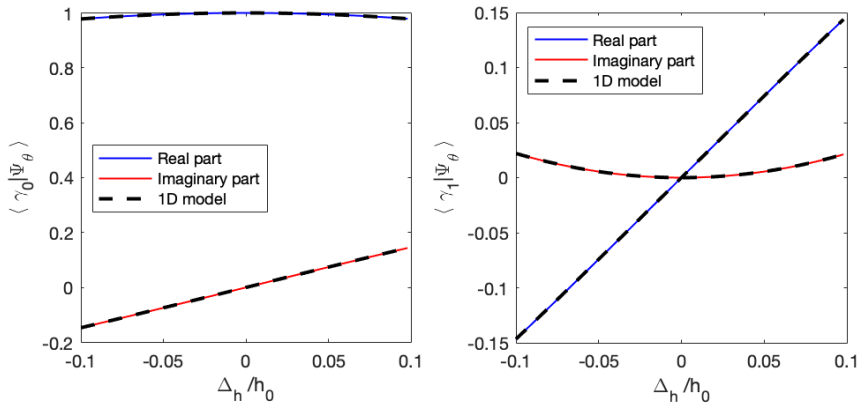

Figure 4.6: Two parameter estimation model comparison with respect to the one dimensional case. Real and imaginary parts of the projections $\langle \gamma_0 | \Psi_h \rangle$ (left) and $\langle \gamma_1 | \Psi_h \rangle$ (right) as function of the normalized error $\delta_h = \Delta_h / h_0$ for $h_0 = 150$ nm and α_0 corresponding to a sidewall angle $\beta_0 = 89°$; considering $\Delta\alpha = 0$. Dashed line corresponds to the one dimensional model.

we can write the mode projection as

$$\langle \gamma_h | \Psi \rangle = k h_0 \frac{\Delta h}{h_0} + i\,(k h_0)^2 \Big(\frac{\Delta h}{h_0}\Big)^2. \tag{4.71}$$

Moreover, projecting on to the initial guess state Ψ_0, one gets

$$\langle \gamma_0 | \Psi \rangle = \int \mathrm{d}x |\Psi_0(x)|^2 \, \exp\Big\{ ik\Delta h \Big[1 - \tanh(\alpha_0 x)\Big]\Big\} \tag{4.72}$$

Once again, we expand this expression bow to second order in Δh:

$$\langle \gamma_0 | \Psi \rangle = \int \mathrm{d}x |\Psi_0(x)|^2 \Big\{ 1 + ik\Delta h \Big[1 - \tanh(\alpha_0 x)\Big] - \frac{(k\Delta h)^2}{2} \Big[1 - \tanh(\alpha_0 x)\Big]^2 \Big\} \tag{4.73}$$

If we use again the relative thickness variation $\Delta h / h_0$, we can write

$$\langle \gamma_0 | \Psi \rangle = 1 - (k h_0)^2 \Big(\frac{\Delta h}{h_0}\Big)^2 + ik h_0 \frac{\Delta h}{h_0} \tag{4.74}$$

Summarizing, the mode projections of interest are

$$\langle \gamma_0 | \Psi \rangle = 1 - (k h_0)^2 \Big(\frac{\Delta h}{h_0}\Big)^2 + ik h_0 \frac{\Delta h}{h_0} \tag{4.75}$$

and

$$\langle \gamma_h | \Psi \rangle = k h_0 \frac{\Delta h}{h_0} + i\,(k h_0)^2 \Big(\frac{\Delta h}{h_0}\Big)^2. \tag{4.76}$$

Note that the equations above coincide with the two-dimensional case when taking $\Delta_\alpha = 0$. This result is shown in Figure 4.6. Thus, from the detection probabilities in Eq. (4.37), to second order in Δh it follows that

$$P_0 + P_1 = 1 - 2(kh_0)^2\Big(\frac{\Delta h}{h_0}\Big)^2 + (kh_0)^2\Big(\frac{\Delta h}{h_0}\Big)^2 + (kh_0)^2\Big(\frac{\Delta h}{h_0}\Big)^2 = 1. \tag{4.77}$$

If one considers now the single-parameter estimation problem for the determination of the sidewall angle ($\theta = \alpha$), assuming $h = h_0$), we have

$$|\gamma_\alpha\rangle = -kh_0\,\frac{i}{N^{1/2}}\int \mathrm{d}x\,\Psi_0(x)x\,\operatorname{sech}^2(\alpha_0 x)\,|x\rangle \tag{4.78}$$

where

$$N = (kh_0)^2\int \mathrm{d}x|\Psi_0(x)|^2x^2\,\operatorname{sech}^4(\alpha_0 x) = (kh_0)^2\,\frac{1}{\alpha_0^3}\,\Big(\frac{2}{\pi\sigma^2}\Big)^{1/2}\,\frac{\pi^2-6}{9}. \tag{4.79}$$

We want to estimate small deviations from α_0, i.e., $\alpha = \alpha_0 + \Delta\alpha$. Using the approximation to second order in $\Delta\alpha$

$$\begin{aligned}
\langle\gamma_0\,|\Psi\rangle &= \int \mathrm{d}x\,|\Psi(x)|^2\,\exp\Big\{i\varphi(x,\alpha) - i\varphi(x,\alpha_0)\Big\}\\
&= \int \mathrm{d}x\,|f(x)|^2\,\exp\Big\{ikh_0\,[\tanh(\alpha_0 x) - \tanh(\alpha x)]\,\Big\}\\
&= \int \mathrm{d}x\,|f(x)|^2\,\exp\Big\{-i\Delta\alpha\,kh_0\,x\operatorname{sech}^2(\alpha_0 x)\\
&\qquad\qquad - i\frac{(\Delta\alpha)^2}{2}\,kh_0\,x^2\tanh(\alpha_0 x)\operatorname{sech}^2(\alpha_0 x)\Big\}.
\end{aligned} \tag{4.80}$$

Using $A = -kh_0 x\operatorname{sech}^2\alpha_0 x$ and $B = kh_0\,x^2\tanh\alpha_0 x\,\operatorname{sech}(\alpha_0 x)$, the Taylor expansion for the exponential term is

$$\exp\Big[iA\Delta\alpha + i\frac{B}{2}(\Delta\alpha)^2\Big] = \Big[1 - \frac{1}{2}\,A^2(\Delta\alpha)^2\Big] + i\Big[A\Delta\alpha + \frac{B}{2}(\Delta\alpha)^2\Big] \tag{4.81}$$

we obtain

$$\langle\gamma_0|\Psi\rangle = 1 - \frac{1}{2}N\,(\Delta\alpha)^2 \tag{4.82}$$

and

$$\langle\gamma_\alpha|\Psi\rangle = N^{1/2}\,\Delta\alpha - \frac{(kh_0)^2}{N^{1/2}}\frac{(\Delta\alpha)^2}{2}\int \mathrm{d}x|\Psi_0(x)|^2x^3\,\operatorname{sech}^4(\alpha_0 x)\,\tanh(\alpha_0 x) \tag{4.83}$$

To first order in $\Delta\alpha$ we have

$$\langle\gamma_\alpha|\Psi\rangle = N^{1/2}\Delta\alpha = \left(\frac{2}{\pi}\right)^{1/4}\,\Big(\frac{\pi^2-6}{9}\Big)^{1/2}\,\frac{kh_0}{\sqrt{\sigma\alpha_0}}\frac{\Delta\alpha}{\alpha_0} \tag{4.84}$$

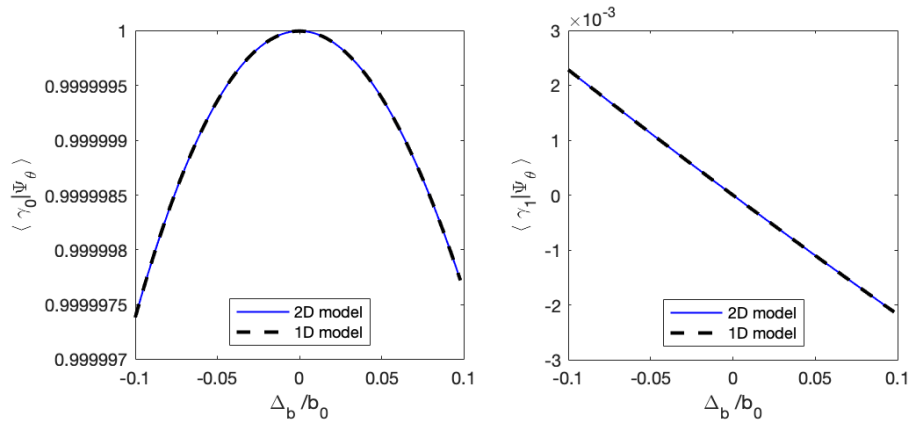

Figure 4.7: Two parameter estimation model comparison with respect to the one dimensional case. Values of the projection $\langle \gamma_0 | \Psi_\alpha \rangle$ (left) and $\langle \gamma_1 | \Psi_\alpha \rangle$ (right) as function of the normalized error $\delta_b = \Delta_b / b_0$, with $b = 2/\alpha$, the horizontal projection of the slope with $h_0 = 150$ nm and α_0 corresponding to a sidewall angle $\beta_0 = 89°$; considering $\Delta_h = 0$. Dashed line corresponds to the one dimensional model.

Similar as in Eq. (4.77), up to second order in $\Delta\alpha$:

$$P_0 + P_1 = 1 - N\,(\Delta\alpha)^2 + N\,(\Delta\alpha)^2 = 1. \tag{4.85}$$

Note that the equations above coincide with the two-dimensional case when taking $\Delta_h = 0$. This result is shown in Figure 4.7.

The extension of the results to the two-parameter estimation problem are shown in Figures 4.8-4.10. It is relevant to point out that the selection of the order of the parameters (θ_1, θ_2) is in general arbitrary and can be chosen according to convenience of the computation of Eqs. (4.43) and (4.44) together with the inner products in Eqs. (4.45) - (4.48). For instance, inverting the order of the parameters, $\theta_1 = \alpha$ and $\theta_2 = h$; using the expressions in Eq. (4.39) and (4.40), together with the inner products 4.53) - (4.57), one gets

$$N_\alpha \,|\gamma_1\rangle = |\partial_\alpha \Psi\rangle = -ikh_0 \int \Psi(x, \theta_0)\, x \,\mathrm{sech}^2\, \alpha_0 x \,|x\rangle \,\mathrm{d}x, \tag{4.86}$$

and

$$\begin{aligned} N_h \,|\gamma_2\rangle &= |\partial_h \Psi\rangle + ik\,|\Psi_0\rangle - \frac{N_0^2 k^2 h_0}{N_1^2 \alpha_0^2}\,|\partial_\alpha \Psi\rangle \\ &= ik \int \Psi(x; \theta_0) \left[\frac{N_{\alpha h}}{N_\alpha^2} h_0\, x \,\mathrm{sech}^2\, \alpha_0 x - \tanh \alpha_0 x \right] |x\rangle \,\mathrm{d}x. \end{aligned} \tag{4.87}$$

Although the modes γ_1 and γ_2 are different, the obtained results are equivalent and the behaviour observed in figures 4.8-4.10 holds for the inversion of the order of parameters.

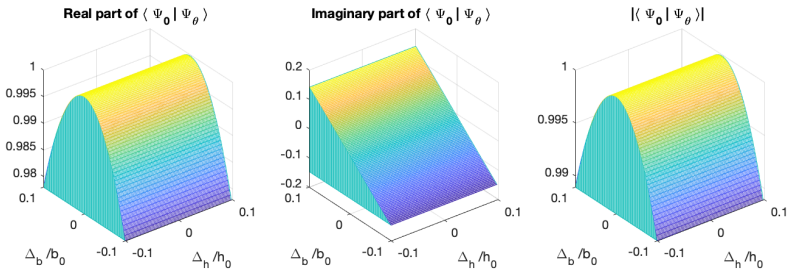

Figure 4.8: Projection to $|\Psi_0\rangle$

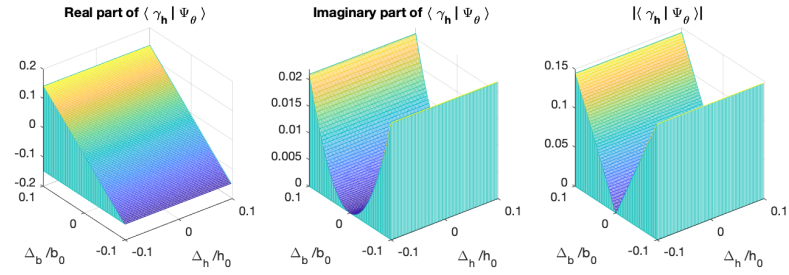

Figure 4.9: Projection to $|\gamma_1\rangle$

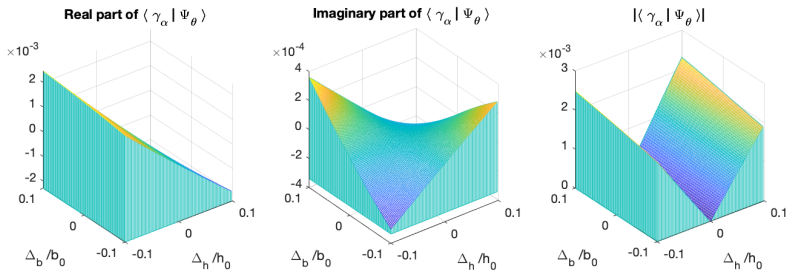

Figure 4.10: Projection to $|\gamma_2\rangle$

Chapter 5

Computational methods for resolution-enhanced sensing

In the core of this thesis, it is of interest to explore measuring protocols to measure spatial features of objects by extracting relevant information beyond the spatial resolution limit given by diffraction. In the previous chapters we have explored the advantages of sensing with spatial modes of light and retrieving information carried by the phase of the optical beam. However, a different approach can be taken. Exploiting the considerable computational advances in terms of both software and hardware, modern computational methods allow to rigorously solve scattering and diffraction problems with extremely high accuracy. Moreover, it is possible to take further advantage of the advances in computational methods. Namely, the development of artificial intelligence (AI) algorithms, specifically Machine Learning (ML) and Neural Networks (NN), allow the access to otherwise apparently hidden information by recognizing patterns from data sets. The content of this chapter has been published in a peer reviewed journal as a research article (Ref. [134]) of which the author of this dissertation is first author.

When using ML algorithms for imaging purposes, NN are able to classify images, recognize specific features of interest and categorize them. In this chapter, we put forward and demonstrate with model particles a *smart* laser-diffraction analysis technique aimed at particle mixture identification. In contrast to commonly-used laser diffraction schemes—in which a large number of detectors are needed—our ML-assisted protocol makes use of a single far-field diffraction pattern contained within a small angle ($\sim 0.26°$) around the light propagation axis. It retrieves all information from the diffraction pattern generated by the whole array of particles, which simplifies considerably its implementation in comparison with alternative schemes. The method does not make use of any physical model of scattering to help in the particle characterization, which usually adds computational complexity to the identification process.

5.1 Laser Diffraction analysis for optical metrology

Particle characterization techniques have long played a fundamental role in many different branches of science and technology. In biology, they assist in schemes for the detection of bacteria [135] and viruses [136]. They are important in the pharmaceutical [137,138], food processing [139,140], and the semiconductor industries [141]. Particularly important are applications aimed at environmental monitoring and protection [142,143]. Some potential applications include the detection of microplastics in marine waters [144], and the characterization of airborne particles, given that their size is strongly correlated with pulmonary toxicity [145,146] leading to respiratory illnesses.

Remarkably, more than 75% of all materials processed in the industry are in particulate form. These particles may be contained in substances in any of the three known phases (solid, liquid, or gaseous) and can be divided into three broad groups: natural, industrially processed from natural products, and completely synthetic particles [147]. In general, one can identify two important reasons for industries routinely employing particle characterization [148]: better understanding of products and processes, and better control of product quality. While the former allows for the optimization of the manufacturing processes, the latter can translate into a potentially important economic benefit.

During the past two decades, several light scattering technologies used for particle characterization have matured and even become a key part of industrial production lines [149]. These techniques may be classified into three main categories: static light scattering (SLS), dynamic light scattering (DLS), and scattering tracking analysis (STA). In the first class, the measured scattering signal results from the light-particle interaction at various spatial locations, whereas in the second and third, the recorded signal results from the monitoring of light-particle interaction as a function of time.

Different techniques aim, or are better suited, for particles in different size classes. Particle dimension ranges from very small, such as viruses (20–100 nm) [150], to larger ensembles such as bacteria colonies of 1–2 mm dimension, with a number of possible shapes [135]. For instance, while dynamic light scattering techniques can resolve particles deep in the submicron region [151], static methods work best in the range of hundreds of μm to mm [152,153]. Here we aim at this regime of size particles, with the smaller particles considered being tens of microns in size.

Static light scattering, also known as laser diffraction (LD) analysis has become the most widely used technique for extracting information about the particle size distribution of an unknown sample [154]. This technique is based both on Mie light scattering theory, and on far-field Fraunhofer diffraction. In LD analysis, the light intensity vs scattering angle is related to the dimensions of the particles participating in the scattering process, with other variables, such as wavelength, kept constant. Thus, information about particle size is extracted from the angular

intensity variation of laser light scattered from a given sample: larger particles scatter light at smaller angles, while smaller particles scatter at wider angles [148]. It is worth pointing out that while for Fraunhofer diffraction the particle size analysis is somewhat straightforward, the Mie scattering approach requires knowledge of the real and imaginary parts of the sample's refractive index [147].

Commercial LD instruments have been used extensively in the industry due to their high precision and reliability. Important drawbacks include their limited portability and their inability to fully discern among different particle shapes. In particular, given that LD is based on the precise detection at different scattering angles, typical instruments require in the region of 16 to 32 detectors positioned at different angles with respect to the main optical axis (see, for instance, Figure 4 of Ref. [149]). Unfortunately, increasing the number of detectors does not necessarily lead to a better resolution [152] and thus, finding the optimum number and location of detectors for a particular application becomes a crucial task. Most LD schemes are based upon the assumption that particles, although different in size, are always spherical; this poses a problem if the goal is to identify samples containing particles with different shapes [155, 156].

Although it is well known that particle shape influences the properties and behavior of substances, for example affecting material strength and deformation mechanisms [157] as well as the compaction/flux of powders [158], it remains challenging to determine it experimentally. Some studies have used LD for the development of sensors to obtain particle shape information for online process control and monitoring, however, these have only achieved limited success [159,160]. Many different measures have been suggested for the characterization of particle shape, involving roundness and angularity (sharpness) [161, 162]. More rigorously, extensions of the Mie theory for arbitrarily-shaped particles can be approached numerically; however, applying such numerical solutions to mixtures of many particles would be computationally very costly [163, 164].

Neural network (NN) algorithms have been applied for particle characterization allowing for the estimation of relevant parameters such as particle size and concentration. In addition, they have also been shown to outperform ill-conditioned inverse scattering problems in Mie theory by reducing significantly the required computational time [165]. In this sense, Machine Learning (ML) techniques are known to be powerful for pattern recognition in large data sets, providing reliable parameter estimation. The standard procedure is to train NNs with either experimental or synthetic data spanning the parameter range of interest, and subsequently estimate the desired parameters by using measurements as input to the trained NN [166]. The key point is that NNs make use of their self-learning capabilities to enhance the performance of optical systems in terms of reliability and resolution without the need to increase their complexity. ML techniques have been applied for particle shape characterization by recognizing the morphology of particle aggregation, ref. [167] or by defining the boundaries of each particle from direct imaging measurements [168]. Interestingly, neural networks have been shown to significantly improve the detection of spatial features in out-of-the-lab technologies

such as mobile-phone-based microscopes [169]. These features combined undoubtedly facilitate the deployment of machine-learning-assisted methods in industrial settings.

5.2 Identification of model particle mixtures using artificial intelligence

In this section, we provide the first steps towards "smart" laser diffraction analysis of heterogeneous mixtures [170]. This technique makes use of **a** trained artificial NN to identify spatial features of heterogeneous mixtures of microscopic objects. Our analysis relies on monitoring the far-field diffraction pattern produced by laser light impinging on two-dimensional arrays of model particles which, for the sake of simplicity and generality, are simulated with the help of a DMD. We would like to point out that, although these model particles are not real three-dimensional objects, they exhibit certain advantages [171, 172]. In particular, given their two-dimensional nature, they reasonably fulfill the theoretical pre-assumptions for Fraunhofer diffraction, and by excluding other possible effects derived from real three-dimensional particles help focus our attention on the advantages of using smart technologies, i.e., those based on pre-programmed rules or patterns learned during a training stage, for laser diffraction analysis.

The technique hereby proposed, in which relevant sample information is reliably extracted from a single and static far-field diffraction pattern, offers two main advantages over typical LD devices. Firstly, it allows for efficient particle identification by detecting the signal within a small angle ($\sim 0.26°$) with respect to the light propagation axis, thus effectively reducing the number of detectors needed for its implementation, as is also the case in recent micro- and nano-particle identification proposals that make use of ML algorithms [165, 173–177].

Secondly, our technique permits the identification of particle shapes in two-component heterogeneous mixtures resolving the shapes of the particles that make up the mixture, as opposed to currently available techniques in which only the particle size can be obtained [170, 178]. In addition, this proposed technique allows for the determination of the predominance (or balance) between particle geometries. These features might be relevant for monitoring particle contamination in industrial manufacturing processes [179].

To generate a large set of different particle mixture configurations, we create objects of different geometries and sizes using a DMD consisting of a 6.57 mm $\times$ 3.69 mm chip containing a grid of square mirrors of 7.63 µm per side. The mirrors can be selectively rotated $\pm 12°$ in an "on" or "off" configuration such that when illuminated, the DMD reflects light selectively.

The DMD is illuminated with a 405 nm wavelength collimated beam of 2.46 mm diameter. The beam size is set to be smaller than the DMD window to avoid diffraction effects caused by the borders of the chip. Each object in the mixture corresponds to a contiguous array of mirrors in the "on" configuration that reflects

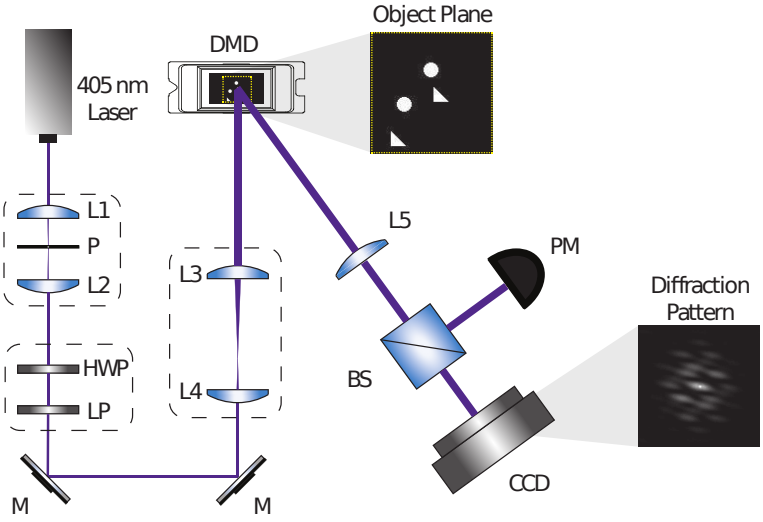

Figure 5.1: Experimental setup for ML-assisted laser diffraction analysis. A 405 nm laser beam, spatially filtered with two lenses (L1 and L2) and a pinhole (P), is expanded with a telescope system (L3 and L4) to illuminate a Digital Micromirror Device (DMD). The power of the illumination beam can be controlled using a Half-wave Plate (HWP) followed by a Linear Polarizer (LP). The light reflected by the DMD passes through a Fourier transform lens (L5), and the diffraction pattern is collected by a CCD camera at the focal plane of the Fourier lens L5. The power of the signal after L5 was measured using a beam splitter (BS) and a power meter (PM).

a part of the beam. The objects are randomly positioned on the DMD plane assuring no overlap between particles. Due to the periodicity of the mirror grid, a mesh of diffraction order beams is produced. A single diffraction order is selected to be transmitted through a Fourier transform lens, and the diffraction pattern is collected with a CCD camera, as shown in Figure 5.1. Note that due to the dimensions of the beam, the model particle images, and the focal length of the Fourier lens L5 (200 mm), the DMD diffraction orders are naturally separated with propagation, so that no additional spatial filtering is required to isolate a single diffraction order. The collected diffraction patterns are stored as bitmaps, scaling the intensity values monitored with the CCD camera to 8-bits, associating the maximum intensity (saturated detector) to 255 gray-scale values.

We consider mixtures of microscopic particles. The aim is to retrieve information such as their size, geometry (shape), and concentration. To demonstrate in principle the effectiveness of the method, in this work we consider only three geometries, namely: squares, triangles, and circles. However, our results seem to indicate that one can consider two-dimensional arbitrarily shaped objects in more general scenarios, given that the different shapes to be identified produce a spatial far-field pattern which is sufficiently distinguishable. These mixtures are analyzed

Table 5.1: Beam power as a function of the illuminated area in the DMD.

Number of Pixels	**Power [μW]**
≤500	200
501–1000	100
1001–1500	50
1501–3000	25
≥3001	15

following the steps shown as a flowchart in Figure 5.3 a.

To demonstrate that we can successfully retrieve the sought-after information about the microscopic objects, we carry out two different experiments. The first experiment (Experiment #1) aims at recognizing sets of microscopic objects that have the same shape but different characteristic lengths; in this case: 11, 15, 21, or 25 times the DMD mirror length (7.63 μm). The total number of particles varies from one to five.

The second experiment (Experiment #2) considers mixtures containing two types (out of the three available geometries) of microscopic objects. In this experiment, the size of the particles is kept constant (15 micromirrors), while the total number of objects ranges from 2 to 10. All possible combinations $n_1 + n_2 = N$ are considered, where n_1 and n_2 are the number of sources belonging to geometries 1 and 2, respectively. The dataset for each experiment is created by randomly assigning the position of the objects, avoiding any overlap between them, and registering their corresponding far-field diffraction pattern. One hundred diffraction patterns were considered for each category. Given the total number of combinations of size, shape, and number of objects, Experiment #1 contains 6000 experimental diffraction patterns, while Experiment #2 includes 19,200 patterns.

Due to the quadratic scaling of the illuminated area with the increase of the particles' characteristic length, the intensity of the diffraction pattern increases accordingly. Thus, in order to avoid saturation of the detector, and incomparable powers of the stored diffraction patterns, the power of the initial illumination beam was selected according to the total illuminated area; more precisely, the total number of pixels in the "on" configuration, which varied from 66 pixels (corresponding to a triangle of 11 pixels per side) up to an almost fifty times larger illuminated area of 3125 pixels (corresponding to five squares of 25 pixels per side). Table 5.1 summarizes the power of the illuminating beam for each case.

Because the illumination beam has a Gaussian profile, the power reflected by the DMD strongly depends on the distribution of the particles; the particles closer to the center of the beam will reflect more intense light than particles far from the center. Tailored illumination with uniform intensity profile such as top-hat beams would prevent this from happening, however, this requires alternative beam shaping equipment. To take these variations into account, we make sure that, in each case, the collected images had the same mean total power. To do

so, the exposure time of each measurement was selected such that no pixel of the CCD camera recorded an intensity larger than 250 (gray-scale), being 255 the saturation value, additionally the integrated signal of all pixels yield the same value for all measurements. A general description of the data collection methodology is summarized in the pseudo-code shown in Algorithm 1.

Algorithm 1: Pseudo-code of experimental data collection.

```
for Select Illumination beam power do
    for Select geometry category do
        for Select total number of particles N do
            Compute total number of Pixels
            Set initial exposure time
            if Total number of pixels ∈ pixel interval then
                for i = 1 : 100 do
                    Generate source plane with non-overlapping particles
                    Project source plane in the DMD
                    Collect diffraction pattern
                    Verify image saturation
                    while Image is underexposed or saturated do
                    end
                    Update exposure time
                    Collect diffraction pattern
                    Verify image saturation
                    Measure signal power
                    Save diffraction pattern
                end
            end
        end
    end
end
```

Examples of the collected diffraction pattern intensities experimentally measured $[I_E(\mathbf{x})]$ are shown in Figure 5.2 and compared with the corresponding theoretical predictions $[I_T(\mathbf{x})]$, generated using a far field FFT-based algorithm that describes the scattering process. Here $\mathbf{x} = (x, y)$ designates the transverse coordinate on the measuring plane. To evaluate the degree of similarity between experiment and theory, we make use of the overlap parameter [180]

$$\Omega = \frac{\left[\int I_E^{1/2}(\mathbf{x}) I_T^{1/2}(\mathbf{x})\, \mathrm{d}\mathbf{x}\right]^2}{\left[\int I_E(\mathbf{x})\, \mathrm{d}\mathbf{x}\right]\left[\int I_T(\mathbf{x})\, \mathrm{d}\mathbf{x}\right]}, \tag{5.1}$$

where $\Omega = 1$ corresponds to a perfect overlap between the theoretical prediction and the experimental measurement. Note that in all of the cases that we have evaluated, the overlap parameter is $\Omega \geq 0.9$.

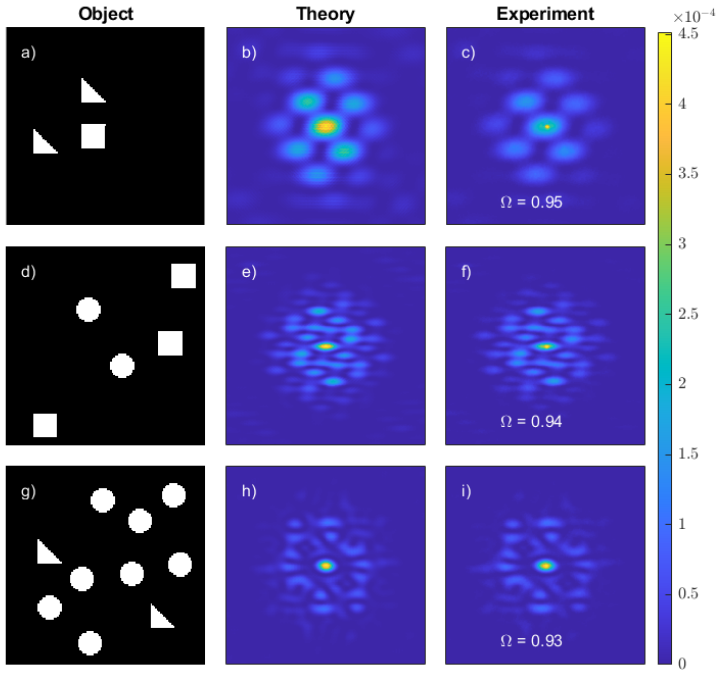

*Figure 5.2: Comparison between simulated and measured diffraction patterns. (**a**,**d**,**g**) show examples of the objects generated with the Digital Micromirror Device (DMD). (**b**,**e**,**h**) are the theoretically predicted diffraction patterns created by the objects depicted in the leftmost column. (**c**,**f**,**i**) are the experimentally measured diffraction pattern. Note that the images are normalized, so that the integrated signal over the detection area adds up to unity. In all cases, the overlap parameter Ω is found to be larger than 0.9.*

5.2.1 Machine learning architecture and data processing

All the algorithms used in our protocol are based on multi-layer feed-forward networks [181]. Hidden layers feature neurons that perform operations on the data using synaptic weights and a nonlinear activation function, the so-called sigmoid function. The output layer comprises softmax neurons that provide a probability distribution over predicted output classes [182, 183]. To build accurate and reliable neural networks, a crucial step is to determine an appropriate feature vector that may capture the information encoded in the diffraction patterns. Figure 5.3b shows the image pre-processing method carried out to build the feature vector. We first crop the diffraction pattern to a 400×400 pixel image, retaining only the central portion of the monochromatic high-resolution original images (1280×1024 pixels, normalized to 8 bits) obtained with a CCD camera (Thorlabs DCU224C). After this step, to reduce the data dimensions, we perform a down-sampling process that averages small clusters of 80 by 80 pixels, resulting in a 5-by-5 pixel image. It is worth mentioning that we have tested our algorithms with a larger set of features (pixels) without observing a significant efficiency improvement, as shown in Figure 5.4. The values of identification accuracy that correspond to each one of the feature matrix dimensions are: 78.41 ± 1.94, 94.12 ± 0.75, 94.24 ± 0.65, 94.48 ± 0.41, 94.45 ± 0.32, 94.55 ± 0.2, 94.6 ± 0.12 and 94.77 ± 0.1 (all values correspond to accuracy percentage). Finally, we rearrange the resulting intensity distribution as a column vector, with the total measured intensity included as a 26th element of the resulting feature vector V_1, depicted by the red rectangle in Figure 5.3c.

Our neural networks undergo two stages, namely training, and testing. We train the classification networks using the scaled conjugate gradient back-propagation algorithm [184], while the performance is evaluated through the cross-entropy [185, 186]. We devote 70% of the dataset to training, 15% to validation, and 15% to testing, as is standard in ML protocols [187, 188]. In all cases, the training of the neural networks was carried out with balanced data, that is, the training dataset contains the same number of observations for each one of the classes. It is worth mentioning that the testing data was excluded from the training phase, thus providing an unbiased evaluation of the algorithm's overall accuracy. A limit of 1000 epochs was set for each network training stage. Both training and testing stages were performed with MATLAB 2019a which runs on a computer with an Intel Core i7-4710MQ CPU (@2.50 GHz) and 32 GB of RAM. After the training stage, our networks can make predictions of the shape, size, and the number of microscopic objects in a given sample using as input the diffraction pattern and the total intensity, as shown in Figure 5.3c. In what follows, we provide a thorough description of the steps followed in each experiment.

In Experiment #1, we implement three neural networks connected in series, each one of them performing a specific prediction of the features of the initial field. The first neural network identifies the shape of the objects. It is trained by using a concatenation of the total intensity (signal power) and the down-sampled representation of the diffraction pattern, i.e., the feature vector V_1 [see Figure

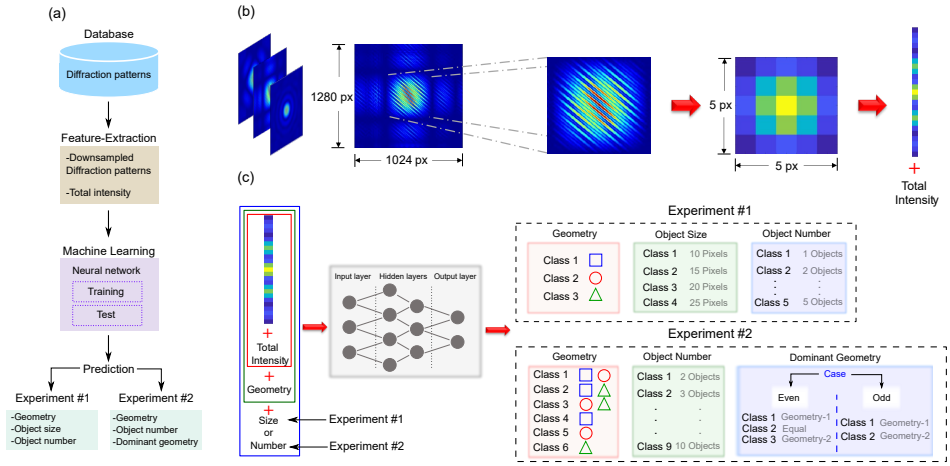

*Figure 5.3: Machine-learning-assisted particle mixture identification protocol. (**a**) Flowchart of the machine learning algorithms used for extracting information from intensity-only measurements of the diffraction patterns. (**b**) Image down-sampling process. The intensity signal extracted from the CCD camera is presented in false color for the sake of clarity of the presentation. (**c**) Flow diagram of the neural networks used in each phase of the experiments described in the main text.*

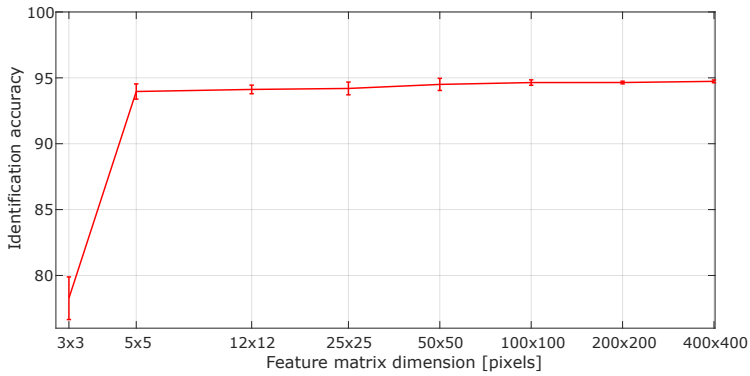

Figure 5.4: Identification accuracy as a function of the feature matrix dimension. Error bars indicate standard deviations.

5.3b]. The second network, identifying the object size, makes use of the prediction of the first network to create the feature vector $V_2 = V_1 + \textit{geometry (shape)}$, whereas the third network extracts the object number from the feature vector $V_3 = V_2 + \textit{size}$. Figure 5.3c summarizes the structure of the neural networks and the predicted classes. The core feature-vector V_1 is initially introduced in the network that identifies the shape. Then, its output acts as input for the second network, in conjunction with the core feature vector. Once the object size has been determined, the third neural network predicts the number of objects using as input the core feature-vector, as well as the outputs of the first and second networks.

In Experiment #2, we follow a similar strategy. We first implement a neural network that determines the combined-geometry (shape) class—i.e., the two shapes of the objects which make up the mixture—by using the feature vector, comprising the down-sampled diffraction pattern and the total measured intensity. With the geometry-class identified and the core feature-vector, we then determine the total number of objects. Finally, by making use of the core feature-vector, as well as the outputs of the first and second networks, we predict the dominant shape. Note that the last network has been divided into two cases: odd and even number of objects. This is due to the fact that when the number of objects is even, we need to define three output classes depending on the concentration ratio, namely (1) larger number of the first geometry, (2) larger number of the second geometry, (3) equal number of model particles of both geometries. For an odd number of objects, there are only two classes. Also note that the class labeled as Geometry-1 (Geometry-2) in Figure 5.3 refers to the first (second) object-shape in each of classes 1, 2, and 3. It is important to note that in both experiments, all of the data which serves as input to the neural network (both for training and for evaluation), is obtained experimentally through far-field diffraction.

5.2.2 Experimental results

We have performed a blind test of our neural networks on the remaining 15% of the collected data. We obtain an overall >90% identification accuracy in every stage of the experiments. Table 5.2 summarizes the results of each experiment (see Figure 5.5 for details on the network success rate for each task), including the overall accuracy, the number of hidden layers, and the number of neurons in each layer.

In Experiment #1, featuring collections of one single type (shape) of particle, the first NN can identify the shape of the model particles with a 99% accuracy using a single hidden layer with 5 neurons. The second NN for the determination of particle size showed the same performance, with the same architecture. For the case of the particle number, the architecture of the NN involves two hidden layers with 20 and 5 neurons, respectively, resulting in a 93% identification accuracy.

We remark that in experiment #1 which involves collections of a single type of particle, each one randomly positioned, we can obtain information about particle shape, size, and total number from inputting a single diffraction pattern to our

Table 5.2: Overall accuracy, number of hidden layers, and number of neurons in each layer for the neural networks implemented in the described experiments.

Experiment	Neural Network	Accuracy	Number of Hidden Layers	Number of Neurons by Layer
1	Geometry	99%	1	5
	Object Size	99%	1	5
	Object Number	93%	2	Layer 1 = 20; Layer 2 = 5
2	Geometry	94%	2	Layer 1 = 30; Layer 2 = 20
	Object Number	92%	2	Layer 1 = 80; Layer 2 = 50
	Dominant geometry (even)	95%	2	Layer 1 = 30; Layer 2 = 20
	Dominant geometry (odd)	98%	2	Layer 1 = 30; Layer 2 = 20

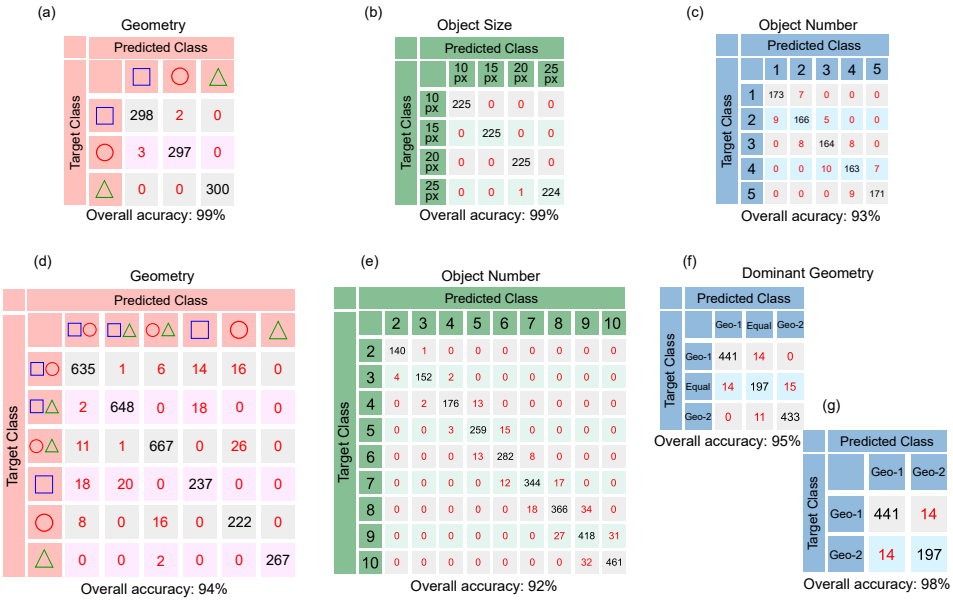

*Figure 5.5: Confusion matrices summarizing the performance of machine-learning algorithms for particle mixture identification. The top row shows the confusion matrices containing information about the correct and incorrect predictions for (**a**) geometry (shape), (**b**) model particle characteristic size, and (**c**) number of objects of the Experiment #1. The bottom row presents the confusion matrices for (**d**) geometry (shape), (**e**) number of model particles, and (**f**,**g**) dominant geometry (shape) of the Experiment #2. (**f**,**g**) matrices correspond to the case in which the number of objects is even and odd, respectively. In all cases, the diagonal elements of the matrices represent successful recognition, i.e., true-positives and true-negatives, whereas off-diagonal elements represent failed attempts, false-negatives, and false-positives.*

Table 5.3: Computation time for test and training of the neural networks used in each experiment.

Experiment	Neural Network	Training [s]	Test [s]
1	Geometry	$2.308 \times 10^{-1} \pm 2.7 \times 10^{-3}$	$7.1 \times 10^{-3} \pm 6.7 \times 10^{-7}$
	Object Size	$2.491 \times 10^{-1} \pm 4.7 \times 10^{-3}$	$7 \times 10^{-3} \pm 5.2 \times 10^{-7}$
	Object Number	$3.905 \times 10^{-1} \pm 9.9 \times 10^{-3}$	$7.2 \times 10^{-3} \pm 2 \times 10^{-7}$
2	Geometry	$4.7212 \pm 7.471 \times 10^{-1}$	$1.2 \times 10^{-2} \pm 1.4 \times 10^{-6}$
	Object Number	$1.57444 \times 10^{1} \pm 4.6636$	$1.82 \times 10^{-2} \pm 2.4 \times 10^{-6}$
	Dominant geometry (even)	$1.045 \pm 6.1 \times 10^{-2}$	$2.7 \times 10^{-5} \pm 9.9 \times 10^{-10}$
	Dominant geometry (odd)	$9.513 \times 10^{1} \pm 6.5 \times 10^{-2}$	$2.1 \times 10^{-5} \pm 2.7 \times 10^{-9}$

three cascaded NNs, in contrast to other schemes which analyze each particle on a one-by-one basis [159, 160].

For experiment #2, featuring heterogeneous mixtures of two types (shapes) of particles, our NN uses two hidden layers. The shape of the particles was retrieved with 94% accuracy using 30 and 20 neurons, respectively; while for the total number of model particles, 80 and 50 neurons were needed for an identification accuracy of 92%. Finally, two layers with 30 and 20 neurons were required to determine the dominant shape obtaining 95% accuracy for the even total number of particles and 98% for the odd number of particles.

We measured the execution time in both training and test stages to quantify the computational cost in terms of the processing time. Table 5.3 shows a comparison of the execution time for all the proposed neural networks. Note that, in general, while our algorithms require less than 30 s to be trained, the test time is significantly less than that of the training, around a few tens of milliseconds.

It is worth mentioning that although the data preparation and processing can be considerably time-consuming, once the training phase has been completed, our neural network can process newly-acquired data (prepared in the same format as used for training) in timescales of milliseconds.

We have demonstrated an optical technique for particle mixture identification, with potential applications in research and industry, based on machine-learning-assisted laser diffraction analysis. The technique proposed facilitates a fast and accurate identification of the particle's shape, size, and total number in the case of collections of a single particle type (shape). Likewise, it leads to fast and accurate identification of the geometry of constituent particles, particle size, and dominant geometry in the case of binary non-heterogeneous mixtures. We have verified that the method works detecting arrays of randomly located model particles generated with the help of a DMD. It is worth pointing out that machine learning and deep learning algorithms have been used to improve optical microscopy [169, 189–191]. Interestingly, by using neural networks as classifiers or feature extractors, in some cases trained with synthetic data and tested in real measurements, these types of techniques have shown to be effective for impurity recognition in semiconductors [192, 193].

In our work, by making use of a digital micromirror device, we have simulated

mixtures of particles of different sizes and geometries with a different total number of model particles. By analyzing the resulting far-field diffraction pattern, our neural network algorithm can extract the spatial features of the mixtures. Relying on a total of 24,900 diffraction patterns and a 70/15/15 ratio for training, validation, and testing data, respectively, the identification performance remained above 90%. Because of its reliability and ease of implementation, our technique may be of great importance for different scientific and technological disciplines, as it establishes a new route towards the development of novel smart identification devices for sample classification and particle contamination monitoring.

Chapter 6

Summary and conclusions

Modern imaging and optical metrology techniques have led to resolution improvements beyond the standard diffraction limit. This has motivated a more detailed and robust description of resolution that can be addressed from a quantum-mechanical point of view. Quantum estimation and statistical inference theory provide the tools to determine the estimation precision limit by means of the Crámer-Rao lower bound, which has two direct implications. On the one hand the quantum Crámer-Rao bound gives a fundamental limit for estimation precision that one can aim to for a given light-matter interaction. On the other hand, the so called classical Crámer-Rao lower bound states the maximum precision that a certain measuring strategy allows. These results derive in a modern description of Rayleigh's resolution criterion as well as a quantitative evaluation of the sensitivity of the measuring technique that can be compared to the fundamental limit.

Depending on quantum state model and the number of parameters to be estimated, several methods to compute the Crámer-Rao lower bound are reported in the literature. In this thesis we explicitly compute and evaluate the validity of different bounds for a particular case. We consider the estimation of the time delay and frequency shift induced to a state of light after interacting with a moving target when using pairs of entangled photons in a quantum Lidar system. We show that the different bounds and their validity depend on the degree of entanglement.

Apart from the characteristics of the system and the parameters of interest, the quantum state model selection is also relevant for the estimation limit. We show a discrepancy for parameter estimation between two particular photonic models, namely N copies of a single photon and a multimode coherent state with average number of photons N.

Furthermore, in this thesis we explore the effects of noisy environments on the informational content of quantum states. In particular, we study quantum correlations beyond entanglement for quantum phase estimation. We consider N00N states and calculate the local quantum uncertainty and quantum discord, which quantifies the decrease of the informational content when losses are present.

Once the fundamental Crámer-Rao lower bound for a particular parameter

estimation is given, one can compare the attainable estimation precision for a given measurement strategy to the fundamental limit. This not only allows to quantify the resolution enhancement of the measurement strategy, but also allows to design or optimize measurement strategies that allow to attain or asymptotically approach the lower bound. We show this discrepancy using two examples, the estimation of the propagation parameters of an optical fiber as a dispersive medium, and the estimation of the spatial features of a nanostructure; both inducing phase changes to the optical field.

Modal methods have shown to be effective to optimally attain the lower bound. In this thesis we propose a method to retrieve the full amplitude and phase modal decomposition of an arbitrary beam using a homodyne spatial mode analyzer. The operation principle of this technique is the combination of two fields using a balanced beam splitter, namely the optical field of interest with the field of a local oscillator holding a single mode. The output signals of the beam splitter ar substracted in a standard homodyne detection scheme such that by varying the phase of the local oscillator mode, the complex coefficients of the modal decomposition can be retrieved.

Additionally, without the need of interferometric methods nor complex mode projections, we propose a technique to extract modal information by encoding azimuthal phases to optical beams using spatial light modulators, followed by projection onto a Gaussian mode. We apply this technique to the two-dimensional localization of an optical beam in the transverse plane. We perform a sensitivity analysis and compare the results with the fundamental lower bound as well as with other methods currently used.

Since modal methods have shown to be optimal in some particular cases, we present a method to compute a basis of modes that allow an optimal estimation of the parameters. We include as an example the estimation of the height and sidewall angle of a cliff-like nanostructure, relevant in the semiconductor industry.

Finally, motivated by the information carried by optical beams that is not easily accessible, we explore the possibility of extracting information about spatial features of microscopic objects by using machine learning algorithms combined with laser diffraction analysis. We show that machine learning algorithms are able to identify spatial features of microscopic objects from their diffraction patterns without the need of solving the inverse problem nor the use of extensive scattering theory.

Future work

Although the majority of the results in this thesis are theoretical; at the heart of this research project we aim at direct applications in metrology. The main interest of this research is to establish and evaluate feasible methods for highly sensitive metrology. We aim at imaging and non-imaging techniques based on spatial mode projections that allow to resolve and measure nanoscopic spatial features of objects with sub-wavelength resolution. Using the theoretical results and simulations

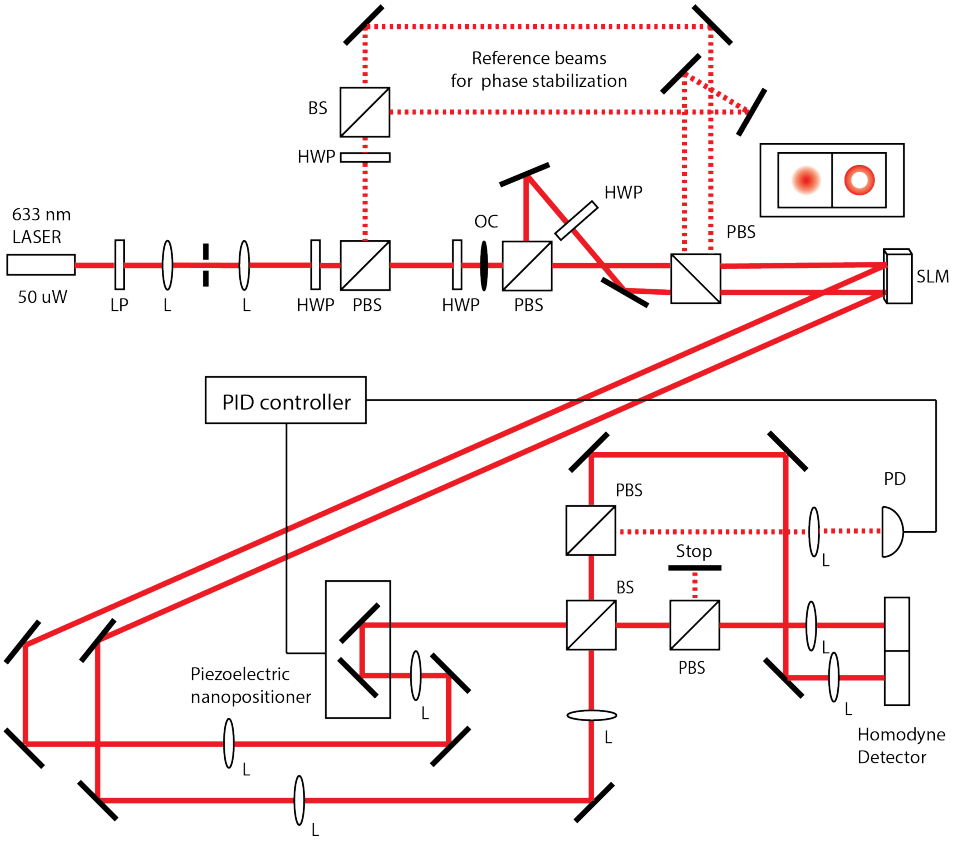

Figure 6.1: Experimental implementation of a homodyne spatial mode analyzer.

presented in this thesis, we hereby propose the foreseen follow up research to be carried out in the near future in terms of experimental implementation of spatial mode sensing.

We expect to carry out the experimental implementation of the methods presented in Sections 3.3 and 3.4. The setup resented in figure 3.9 is expected to be used in two scenarios. First, to experimentally demonstrate the results of Section 3.4.1 for two-dimensional beam localization in the transverse plane using azimuthal mode phase encoding. Second, this method is intended to be used for measurements of orientation of objects following an equivalent procedure.

Moreover, the homodyne spatial mode analyzer (see figure 6.1) is intended to be used for optimal phase estimation using the optimal modes presented in Section 4.2. In particular, for optimal estimation of spatial features of phase objects. We expect to use cliff-like nanostructures as well as diffraction grating in which the characteristic parameters are the height, period, critical dimension (width at half height) and sidewall angles.

Finally, in collaboration with groups at TU Delft, VSL and ASML Research, we expect to perform computational spatial mode projections for super-resolution optical metrology. Using measured data of the complex field (amplitude and phase) obtained by phase retrieval methods using pthychography, we intend to computationally project onto the basis of spatial modes that allow optimal estimation; leading to saturation of the Crámer-Rao lower bound.

Appendix A

Explicit computation of the Holevo bound for a quantum Lidar system

Although the computation of the Holevo bound is not straightforward in general, we can apply the same procedure used by Bradshaw et. al. in [194].

It is first needed to find an orthonormal basis of vectors $\{|e_0\rangle, |e_1\rangle, |e_2\rangle\}$ in which we can decompose the sate $|\Psi_0\rangle$ and its derivatives with respect to the parameters $(\boldsymbol{\theta} = (\theta_1, \theta_2))$ $|\Psi_1\rangle \equiv \langle \partial_1 \Psi|$ and $|\Psi_2\rangle \equiv \langle \partial_2 \Psi|$. To do so, we redefine the variables as dimensionless variables $\tau \to \frac{\tau}{T}$ and $\delta \to \frac{\delta}{W}$. Since the Holevo CR bound is asymptotically attainable with an adaptive measurement scheme, we evaluate at $(\tau, \delta) \to 0$. The state and its derivatives are expressed in terms of the orthonormal basis as:

$$|\Psi_0\rangle = |e_0\rangle, \tag{A.1}$$

$$|\Psi_1\rangle = \sqrt{\tfrac{WT}{2}} \cosh r |e_1\rangle + \sqrt{\tfrac{WT}{2}} \sinh r |e_2\rangle, \tag{A.2}$$

$$|\Psi_2\rangle = i\omega_s^o T |e_o\rangle + i\sqrt{\tfrac{WT}{2}} \cosh r |e_1\rangle - i\sqrt{\tfrac{WT}{2}} \sinh r |e_2\rangle. \tag{A.3}$$

Here r is such that $\cosh 2r = 2WT$. Using the expressions above; the conditions $Tr[\rho X^i] = 0$ and $Tr[\partial_i \rho X^j] = \delta_{ij}$, are explicitly:

$$\mathrm{Re}\{\cosh r \langle e_0| X_1 |e_1\rangle + \sinh r \langle e_0| X_1 |e_2\rangle\} = \tfrac{1}{\sqrt{\cosh 2r}}, \tag{A.4}$$

$$\mathrm{Re}\{\cosh r \langle e_0| X_2 |e_1\rangle + \sinh r \langle e_0| X_2 |e_2\rangle\} = 0, \tag{A.5}$$

$$\mathrm{Re}\{i \cosh r \langle e_0| X_1 |e_1\rangle - i \sinh r \langle e_0| X_1 |e_2\rangle\} = 0, \tag{A.6}$$

$$\mathrm{Re}\{i \cosh r \langle e_0| X_2 |e_1\rangle - i \sinh r \langle e_0| X_2 |e_2\rangle\} = \tfrac{1}{\sqrt{\cosh 2r}}. \tag{A.7}$$

Splitting the matrix elements in its real and imaginary parts as:

$$\langle e_0| X_1 |e_1\rangle = t_1 + ij_1, \tag{A.8}$$
$$\langle e_0| X_1 |e_2\rangle = s_1 + ik_1, \tag{A.9}$$
$$\langle e_0| X_2 |e_1\rangle = t_2 + ij_2, \tag{A.10}$$
$$\langle e_0| X_2 |e_2\rangle = s_2 + ik_2; \tag{A.11}$$

one can rewrite the conditions (A.4-A.7) as:

$$t_2 = -s_2 \tanh r, \tag{A.12}$$
$$j_1 = k_1 \tanh r, \tag{A.13}$$
$$t_1 = \tfrac{\operatorname{sech} r}{\sqrt{\cosh 2r}} - s_1 \tanh r, \tag{A.14}$$
$$j_2 = -\tfrac{\operatorname{sech} r}{\sqrt{\cosh 2r}} + k_2 \tanh r. \tag{A.15}$$

Using the definition in Section 2.2.1, the elements of the matrix $Z[\vec{X}]$ are written as:

$$Z_{11} = |\langle e_0| X_1 |e_1\rangle|^2 + |\langle e_0| X_1 |e_2\rangle|^2, \tag{A.16}$$
$$Z_{12} = \langle e_0| X_1 |e_1\rangle \langle e_1| X_2 |e_0\rangle + \langle e_0| X_1 |e_2\rangle \langle e_2| X_2 |e_0\rangle, \tag{A.17}$$
$$Z_{21} = \langle e_0| X_2 |e_1\rangle \langle e_1| X_1 |e_0\rangle + \langle e_0| X_2 |e_2\rangle \langle e_2| X_1 |e_0\rangle, \tag{A.18}$$
$$Z_{22} = |\langle e_0| X_2 |e_1\rangle|^2 + |\langle e_0| X_2 |e_2\rangle|^2. \tag{A.19}$$

Considering the weight matrix $\mathbf{G} = diag[1, z]$ $(z > 0)$, the Holevo function $h[\vec{X}]$ becomes:

$$h = f + 2|g|\sqrt{z}, \tag{A.20}$$

where f and g are functions that depend on (s_1, k_2, k_1, s_2) as

$$\begin{aligned} f =& t_1^2 + j_1^2 + s_1^2 + k_1^2 + z(t_2^2 + j_2^2 + s_2^2 + k_2^2) = \\ =& (s_1^2 + k_1^2 + zk_2^2 + zs_2^2)(1 + \tanh^2 r), \\ &+ (1+z)\tfrac{\operatorname{sech}^2 r}{\cosh 2r} - 2(s_1 + zk_2)\tfrac{\operatorname{sech} r \tanh r}{\sqrt{\cosh 2r}}. \end{aligned} \tag{A.21}$$

$$\begin{aligned} g =& - j_1 t_2 - k_1 s_2 + j_2 t_1 + k_2 s_1 = \\ =& (k_2 s_1 - k_1 s_2)(1 - \tanh^2 r) - \tfrac{\operatorname{sech}^2 r}{\cosh 2r} \\ &+ \tfrac{\operatorname{sech} r \tanh r}{\sqrt{\cosh 2r}}(s_1 + k_2) \end{aligned} \tag{A.22}$$

The Holevo function $h[\vec{X}]$ needs to minimize to find the Holevo CR bound. To do so, we use the Karush-Kuhn-Tucker (KKT) conditions as described in Appendix B.1. Two different cases are considered, $g < 0$ and $g > 0$. The KKT conditions are

- If $g < 0$:

$$\begin{cases} -\nabla h = \lambda \nabla g, \\ g < 0, \\ \lambda \geq 0, \\ g\lambda = 0. \end{cases} \tag{A.23}$$

The potential minimum corresponds to:

$$\begin{pmatrix} s_1^* \\ k_2^* \\ k_1^* \\ s_2^* \end{pmatrix} = \begin{pmatrix} -\frac{\sinh r}{\sqrt{\cosh 2r}} \frac{4z+4z\cosh 2r+4z^{\frac{3}{2}}\cosh 2r+4z^{\frac{3}{2}}}{4z-4z\cosh^2 2r} \\ -\frac{\sinh r}{\sqrt{\cosh 2r}} \frac{4z+4z\cosh 2r+4\sqrt{z}\cosh 2r+4\sqrt{z}}{4z-4z\cosh^2 2r} \\ 0 \\ 0 \end{pmatrix}. \tag{A.24}$$

Substituting this solution in the expression for g (A.22), one has:

$$g = -\frac{\operatorname{sech}^2 r}{\cosh 2r}\left(1 - \frac{(1+\sqrt{z})^2}{\sqrt{z}} \frac{2\sinh^2 r + 1}{4\sinh^2 r}\right) > 0. \tag{A.25}$$

Which has no solution; then there is no valid solution for $g < 0$.

- If $g \geq 0$:

$$\begin{cases} -\nabla h = -\lambda \nabla g, \\ g > 0, \\ \lambda \geq 0, \\ g\lambda = 0. \end{cases} \tag{A.26}$$

Two cases fulfill the condition $g\lambda = 0$, namely:

  - $\lambda = 0$:

$$\begin{pmatrix} s_1^* \\ k_2^* \\ k_1^* \\ s_2^* \end{pmatrix} = \begin{pmatrix} \frac{1-\sqrt{z}}{\sinh r\sqrt{\cosh 2r}} \\ \frac{\sqrt{z}-1}{\sinh r\sqrt{z}\sqrt{\cosh 2r}} \\ 0 \\ 0 \end{pmatrix}. \tag{A.27}$$

    The function g becomes:

$$g = -\frac{\operatorname{sech}^2 r}{\cosh 2r}\left(1 + \coth^2 r \frac{(1-\sqrt{z})^2}{\sqrt{z}}\right) < 0 \tag{A.28}$$

    Which is again not a valid solution.

  - $g = 0$:

The variables s_2^* and k_1^* are equal to zero and s_1^*, k_2^* are the solution of the system:

$$\begin{cases} g = k_2^* s_1^* (1 - \tanh^2 r) - \frac{\operatorname{sech}^2 r}{\cosh 2r} + \frac{\operatorname{sech} r \tanh r}{\sqrt{\cosh 2r}} (s_1^* + k_2^*) = 0, \\ s_1^* = -\frac{\sinh r}{\sqrt{2WT}} \frac{4z+2\lambda z-4\lambda\sqrt{z}+\lambda^2-4z^{3/2}+8TWz-8TWz^{3/2}+4TW\lambda z}{4z-4\lambda\sqrt{z}+\lambda^2-16T^2W^2z}, \\ k_2^* = -\frac{\sinh r}{\sqrt{2WT}} \frac{2\lambda+4z-4\lambda\sqrt{z}+\lambda^2-4\sqrt{z}+4TW\lambda+8TWz-8TW\sqrt{z}}{4z-4\lambda\sqrt{z}+\lambda^2-16T^2W^2z}. \end{cases} \tag{A.29}$$

The solution for $\lambda > 0$, is obtained numerically.

We are particularly interested in the solution for $\gamma(z = 1)$ (see Appendix B). It is possible to find the analytic solution for the system in (A.29) corresponding to $\lambda = 4 \cosh r e^{\pm r}$, which implies

$$s_1^* = k_2^* = \frac{\mp e^{\pm r}}{\sqrt{\cosh 2r}}. \tag{A.30}$$

From this two possible solutions for $(s_1^*, k_2^*, k_1^*, s_2^*)$ we take the one that minimizes $h[\vec{X}] = f + 2g$.

Finally, the Holevo bound after reversing the transformation for dimensionless units is

$$W^2 V(\tau) + T^2 V(\delta) \geq \cosh 2r \; e^{-2r}, \tag{A.31}$$

which can also be written as:

$$W^2 V(\tau) + T^2 V(\delta) \geq 2WT \left(2WT - \sqrt{4T^2W^2 - 1} \right). \tag{A.32}$$

Appendix B

Minimization of the bound for simultaneous measurement in a Lidar system

The goal in this section is to find the minimum of the function

$$f = Var(\tau)Var(\delta), \tag{B.1}$$

under a set of inequalities of the form

$$g_i(z_i) = \gamma(z_i) - W^2 Var(\tau) - z_i T^2 Var(\delta) \leq 0, \tag{B.2}$$

for $z_i \in (0, \infty)$ corresponding to a weight in the extimation of τ_s, $\boldsymbol{G} = \text{diag}(1, z_i)$ and the function $\gamma(z)$ corresponds to one of the bounds $C^i(z)$ introduced in Section 2.3.1. To avoid notation, let us define the normalized variables

$$V_1 = \frac{Var(\tau)}{T^2}, \qquad V_2 = \frac{Var(\delta)}{W^2}. \tag{B.3}$$

A set of inequalities, further described in (B.2), defines the area of points (V_1, V_2) shown in Figure B.1 where the minimum can be located, depending on the value of the entanglement parameter TW.

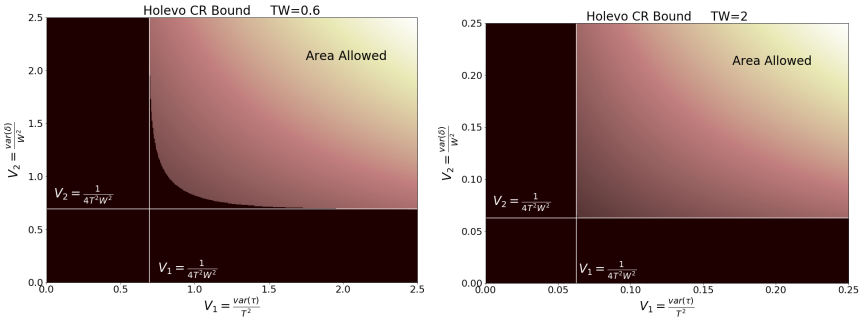

Figure B.1: Values of the s (V_1, V_2) allowed by the Holevo CR bound for estimation of time delay and Doppler shift using a quantum lidar system for two different values of TW: $TW = 0.6$ (left) and $TW = 2$ (right). The gradient of colors represents the value of the product V_1V_2, lighter for higher values. The lines $V_1, V_2 = \frac{1}{4T^2W^2}$ correspond with the vertical and horizontal asymptotes of the sections.

The values in the boundary [1] of this area are given by:

$$V_1' = \frac{1}{(WT)^2}\left(\gamma(z) - z\frac{d\gamma(z)}{dz}\right), \tag{B.4}$$

$$V_2' = \frac{1}{(WT)^2}\frac{d\gamma(z)}{dz}. \tag{B.5}$$

B.1 The Karush-Kuhn-Tucker conditions

To find the values (V_1, V_2) that solve the minimization problem, we make use of the Karush-Kuhn-Tucker conditions defined as follow. The Karush-Kuhn-Tucker (KKT) conditions are necessary conditions that set the solution for a constrained optimization nonlinear problem. They generalize the method of Lagrange multipliers to a problem in which the constraints can be inequalities as well as equalities. The aim is to optimize a function $f(x)$ (called the objective function) subject to both inequality and constant constraints of the form

$$g_i(x) \leq 0 \tag{B.6}$$

$$h_j(x) = 0, \tag{B.7}$$

where $i = 1, ..., m$ and $j = 1, .., n$. The optimization variable is x.

We assume all the functions $f(x)$, $g_i(x)$ and $h_j(x)$ are continuously differentiable at a point x^*. This point x^* is a minimum if there exist constants λ_i and

[1] For each bound $\gamma(z) = C^i$ an area (and boundary) is defined; however, when using the Holevo bound C^H the area is maximal and the boundary is lower than any other bound, meaning that the areas for the other bounds are contained in the one described by the Holevo bound.

μ_j such that the following conditions are satisfied.

$$-\nabla f(x^*) = \sum_{i=1}^{m} \lambda_i \nabla g_i(x^*) + \sum_{j=1}^{l} \mu_j \nabla h_j(x^*) \tag{B.8}$$

$$g_i(x^*) \leq 0 \quad \forall i \tag{B.9}$$

$$h_j(x^*) = 0 \quad \forall j \tag{B.10}$$

$$\lambda_i \geq 0 \quad \forall i \tag{B.11}$$

$$\lambda_i g_i(x^*) = 0 \quad \forall i \tag{B.12}$$

Additionally, if are looking for a maximum instead, condition (B.8) is replaced by:

$$\nabla f(x^*) = \sum_{i=1}^{m} \lambda_i \nabla g_i(x^*) + \sum_{j=1}^{l} \mu_j \nabla h_j(x^*). \tag{B.13}$$

The KKT conditions (B.8)-(B.13) are then reduced to:

$$\nabla f \quad + \textstyle\sum_{i=1}^{N} \lambda_i \nabla g_i = 0, \tag{B.14}$$

$$g_i \quad \leq 0 \qquad i = 1...N, \tag{B.15}$$

$$\lambda_i \quad \geq 0 \qquad i = 1...N, \tag{B.16}$$

$$\lambda_i g_i \quad = 0 \qquad i = 1...N. \tag{B.17}$$

From Eq. (B.14) we have

$$V_1 = \frac{Var(\tau)}{T^2} = \sum_i z_i \lambda_i \tag{B.18}$$

$$V_2 = \frac{Var(\delta)}{W^2} = \sum_i \lambda_i \tag{B.19}$$

From Eq. (B.16) we see that all parameters λ_i should be zero or positive. From Eq. (B.17) we have that if $\lambda_i \neq 0$ we should fulfill $g_i = 0$ so that

$$\frac{\gamma_i}{(WT)^2} = \sum_j z_j \lambda_j + z_i \sum_j \lambda_j. \tag{B.20}$$

The points in the interior of the area allowed correspond to $g_i < 0$ and do not fulfill the KKT conditions. The solution to the minimization problem must be on the boundary. All points (V_1', V_2') on the boundary fulfill a single inequality for a given value of z that we designate as z_0. This is shown in Figure B.2.

If this point fulfills the KKT conditions only one value of λ_i can be different from 0. This is:

$$\lambda_i^0 = \frac{1}{(WT)^2} \frac{\gamma(z_0)}{2z_0}. \tag{B.21}$$

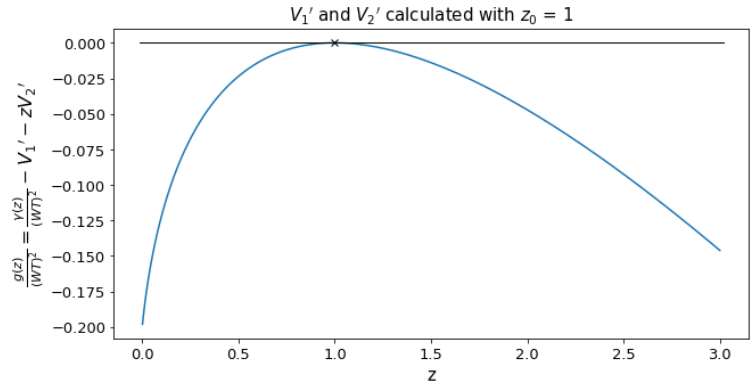

(a) $z_0 = 1$

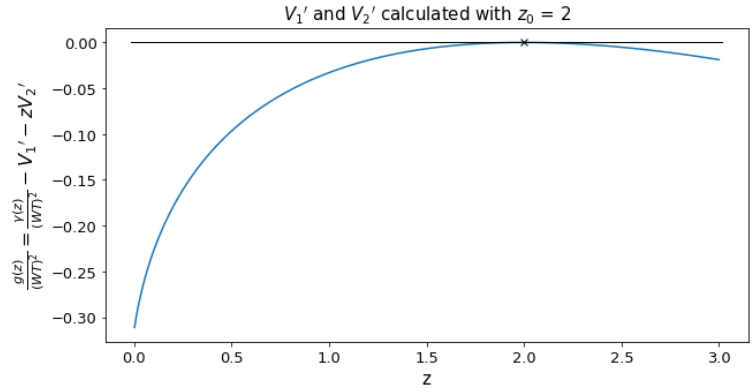

(b) $z_0 = 2$

Figure B.2: Value of the function $\frac{g(z)}{(WT)^2}$ *for the Karush-Kuhn-Tucker minimization problem at two points in the boundary* $(V_1'(z_0), V_2'(z_0))$ *as a function of* z *for* $TW = 0.6$*. The figure on top corresponds to the point in the boundary with* $z_0 = 1$*. Below, we have the same but for the point corresponding to* $z_0 = 2$*. It seen that* $\frac{g(z)}{(WT)^2} = 0$ *only happens for* $z = z_0$*.*

Therefore, using (B.18) and (B.19), we know the points in the boundary that fulfill KKT are:

$$V_1'' = \frac{Var(\tau)}{T^2} = \frac{1}{(WT)^2}\frac{\gamma(z_0)}{2} \tag{B.22}$$

$$V_2'' = \frac{Var(\delta)}{W^2} = \frac{1}{(WT)^2}\frac{\gamma(z_0)}{2z_0}. \tag{B.23}$$

To find the value z_0 we compare the expressions for (V_1', V_2') and (V_1'', V_2''). The minimum will be reached for a z_0 such that

$$2z_0 \left.\frac{d\gamma(z)}{dz}\right|_{z=z_0} = \gamma(z_0). \tag{B.24}$$

In that case, the minimum of the product will be

$$f_{min} = (Var(\tau)Var(\delta))_{min} = \frac{\gamma^2(z_0)}{4(WT)^2 z_0}, \tag{B.25}$$

Then, the bound for the simultaneous measurement in equation 2.70 for each C^i is

$$\sigma^i = \frac{C^i(z_0)^2}{4(WT)^2 z_0}. \tag{B.26}$$

Appendix C

Phase step hologram for vortex beams

To compare the results with other works [19, 122], we consider a transmission function of the following form:

$$\begin{aligned} T_\pi(\varphi) &= \exp\Big[i\alpha \sin\big(\Theta_\pi(\varphi) - \frac{2\pi}{\Lambda} r\cos\varphi\big)\Big] \\ &= \sum_m t_m \exp\Big[im\Theta_\pi(\varphi) - im\frac{2\pi}{\Lambda} r\cos(\theta-\varphi)\Big], \end{aligned} \tag{C.1}$$

where $\Theta_\pi(\varphi)$ is the piecewise function corresponding to dividing the SLM display in two halves, with 0 phase in one side and π phase in the other one, namely

$$\Theta_\pi(\varphi) = \begin{cases} 0 & \text{if } -\frac{\pi}{2} < \varphi < \frac{\pi}{2} \\ \pi & \text{if } \frac{\pi}{2} < \varphi < \frac{3\pi}{2}. \end{cases} \tag{C.2}$$

Substituting in Eq. (3.42), from Eq. (3.50) it follows that

$$U_m(\rho_m, \theta_m) = \frac{\exp(2ikf)}{\lambda f}\, t_m \sum_{l,s} i^{s+1} \exp\Big[is\theta_m\Big]\, I_s \int r\mathrm{d}r\, a_l(r) J_s\Big(\frac{k\rho}{f} r\Big) \tag{C.3}$$

where I_s is the angular integral

$$
\begin{aligned}
I_s &= \int_{-\frac{\pi}{2}}^{\frac{3\pi}{2}} \mathrm{d}\varphi \exp\Big\{\Big[i(l-s)\varphi + im\theta_\pi(\varphi)\Big]\Big\} \\
&= \int_{-\frac{\pi}{2}}^{\frac{\pi}{2}} \mathrm{d}\varphi \exp\Big\{\Big[i(l-s)\varphi\Big]\Big\} + \int_{\frac{\pi}{2}}^{\frac{3\pi}{2}} \mathrm{d}\varphi \exp\Big\{\Big[i(l-s)\varphi + im\pi\Big]\Big\} \\
&= \frac{1}{i(l-s)} \exp\Big\{\Big[i(l-s)\varphi\Big]\Big\}\Big|_{-\frac{\pi}{2}}^{\frac{\pi}{2}} + \frac{\exp[im\pi]}{i(l-s)} \exp\Big\{\Big[i(l-s)\varphi\Big]\Big\}\Big|_{\frac{\pi}{2}}^{\frac{3\pi}{2}} \\
&= \frac{1}{i(l-s)} \exp\Big\{\Big[i(l-s)\varphi\Big]\Big\}\Big|_{-\frac{\pi}{2}}^{\frac{\pi}{2}} + \frac{\exp[im\pi]}{i(l-s)} \exp\{[i(l-s)\pi]\} \exp\Big\{\Big[i(l-s)\varphi\Big]\Big\}\Big|_{-\frac{\pi}{2}}^{\frac{\pi}{2}} \\
&= \frac{2}{(l-s)} \sin\Big((l-s)\frac{\pi}{2}\Big)\Big[1 + \exp[im\pi] \exp\{[i(l-s)\pi]\}\Big]. \qquad \text{(C.4)}
\end{aligned}
$$

We see that for the first diffraction order $m = 1$ (and any $|m|$ odd),

$$
I_s = \pi \,\mathrm{sinc}\Big((l-s)\frac{\pi}{2}\Big)\Big[1 - \exp\{[i(l-s)\pi]\}\Big]. \qquad \text{(C.5)}
$$

In particular for an incoming Gaussian beam, $U_0 = a_0(r) \to l \equiv 0$, I_s vahishes for s not odd

$$
I_s = \pi \,\mathrm{sinc}\Big(\frac{s\pi}{2}\Big)\Big[1 - \exp\{[-is\pi]\}\Big] = 2\pi \mathrm{sinc}\Big(\frac{s\pi}{2}\Big). \qquad \text{(C.6)}
$$

Figure C.1a shows the values of the integral I_s. Note that I_s is nonzero for s odd and the principal contributions to the field U_m are for $s = -1, 1$. Explicitly, plugging Eq. (C.6) back in Eq. (C.3),

$$
U_m(\rho_m, \theta_m) = 2\pi \, q_f \, t_m \sum_{s_{odd}} i^{s+1} \exp[is\theta_m] \,\mathrm{sinc}\Big[\frac{s\pi}{2}\Big] \int r\mathrm{d}r \, a_l(r) J_s\Big(\frac{k\rho}{f} r\Big), \quad \text{(C.7)}
$$

where $q_f = \exp(2ikf)/\lambda f$. Making use of the identity $J_{-s}(z) = (-1)^s J_s(z)$ we get

$$
U_m(\rho_m, \theta_m) = \frac{4\pi}{\lambda f} \, t_m \sum_{s_{odd}>0} i^{s+1} \, \cos[s\theta_m] \,\mathrm{sinc}\Big[\frac{s\pi}{2}\Big] \int r\mathrm{d}r \, a_l(r) J_s\Big(\frac{k\rho_m}{f} r\Big). \quad \text{(C.8)}
$$

Consider an incoming Gaussian beam:

$$
U_0(r, \varphi) = a_0(r) = \frac{1}{\sqrt{\pi w_0^2}} \exp\Big\{\Big[-\frac{r^2}{2w_0^2}\Big]\Big\}. \qquad \text{(C.9)}
$$

The field of the first diffraction order ($m = 1$) after the 2f system in Eq. (C.8), using $(\rho_1, \theta_1) = (\rho, \theta)$ reduces to:

$$
U_1(\rho, \theta) = \frac{4\pi}{\lambda f} \frac{t_1}{\sqrt{\pi w_0^2}} \sum_{s_{odd}>0} i^{s+1} \, \cos[s\theta] \,\mathrm{sinc}\Big[\frac{s\pi}{2}\Big] \int r\mathrm{d}r \, \exp\Big\{\Big[-\frac{r^2}{2w_0^2}\Big]\Big\} J_s\Big(\frac{k\rho}{f} r\Big). \qquad \text{(C.10)}
$$

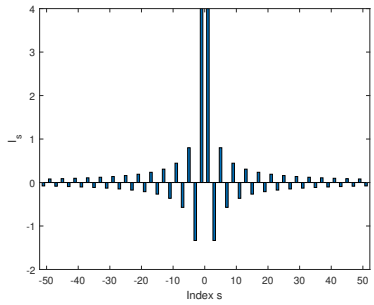

(a) Angular integral I_s.

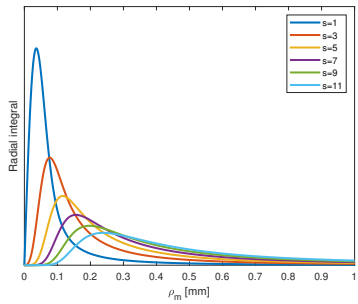

(b) Radial integral.

Figure C.1: Values of the angular (a) and radial (b) integrals corresponding to the different components s contributing to the field $U_m(\rho_m, \theta_m)$ after the 2f system.

Figure C.1b shows the radial integrals with index s in Eq. (C.10) as function of the diffraction order radial coordinate ρ. Note that the first component $s = 1$ dominates strongly.

It is common in literature (see Refs. [19,122]) to assume, using a similar method, to generate a TEM_{10} mode, with the form:

$$U_{TEM_{mn}} = E_{mn}\, H_m\Big(\frac{x}{w}\Big)\, \exp\Big\{\big[\frac{x^2}{2w^2}\big]\Big\}\, H_n\Big(\frac{y}{w}\Big)\, \exp\Big\{\big[\frac{y^2}{2w^2}\big]\Big\}, \tag{C.11}$$

where E_{mn} is a constant normalization factor and H_j is the $j-$th order Hermite polynomial. The TEM_{10} mode is

$$U_{TEM_{10}}(x, y) = E_{10}\, \frac{2x}{w}\, \exp\Big\{\big[-\frac{(x^2 + y^2)}{2w^2}\big]\Big\}, \tag{C.12}$$

where $x = \rho\cos\theta$ and $y = \rho\sin\theta$. Figure C.2 shows the intensity profile of the field in Eq. (C.10) considering 50 terms of the sum over s (a) compared to the first

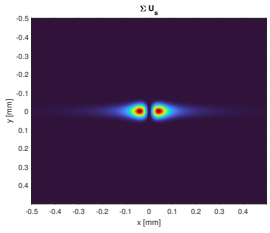

(a) $|\sum_s U_s|^2$

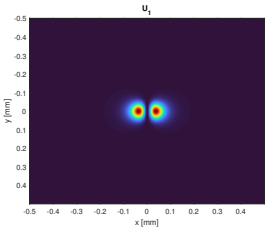

(b) $|U_{s=1}|^2$

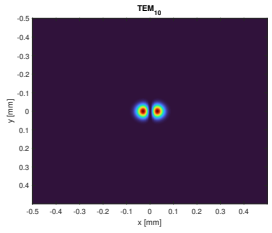

(c) $|TEM_{01}|^2$

Figure C.2: Intensity profile comparison for generation of the TEM_{01} mode (a) the sum of 50 mode contributions, (b) the first mode $s = 1$ and (c) the TEM_{10} mode with waist $w_0' = \lambda f/2\pi w_0$.

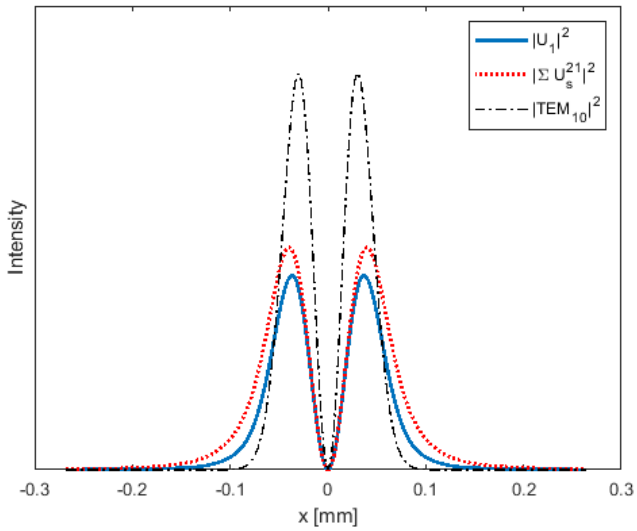

Figure C.3: Intensity profiles along the horizontal line $y = 0$ of the image plane after the 2f system.

term $s = 1$ (b) and the TEM_{01} desired mode (c). The transverse intensity profiles are compared in Fig. C.3. Furthermore, we can compare the spatial profiles of the field with respect to each other by computing the fidelity. For two normalized fields $U_1(x, y)$ and $U_2(x, y)$, such that $\int |U_i(x, y)|^2 \, \mathrm{d}x \, \mathrm{d}y = 1$, the fidelity is:

$$F(U_1, U_2) = \int U_1(x, y) \, U_2^*(x, y) \, \mathrm{d}x \, \mathrm{d}y. \tag{C.13}$$

Comparing the field TEM_{10} to the field in Eq. (C.10), considering the single first term and the sum of the even contributions up to $s = 50$ we see that the fidelity between them is:

$$F(TEM_{10}, \Sigma_1^{50} U_m) = 0.815$$
$$F(TEM_{10}, \Sigma_1^{1} U_m) = 0.887$$
$$F(\Sigma_1^{50} U_m, \Sigma_1^{1} U_m) = 0.918.$$

Bibliography

[1] L. Rayleigh, "Xxxi. investigations in optics, with special reference to the spectroscope," *The London, Edinburgh, and Dublin Philosophical Magazine and Journal of Science*, vol. 8, no. 49, pp. 261–274, 1879.

[2] G. R. Fowles, *Introduction to modern optics*. Courier Corporation, 1989.

[3] M. Born and E. Wolf, *Principles of optics: electromagnetic theory of propagation, interference and diffraction of light*. Elsevier, 2013.

[4] C. G. Schroer, O. Kurapova, J. Patommel, P. Boye, J. Feldkamp, B. Lengeler, M. Burghammer, C. Riekel, L. Vincze, A. van der Hart, *et al.*, "Hard x-ray nanoprobe based on refractive x-ray lenses," *Applied Physics Letters*, vol. 87, no. 12, p. 124103, 2005.

[5] S. W. Hell and J. Wichmann, "Breaking the diffraction resolution limit by stimulated emission: stimulated-emission-depletion fluorescence microscopy," *Optics Letters*, vol. 19, no. 11, pp. 780–782, 1994.

[6] S. W. Hell, "Far-field optical nanoscopy," *Science*, vol. 316, no. 5828, pp. 1153–1158, 2007.

[7] B. Hecht, B. Sick, U. P. Wild, V. Deckert, R. Zenobi, O. J. Martin, and D. W. Pohl, "Scanning near-field optical microscopy with aperture probes: Fundamentals and applications," *The Journal of Chemical Physics*, vol. 112, no. 18, pp. 7761–7774, 2000.

[8] U. Dürig, D. W. Pohl, and F. Rohner, "Near-field optical-scanning microscopy," *Journal of Applied Physics*, vol. 59, no. 10, pp. 3318–3327, 1986.

[9] L. Novotny and N. Van Hulst, "Antennas for light," *Nature Photonics*, vol. 5, no. 2, pp. 83–90, 2011.

[10] A. Lewis, M. Isaacson, A. Harootunian, and A. Muray, "Development of a 500 å spatial resolution light microscope: I. light is efficiently transmitted through $\lambda/16$ diameter apertures," *Ultramicroscopy*, vol. 13, no. 3, pp. 227–231, 1984.

[11] D. W. Pohl, W. Denk, and M. Lanz, "Optical stethoscopy: Image recording with resolution $\lambda/20$," *Applied Physics Letters*, vol. 44, no. 7, pp. 651–653, 1984.

[12] M. Moharam and T. Gaylord, "Rigorous coupled-wave analysis of planar-grating diffraction," *JOSA*, vol. 71, no. 7, pp. 811–818, 1981.

[13] O. El Gawhary, N. Kumar, S. Pereira, W. Coene, and H. Urbach, "Performance analysis of coherent optical scatterometry," *Applied Physics B*, vol. 105, no. 4, pp. 775–781, 2011.

[14] W. Osten, A. Faridian, P. Gao, K. Körner, D. Naik, G. Pedrini, A. K. Singh, M. Takeda, and M. Wilke, "Recent advances in digital holography," *Applied optics*, vol. 53, no. 27, pp. G44–G63, 2014.

[15] W. Hoppe *et al.*, "Trace structure analysis, ptychography, phase tomography," *Ultramicroscopy*, vol. 10, no. 3, pp. 187–198, 1982.

[16] J. M. Rodenburg, "Ptychography and related diffractive imaging methods," *Advances in imaging and electron physics*, vol. 150, pp. 87–184, 2008.

[17] A. J. Den Dekker and A. Van den Bos, "Resolution: a survey," *JOSA A*, vol. 14, no. 3, pp. 547–557, 1997.

[18] C. W. Helstrom, "Estimation of object parameters by a quantum-limited optical system," *JOSA*, vol. 60, no. 2, pp. 233–239, 1970.

[19] V. Delaubert, N. Treps, M. Lassen, C. C. Harb, C. Fabre, P. K. Lam, and H. A. Bachor, "Tem 10 homodyne detection as an optimal small-displacement and tilt-measurement scheme," *Physical Review A*, vol. 74, no. 5, p. 053823, 2006.

[20] V. Delaubert, N. Treps, C. Fabre, H. A. Bachor, and P. Réfrégier, "Quantum limits in image processing," *EPL (Europhysics Letters)*, vol. 81, no. 4, p. 44001, 2008.

[21] L. Pezzè, M. A. Ciampini, N. Spagnolo, P. C. Humphreys, A. Datta, I. A. Walmsley, M. Barbieri, F. Sciarrino, and A. Smerzi, "Optimal measurements for simultaneous quantum estimation of multiple phases," *Physical Review Letters*, vol. 119, no. 13, p. 130504, 2017.

[22] C. W. Helstrom, "Quantum detection and estimation theory," *Journal of Statistical Physics*, vol. 1, no. 2, pp. 231–252, 1969.

[23] A. S. Holevo, *Probabilistic and statistical aspects of quantum theory*, vol. 1. Springer Science & Business Media, 2011.

[24] C. W. Helstrom, "Detection and resolution of incoherent objects by a background-limited optical system," *JOSA*, vol. 59, no. 2, pp. 164–175, 1969.

[25] M. Tsang, "Quantum limits to optical point-source localization," *Optica*, vol. 2, no. 7, pp. 646–653, 2015.

[26] M. Tsang, R. Nair, and X.-M. Lu, "Quantum theory of superresolution for two incoherent optical point sources," *Physical Review X*, vol. 6, no. 3, p. 031033, 2016.

[27] R. Nair and M. Tsang, "Far-field superresolution of thermal electromagnetic sources at the quantum limit," *Physical Review Letters*, vol. 117, no. 19, p. 190801, 2016.

[28] J. Řehaček, Z. Hradil, B. Stoklasa, M. Paúr, J. Grover, A. Krzic, and L. Sánchez-Soto, "Multiparameter quantum metrology of incoherent point sources: towards realistic superresolution," *Physical Review A*, vol. 96, no. 6, p. 062107, 2017.

[29] R. Nair and M. Tsang, "Beating rayleigh's criterion: Superresolution of thermal sources with linear optics," in *Quantum Information and Measurement*, pp. QT5C–5, Optical Society of America, 2017.

[30] W.-K. Tham, H. Ferretti, and A. M. Steinberg, "Beating rayleigh's curse by imaging using phase information," *Physical Review Letters*, vol. 118, no. 7, p. 070801, 2017.

[31] M. Paúr, B. Stoklasa, J. Grover, A. Krzic, L. L. Sánchez-Soto, Z. Hradil, and J. Řeháček, "Tempering rayleigh's curse with psf shaping," *Optica*, vol. 5, no. 10, pp. 1177–1180, 2018.

[32] S. Zhou and L. Jiang, "Modern description of rayleigh's criterion," *Physical Review A*, vol. 99, no. 1, p. 013808, 2019.

[33] J. Wolfowitz, "Asymptotic efficiency of the maximum likelihood estimator," *Theory of Probability & Its Applications*, vol. 10, no. 2, pp. 247–260, 1965.

[34] H. L. Van Trees, *Detection, estimation, and modulation theory, part I: detection, estimation, and linear modulation theory*. John Wiley & Sons, 2004.

[35] S.-i. Amari, *Information geometry and its applications*, vol. 194. Springer, 2016.

[36] M. G. Paris, "Quantum estimation for quantum technology," *International Journal of Quantum Information*, vol. 7, no. supp01, pp. 125–137, 2009.

[37] P. A. M. Dirac, "On the analogy between classical and quantum mechanics," *Reviews of Modern Physics*, vol. 17, no. 2-3, p. 195, 1945.

[38] H. Nagaoka, "A new approach to cràmer-rao bounds for quantum state estimation," *IEICE Technical Report*, vol. 89, no. 228, pp. 9–14, 1989.

[39] K. Matsumoto, "A geometrical approach to quantum estimation theory," in *Asymptotic Theory Of Quantum Statistical Inference: Selected Papers*, pp. 305–350, World Scientific, 2005.

[40] A. Fujiwara and H. Nagaoka, "Quantum fisher metric and estimation for pure state models," *Physics Letters A*, vol. 201, no. 2-3, pp. 119–124, 1995.

[41] A. Fujiwara, "Strong consistency and asymptotic efficiency for adaptive quantum estimation problems," *JOURNAL OF PHYSICS-LONDON-A MATHEMATICAL AND GENERAL*, vol. 39, no. 40, p. 12489, 2006.

[42] K. Matsumoto, "A new approach to the cramér-rao-type bound of the pure-state model," *Journal of Physics A: Mathematical and General*, vol. 35, no. 13, p. 3111, 2002.

[43] A. Fujiwara, "Geometry of quantum estimation theory," in *Asymptotic Theory Of Quantum Statistical Inference: Selected Papers*, pp. 229–286, World Scientific, 2005.

[44] A. Fujiwara and H. Nagaoka, "An estimation theoretical characterization of coherent states," in *Asymptotic Theory Of Quantum Statistical Inference: Selected Papers*, pp. 287–304, World Scientific, 2005.

[45] J. Suzuki, "Explicit formula for the holevo bound for two-parameter qubit-state estimation problem," *Journal of Mathematical Physics*, vol. 57, no. 4, p. 042201, 2016.

[46] K. Yamagata, A. Fujiwara, R. D. Gill, *et al.*, "Quantum local asymptotic normality based on a new quantum likelihood ratio," *The Annals of Statistics*, vol. 41, no. 4, pp. 2197–2217, 2013.

[47] M. Hayashi and K. Matsumoto, "Asymptotic performance of optimal state estimation in qubit system," *Journal of Mathematical Physics*, vol. 49, no. 10, p. 102101, 2008.

[48] M. Guţă and J. Kahn, "Local asymptotic normality for qubit states," *Physical Review A*, vol. 73, no. 5, p. 052108, 2006.

[49] J. Kahn and M. Guţă, "Local asymptotic normality for finite dimensional quantum systems," *Communications in Mathematical Physics*, vol. 289, no. 2, pp. 597–652, 2009.

[50] S. L. Braunstein and C. M. Caves, "Statistical distance and the geometry of quantum states," *Physical Review Letters*, vol. 72, no. 22, p. 3439, 1994.

[51] S. L. Braunstein, C. M. Caves, and G. J. Milburn, "Generalized uncertainty relations: theory, examples, and lorentz invariance," *annals of physics*, vol. 247, no. 1, pp. 135–173, 1996.

[52] J. Liu, J. Chen, X.-X. Jing, and X. Wang, "Quantum fisher information and symmetric logarithmic derivative via anti-commutators," *Journal of Physics A: Mathematical and Theoretical*, vol. 49, no. 27, p. 275302, 2016.

[53] D. Šafránek, "Simple expression for the quantum fisher information matrix," *Physical Review A*, vol. 97, no. 4, p. 042322, 2018.

[54] D. Bures, "D. bures, trans. am. math. soc. 135, 199 (1969).," *Trans. Am. Math. Soc.*, vol. 135, p. 199, 1969.

[55] A. Uhlmann, "A. uhlmann, rep. math. phys. 9, 273 (1976).," *Rep. Math. Phys.*, vol. 9, p. 273, 1976.

[56] D. Šafránek, "Discontinuities of the quantum fisher information and the bures metric," *Physical Review A*, vol. 95, no. 5, p. 052320, 2017.

[57] C. Zhang, Y.-F. Huang, B.-H. Liu, C.-F. Li, and G.-C. Guo, "Spontaneous parametric down-conversion sources for multiphoton experiments," *Advanced Quantum Technologies*, vol. 4, no. 5, p. 2000132, 2021.

[58] G. Grynberg, A. Aspect, and C. Fabre, *Introduction to quantum optics: from the semi-classical approach to quantized light*. Cambridge university press, 2010.

[59] E. Arthurs and J. Kelly, "Bstj briefs: On the simultaneous measurement of a pair of conjugate observables," *The Bell System Technical Journal*, vol. 44, no. 4, pp. 725–729, 1965.

[60] Q. Zhuang, Z. Zhang, and J. H. Shapiro, "Entanglement-enhanced lidars for simultaneous range and velocity measurements," *Physical Review A*, vol. 96, no. 4, p. 040304, 2017.

[61] A. Villegas, M. H. M. Passos, and J. P. Torres, "Quantum limits for the precision of optical parameter estimation of arbitrarily shaped phase objects," 2023.

[62] M. Paúr, B. Stoklasa, Z. Hradil, L. L. Sánchez-Soto, and J. Rehacek, "Achieving the ultimate optical resolution," *Optica*, vol. 3, no. 10, pp. 1144–1147, 2016.

[63] J. Hassett, T. Malhorta, M. Alonso, R. Boyd, S. H. Rafsanjani, and A. Vamivakas, "Sub-rayleigh limit localization with a spatial mode analyzer," in *Laser Science*, pp. JW4A–124, Optical Society of America, 2018.

[64] Y. Zhou, J. Yang, J. D. Hassett, S. M. H. Rafsanjani, M. Mirhosseini, A. N. Vamivakas, A. N. Jordan, Z. Shi, and R. W. Boyd, "Quantum-limited estimation of the axial separation of two incoherent point sources," *Optica*, vol. 6, no. 5, pp. 534–541, 2019.

[65] C. Napoli, S. Piano, R. Leach, G. Adesso, and T. Tufarelli, "Towards superresolution surface metrology: quantum estimation of angular and axial separations," *Physical review letters*, vol. 122, no. 14, p. 140505, 2019.

[66] S. Z. Ang, R. Nair, and M. Tsang, "Quantum limit for two-dimensional resolution of two incoherent optical point sources," *Physical Review A*, vol. 95, no. 6, p. 063847, 2017.

[67] J. P. Torres and L. J. Salazar-Serrano, "Weak value amplification: a view from quantum estimation theory that highlights what it is and what isn't," *Scientific reports*, vol. 6, no. 1, pp. 1–11, 2016.

[68] L. Cisotto and H. P. Urbach, "Amplitude and phase beam shaping for highest sensitivity in sidewall angle detection," *JOSA A*, vol. 34, no. 1, pp. 52–60, 2017.

[69] O. Cordero, A. Villegas, J.-R. Alvarez, R. d. J. León-Montiel, M. H. M. Passos, and J. P. Torres, "Equivalence regimes for geometric quantum discord and local quantum uncertainty," *Phys. Rev. A*, vol. 104, p. 042401, Oct 2021.

[70] K. Modi, H. Cable, M. Williamson, and V. Vedral, "Quantum correlations in mixed-state metrology," *Phys. Rev. X*, vol. 1, p. 021022, Dec 2011.

[71] L. Henderson and V. Vedral, "Classical, quantum and total correlations," *Journal of Physics A: mathematical and general*, vol. 34, no. 35, p. 6899, 2001.

[72] H. Ollivier and W. H. Zurek, "Quantum discord: a measure of the quantumness of correlations," *Physical Review Letters*, vol. 88, no. 1, p. 017901, 2002.

[73] Y. Huang, "Computing quantum discord is np-complete," *New Journal of Physics*, vol. 16, p. 033027, 2014.

[74] S. Luo, "Quantum discord for two-qubit systems," *Physical Review A*, vol. 77, p. 042303, 2008.

[75] M. Ali, A. Rau, and G. Alber, "Quantum discord for two-qubit x states," *Physical Review A*, vol. 81, no. 4, p. 042105, 2010.

[76] Q. Chen, C. Zhang, S. Yu, X. Yi, and C. Oh, "Quantum discord of two-qubit x states," *Physical Review A*, vol. 84, no. 4, p. 042313, 2011.

[77] K. Modi, A. Brodutch, H. Cable, T. Paterek, and V. Vedral, "The classical-quantum boundary for correlations: discord and related measures," *Reviews of Modern Physics*, vol. 84, p. 1655, 2012.

[78] B. Dakić, V. Vedral, and C. Brukner, "Necessary and sufficient condition for nonzero quantum discord," *Phys. Rev. Lett.*, vol. 105, p. 190502, 2010.

[79] A. Datta, "A condition for the nullity of quantum discord," *arXiv:1003.5256v2 [quant-ph]*, 2011.

[80] A. A. Ferraro, L. Aolita, D. Cavalcanti, F. M. Cucchietti, 1, and A. Acın, "Almost all quantum states have nonclassical correlations," *Physical Review A*, vol. 81, p. 052318, 2010.

[81] J. S. S. Ferreira, D. Filenga, M. F. Cornelio, and F. F. Fanchini, "Multipartite monogamous relations for entanglement and discord," *Physical Review A*, vol. 97, p. 012328, 2018.

[82] P. Busch and P. Lahti, *Lüders Rule*. Springer Berlin Heidelberg, 2009.

[83] S. Luo and Y. Sun, "Quantum coherence versus quantum uncertainty," *Physical Review A*, vol. 96, p. 022130, 2017.

[84] G. Adesso, M. Cianciaruso, and T. R. Bromley, "An introduction to quantum discord and non-classical correlations beyond entanglement," *arXiv:1611.01959v1 [quant-ph]*, vol. 7 November 2016, 2016.

[85] M. Piani, "Problem with geometric discord," *Physical Review A*, vol. 86, p. 034101, 2012.

[86] L. Chang and S. Luo, "Remedying the local ancilla problem with geometric discord," *Physical Review A*, vol. 87, p. 062303, 2013.

[87] S. Luo and S. Fu, "Evaluating the geometric measure of quantum discord," *Theoretical and Mathematical Physics*, vol. 171, p. 870, 2012.

[88] D. Girolami, T. Tufarelli, and G. Adesso, "Characterizing nonclassical correlations via local quantum uncertainty," *Physical Review Letters*, vol. 110, p. 240402, 2013.

[89] E. P. Wigner and M. M. Yanase, "Information contents of distributions," *Proceedings of the National Academy of Sciences*, vol. 49, p. 910, 1963.

[90] A. Rasin, "Diagonalization of quark mass matrices and the cabibbo-kobayashi-maskawa matrix," *arXiv:hep-ph/9708216*, 1997.

[91] M. W. Mitchell, J. S. Lundeen, and A. M. Steinberg, "Super-resolving phase measurements with a multiphoton entangled state," *Nature*, vol. 429, p. 161–164, May 2004.

[92] R. Demkowicz-Dobrzanski, U. Dorner, B. J. Smith, J. S. Lundeen, W. Wasilewski, K. Banaszek, and I. A. Walmsley, "Quantum phase estimation with lossy interferometers," *Physical Review A*, vol. 80, p. 013825, 2009.

[93] Z. Y. M., X. W. Li, W. Yang, and G. R. Jin, "Quantum fisher information of entangled coherent states in the presence of photon loss," *Physical Review A*, vol. 88, p. 043832, 2013.

[94] R. Horodecki, P. Horodecki, M. Horodecki, and K. Horodecki, "Quantum entanglement," *Review of Modern Physics*, vol. 81, pp. 865–942, 2009.

[95] T. Malhotra, W. E. Farriss, J. Hassett, A. F. Abouraddy, J. R. Fienup, and A. N. Vamivakas, "Interferometric spatial mode analyzer with a bucket detector," *Optics Express*, vol. 26, no. 7, pp. 8719–8728, 2018.

[96] L. Eyges, *The classical electromagnetic field*. Courier Corporation, 2012.

[97] R. Haberman, *Applied partial differential equations*, vol. 4. Prentice Hall Upper Saddle River, NJ:, 2003.

[98] J. Pinnell, I. Nape, B. Sephton, M. A. Cox, V. Rodríguez-Fajardo, and A. Forbes, "Modal analysis of structured light with spatial light modulators: a practical tutorial," *JOSA A*, vol. 37, no. 11, pp. C146–C160, 2020.

[99] A. Forbes, "Structured light: tailored for purpose," *Optics and Photonics News*, vol. 31, no. 6, pp. 24–31, 2020.

[100] S. Oemrawsingh, J. Van Houwelingen, E. Eliel, J. Woerdman, E. Verstegen, J. Kloosterboer, *et al.*, "Production and characterization of spiral phase plates for optical wavelengths," *Applied optics*, vol. 43, no. 3, pp. 688–694, 2004.

[101] A. Rubano, F. Cardano, B. Piccirillo, and L. Marrucci, "Q-plate technology: a progress review," *JOSA B*, vol. 36, no. 5, pp. D70–D87, 2019.

[102] L. Marrucci, "The q-plate and its future," *Journal of Nanophotonics*, vol. 7, no. 1, p. 078598, 2013.

[103] L. Marrucci, C. Manzo, and D. Paparo, "Optical spin-to-orbital angular momentum conversion in inhomogeneous anisotropic media," *Physical review letters*, vol. 96, no. 16, p. 163905, 2006.

[104] N. Heckenberg, R. McDuff, C. Smith, and A. White, "Generation of optical phase singularities by computer-generated holograms," *Optics letters*, vol. 17, no. 3, pp. 221–223, 1992.

[105] G. Tricoles, "Computer generated holograms: an historical review," *Applied optics*, vol. 26, no. 20, pp. 4351–4360, 1987.

[106] P.-G. De Gennes and J. Prost, *The physics of liquid crystals*. No. 83, Oxford university press, 1993.

[107] B. R. Boruah, "Dynamic manipulation of a laser beam using a liquid crystal spatial light modulator," *American Journal of Physics*, vol. 77, no. 4, pp. 331–336, 2009.

[108] A. Forbes, A. Dudley, and M. McLaren, "Creation and detection of optical modes with spatial light modulators," *Advances in Optics and Photonics*, vol. 8, no. 2, pp. 200–227, 2016.

[109] C. Rosales-Guzmán and A. Forbes, *How to shape light with spatial light modulators*. SPIE Press, 2017.

[110] J. A. Davis, D. M. Cottrell, J. Campos, M. J. Yzuel, and I. Moreno, "Encoding amplitude information onto phase-only filters," *Applied optics*, vol. 38, no. 23, pp. 5004–5013, 1999.

[111] V. Arrizón, G. Méndez, and D. Sánchez-de La-Llave, "Accurate encoding of arbitrary complex fields with amplitude-only liquid crystal spatial light modulators," *Optics Express*, vol. 13, no. 20, pp. 7913–7927, 2005.

[112] V. Arrizón, U. Ruiz, R. Carrada, and L. A. González, "Pixelated phase computer holograms for the accurate encoding of scalar complex fields," *JOSA A*, vol. 24, no. 11, pp. 3500–3507, 2007.

[113] L. Zhu and J. Wang, "Arbitrary manipulation of spatial amplitude and phase using phase-only spatial light modulators," *Scientific reports*, vol. 4, no. 1, pp. 1–7, 2014.

[114] M. Karamehmedović, K. Scheel, F. L.-S. Pedersen, A. Villegas, and P.-E. Hansen, "Steerable photonic jet for super-resolution microscopy," *Optics Express*, vol. 30, no. 23, pp. 41757–41773, 2022.

[115] G. N. Watson, *A treatise on the theory of Bessel functions*, vol. 3. The University Press, 1922.

[116] H. Rubinsztein-Dunlop, A. Forbes, M. V. Berry, *et al.*, "Roadmap on structured light," *Journal of Optics*, vol. 19, p. 013001, 2016.

[117] L. Torner, J. P. Torres, and S. Carrasco, "Digital spiral imaging," *Optics express*, vol. 13, no. 3, pp. 873–881, 2005.

[118] S. Fürhapter, A. Jesacher, S. Bernet, and M. Ritsch-Marte, "Spiral phase contrast imaging in microscopy," *Optics Express*, vol. 13, p. 689, 2005.

[119] G. Xie, H. Song, Z. Zhao, G. Milione, Y. Ren, C. Liu, *et al.*, "Using a complex optical orbital-angular-momentum spectrum to measure object parameters," *Optics Letters*, vol. 42, p. 4482, 2017.

[120] J. P. Torres and L. Torner, *Twisted photons: applications of light with orbital angular momentum*. John Wiley & Sons, 2011.

[121] J. Rehacek, M. Paúr, B. Stoklasa, Z. Hradil, and L. L. Sanchez-Soto, "Optimal measurements for resolution beyond the rayleigh limit," *Optics letters*, vol. 42, no. 2, pp. 231–234, 2017.

[122] M. T. Hsu, V. Delaubert, P. K. Lam, and W. P. Bowen, "Optimal optical measurement of small displacements," *Journal of Optics B: Quantum and Semiclassical Optics*, vol. 6, no. 12, p. 495, 2004.

[123] A. Villegas and J. P. Torres, "Spatial spectroscopy for high resolution imaging," in *EPJ Web of Conferences*, vol. 238, p. 06005, EDP Sciences, 2020.

[124] N. Treps, U. Andersen, B. Buchler, P. K. Lam, A. Maitre, H.-A. Bachor, and C. Fabre, "Surpassing the standard quantum limit for optical imaging using nonclassical multimode light," *Physical Review Letters*, vol. 88, no. 20, p. 203601, 2002.

[125] V. Delaubert, N. Treps, C. C. Harb, P. K. Lam, and H.-A. Bachor, "Quantum measurements of spatial conjugate variables: displacement and tilt of a gaussian beam," *Optics Letters*, vol. 31, no. 10, pp. 1537–1539, 2006.

[126] L. Janicijevic and S. Topuzoski, "Fresnel and fraunhofer diffraction of a gaussian laser beam by fork-shaped gratings," *JOSA A*, vol. 25, no. 11, pp. 2659–2669, 2008.

[127] S. Topuzoski and L. Janicijevic, "Fraunhofer diffraction of a laguerre–gaussian laser beam by fork-shaped grating," *Journal of Modern Optics*, vol. 58, no. 2, pp. 138–145, 2011.

[128] L. Stoyanov, S. Topuzoski, I. Stefanov, L. Janicijevic, and A. Dreischuh, "Far field diffraction of an optical vortex beam by a fork-shaped grating," *Optics Communications*, vol. 350, pp. 301–308, 2015.

[129] A. N. Jordan, J. Martínez-Rincón, and J. C. Howell, "Technical advantages for weak-value amplification: when less is more," *Physical Review X*, vol. 4, no. 1, p. 011031, 2014.

[130] C. Lupo and S. Pirandola, "Ultimate precision bound of quantum and subwavelength imaging," *Physical Review Letters*, vol. 117, no. 19, p. 190802, 2016.

[131] F. Yang, R. Nair, M. Tsang, C. Simon, and A. I. Lvovsky, "Fisher information for far-field linear optical superresolution via homodyne or heterodyne detection in a higher-order local oscillator mode," *Physical Review A*, vol. 96, no. 6, p. 063829, 2017.

[132] J. Řeháček, Z. Hradil, D. Koutnỳ, J. Grover, A. Krzic, and L. L. Sánchez-Soto, "Optimal measurements for quantum spatial superresolution," *Physical Review A*, vol. 98, no. 1, p. 012103, 2018.

[133] W. Larson and B. E. Saleh, "Resurgence of rayleigh's curse in the presence of partial coherence," *Optica*, vol. 5, no. 11, pp. 1382–1389, 2018.

[134] A. Villegas, M. A. Quiroz-Juárez, A. B. U'Ren, J. P. Torres, and R. d. J. León-Montiel, "Identification of model particle mixtures using machine-learning-assisted laser diffraction," in *Photonics*, vol. 9, p. 74, MDPI, 2022.

[135] P. P. Banada, S. Guo, B. Bayraktar, E. Bae, B. Rajwa, J. P. Robinson, E. D. Hirleman, and A. K. Bhunia, "Optical forward-scattering for detection of listeria monocytogenes and other listeria species," *Biosensors and Bioelectronics*, vol. 22, no. 8, pp. 1664–1671, 2007.

[136] J.-E. Park, K. Kim, Y. Jung, J.-H. Kim, and J.-M. Nam, "Metal nanoparticles for virus detection," *ChemNanoMat*, vol. 2, no. 10, pp. 927–936, 2016.

[137] B. Y. Shekunov, P. Chattopadhyay, H. H. Y. Tong, and A. H. L. Chow, "Particle size analysis in pharmaceutics: principles, methods and applications," *Pharm. Res.*, vol. 24, p. 203, 2007.

[138] R. K. Dhamoon, H. Paplo, G. Aggarwal, and M. Gupta, "Particle size characterization-techniques, factors and quality-by-design approach," *International Journal of Drug Delivery*, vol. 10, p. 1, 2018.

[139] M. M. Robins, *Particle size analysis in food. In encyclopedia of analytical chemistry. Eds R. A. Meyers and R. J. McGorring.* Wiley Online Library, 2006.

[140] J. Zhang, D. Liu, Y. Liu, Y. Yu, Y. Hemar, J. M. Regenstein, and P. Zhou, "Effects of particle size and aging of milk protein concentrate on the biophysical properties of an intermediate-moisture model food system," *Food Bioscience*, vol. 37, p. 100698, 2020.

[141] S. Roy, A. Assafrão, S. Pereira, and H. Urbach, "Coherent fourier scatterometry for detection of nanometer-sized particles on a planar substrate surface," *Optics express*, vol. 22, no. 11, pp. 13250–13262, 2014.

[142] A. P. Tinke, A. Carnicer, R. Govoreanu, G. Scheltjens, L. Lauwerysen, N. Mertens, K. Vanhoutte, and M. E. Brewster, "Particle shape and orientation in laser diffraction and static image analysis: size distribution analysis of micrometer sized rectangular particles," *Powder Technology*, vol. 186, p. 154, 2008.

[143] H. K. Imhof, C. Laforsch, A. C. Wiesheu, J. Schmid, P. M. Anger, R. Niessner, and N. P. Ivleva, "Pigments and plastic in limnetic ecosystems: A qualitative and quantitative study on microparticles of different size classes," *Water Research*, vol. 98, pp. 64 – 74, 2016.

[144] K. Parrish and N. Fahrenfeld, "Microplastic biofilm in fresh-and wastewater as a function of microparticle type and size class," *Environmental Science: Water Research & Technology*, vol. 5, no. 3, pp. 495–505, 2019.

[145] D. M. Brown, M. R. Wilson, W. MacNee, V. Stone, and K. Donaldson, "Size-dependent proinflammatory effects of ultrafine polystyrene particles: a role for surface area and oxidative stress in the enhanced activity of ultrafines," *Toxicology and applied pharmacology*, vol. 175, no. 3, pp. 191–199, 2001.

[146] G. Oberdörster, J. Finkelstein, C. Johnston, R. Gelein, C. Cox, R. Baggs, and A. Elder, "Acute pulmonary effects of ultrafine particles in rats and mice.," *Research report (Health Effects Institute)*, no. 96, pp. 5–74, 2000.

[147] H. G. Merkus, *Particle size measurements: Fundamentals, practice, quality*. Springer, 2009.

[148] M. Ltd., *A basic guide to particle characterization*. Malvern, 2015.

[149] R. Xu, "Light scattering: A review of particle characterization applications," *Particuology*, vol. 18, pp. 11–21, 2015.

[150] B. Bradley Deutsch, R. Beams, and L. Novotny, "Nanoparticle detection using dual-phase interferometry," *Applied Optics*, vol. 49, no. 26, pp. 4921–4925, 2010.

[151] J. Stetefeld, S. A. McKenna, and T. R. Patel, "Dynamic light scattering: a practical guide and applications in biomedical sciences," *Biophys. Rev.*, vol. 8, p. 409, 2016.

[152] A. Rawle, *Basic principles of particle size analysis*. Malvern Instruments, 1995.

[153] ISO 13320:2020, *Particle size analysis – Laser diffraction methods*. 2020.

[154] S. J. Blott, D. J. Croft, K. Pye, S. E. Saye, and H. E. Wilson, "Particle size analysis by laser diffraction," *Geological Society, London, Special Publications*, vol. 232, p. 63, 2004.

[155] J. Chen, N. E. Clay, No-hyung Park, and H. Kong, "Non-spherical particles for targeted drug delivery," *Chemical Engineering Science*, vol. 125, pp. 20 – 24, 2015. Pharmaceutical Particles and Processing.

[156] M. Cooley, A. Sarode, M. Hoore, D. A. Fedosov, S. Mitragotri, and A. Sen Gupta, "Influence of particle size and shape on their margination and wall-adhesion: implications in drug delivery vehicle design across nano-to-micro scale," *Nanoscale*, vol. 10, pp. 15350–15364, 2018.

[157] J. M. Ting, L. Meachum, and J. D. Rowell, "Effect of particle shape on the strength and deformation mechanisms of ellipse-shaped granular assemblages," *Engineering Computations*, 1995.

[158] R. Zou and A.-B. Yu, "Evaluation of the packing characteristics of monosized non-spherical particles," *Powder technology*, vol. 88, no. 1, pp. 71–79, 1996.

[159] Z. Ma, H. G. Merkus, J. G. de Smet, C. Heffels, and B. Scarlett, "New developments in particle characterization by laser diffraction: size and shape," *Powder Technology*, vol. 111, no. 1-2, pp. 66–78, 2000.

[160] Z. Ma, H. G. Merkus, and B. Scarlett, "Extending laser diffraction for particle shape characterization: technical aspects and application," *Powder Technology*, vol. 118, no. 1-2, pp. 180–187, 2001.

[161] S. J. Blott and K. Pye, "Particle shape: a review and new methods of characterization and classification," *Sedimentology*, vol. 55, no. 1, pp. 31–63, 2008.

[162] M. L. Hentschel and N. W. Page, "Selection of descriptors for particle shape characterization," *Particle & Particle Systems Characterization: Measurement and Description of Particle Properties and Behavior in Powders and Other Disperse Systems*, vol. 20, no. 1, pp. 25–38, 2003.

[163] J. Hovenier, K. Lumme, M. Mishchenko, N. Voshchinnikov, D. Mackowski, and J. Rahola, "Computations of scattering matrices of four types of nonspherical particles using diverse methods," *Journal of Quantitative Spectroscopy and Radiative Transfer*, vol. 55, no. 6, pp. 695–705, 1996.

[164] M. I. Mishchenko, L. D. Travis, and D. W. Mackowski, "T-matrix computations of light scattering by nonspherical particles: A review," *Journal of Quantitative Spectroscopy and Radiative Transfer*, vol. 55, no. 5, pp. 535–575, 1996.

[165] R. Jia, X. Zhang, F. Cui, G. Chen, H. Li, H. Peng, Z. Cao, and S. Pei, "Machine-learning-based computationally efficient particle size distribution retrieval from bulk optical properties," *Applied Optics*, vol. 59, no. 24, pp. 7284–7291, 2020.

[166] L. E. Altman and D. G. Grier, "Catch: Characterizing and tracking colloids holographically using deep neural networks," *The Journal of Physical Chemistry B*, vol. 124, no. 9, pp. 1602–1610, 2020.

[167] A. L. Daniels, C. P. Calderon, and T. W. Randolph, "Machine learning and statistical analyses for extracting and characterizing "fingerprints" of antibody aggregation at container interfaces from flow microscopy images," *Biotechnology and Bioengineering*, vol. 117, no. 11, pp. 3322–3335, 2020.

[168] H. Hundal, S. Rohani, H. Wood, and M. Pons, "Particle shape characterization using image analysis and neural networks," *Powder technology*, vol. 91, no. 3, pp. 217–227, 1997.

[169] Y. Rivenson, H. C. Koydemir, H. Wang, Z. Wei, Z. Ren, H. Gunaydın, Y. Zhang, Z. Gorocs, K. Liang, D. Tseng, and A. Ozcan, "Deep learning enhanced mobile-phone microscopy," *ACS Photonics*, vol. 5, p. 2354, 2018.

[170] C. Nascimento, R. Guardani, and M. Giulietti, "Use of neural networks in the analysis of particle size distributions by laser diffraction," *Powder Technology*, vol. 90, no. 1, pp. 89–94, 1997.

[171] C. F. Hewitt and P. B. Whalley, "Advanced optical instrumentation methods," *Int. J. Multiphase Flow*, vol. 6, p. 139, 1980.

[172] S. Kang, P. Lyoo, D. Kim, and J. Park, "Laser diffraction pattern analysis of various two-dimensional regular-shaped model particles," *Advanced Powder Technology*, vol. 5, no. 1, pp. 33–42, 1994.

[173] A. Yevick, M. Hannel, and D. G. Grier, "Machine-learning approach to holographic particle characterization," *Optics Express*, vol. 22, p. 26884, 2014.

[174] M. D. Hannel, A. Abdulali, M. O'Brien, and D. G. Grier, "Machine-learning techniques for fast and accurate feature localization in holograms of colloidal particles," *Optics express*, vol. 26, no. 12, pp. 15221–15231, 2018.

[175] S. Helgadottir, A. Argun, and G. Volpe, "Digital video microscopy enhanced by deep learning," *Optica*, vol. 6, p. 506, 2019.

[176] D. Kolenov and S. Pereira, "Machine learning techniques applied for the detection of nanoparticles on surfaces using coherent fourier scatterometry," *Optics Express*, vol. 28, no. 13, pp. 19163–19186, 2020.

[177] R. Hussain, M. A. Noyan, G. Woyessa, R. R. R. Marín, P. A. Martinez, F. M. Mahdi, V. Finazzi, T. A. Hazlehurst, T. N. Hunter, T. Coll, *et al.*, "An ultra-compact particle size analyser using a cmos image sensor and machine learning," *Light: Science & Applications*, vol. 9, no. 1, pp. 1–11, 2020.

[178] R. Guardani, C. Nascimento, and R. Onimaru, "Use of neural networks in the analysis of particle size distribution by laser diffraction: tests with different particle systems," *Powder technology*, vol. 126, no. 1, pp. 42–50, 2002.

[179] D. Kolenov, D. Davidse, J. Le Cam, and S. Pereira, "Convolutional neural network applied for nanoparticle classification using coherent scatterometry data," *Applied Optics*, vol. 59, no. 27, pp. 8426–8433, 2020.

[180] A. Perez-Leija, D. Guzman-Silva, R. de J. León-Montiel, M. Grafe, M. Heinrich, H. Moya-Cessa, K. Busch, and A. Szameit, "Endurance of quantum coherence due to particle indistinguishability in noisy quantum networks," *npj Quantum Inf.*, vol. 4, p. 45, 2018.

[181] D. Svozil, V. Kvasnicka, and J. Pospichal, "Introduction to multi-layer feed-forward neural networks," *Chemometrics and intelligent laboratory systems*, vol. 39, no. 1, pp. 43–62, 1997.

[182] I. Goodfellow, Y. Bengio, and A. Courville, *Deep Learning*. MIT Press, 2016. http://www.deeplearningbook.org.

[183] C. M. Bishop, *Pattern recognition and machine learning*. springer, 2006.

[184] M. F. Møller, "A scaled conjugate gradient algorithm for fast supervised learning," *Neural networks*, vol. 6, no. 4, pp. 525–533, 1993.

[185] J. Shore and R. Johnson, "Properties of cross-entropy minimization," *IEEE Transactions on Information Theory*, vol. 27, no. 4, pp. 472–482, 1981.

[186] P.-T. De Boer, D. P. Kroese, S. Mannor, and R. Y. Rubinstein, "A tutorial on the cross-entropy method," *Annals of operations research*, vol. 134, no. 1, pp. 19–67, 2005.

[187] A. Shebani and S. Iwnicki, "Prediction of wheel and rail wear under different contact conditions using artificial neural networks," *Wear*, vol. 406, pp. 173–184, 2018.

[188] C. You, M. A. Quiroz-Juárez, A. Lambert, N. Bhusal, C. Dong, A. Perez-Leija, A. Javaid, R. de J. León-Montiel, and O. S. Magaña-Loaiza, "Identification of light sources using machine learning," *Applied Physics Reviews*, vol. 7, no. 2, p. 021404, 2020.

[189] F. Xing, Y. Xie, H. Su, F. Liu, and L. Yang, "Deep learning in microscopy image analysis: A survey," *IEEE Transactions on Neural Networks and Learning Systems*, vol. 29, no. 10, pp. 4550–4568, 2017.

[190] Y. Rivenson, Z. Göröcs, H. Günaydin, Y. Zhang, H. Wang, and A. Ozcan, "Deep learning microscopy," *Optica*, vol. 4, no. 11, pp. 1437–1443, 2017.

[191] L. Mennel, J. Symonowicz, S. Wachter, D. K. Polyushkin, A. J. Molina-Mendoza, and T. Mueller, "Ultrafast machine vision with 2d material neural network image sensors," *Nature*, vol. 579, no. 7797, pp. 62–66, 2020.

[192] T. Nakazawa and D. V. Kulkarni, "Wafer map defect pattern classification and image retrieval using convolutional neural network," *IEEE Transactions on Semiconductor Manufacturing*, vol. 31, no. 2, pp. 309–314, 2018.

[193] J. O'Leary, K. Sawlani, and A. Mesbah, "Deep learning for classification of the chemical composition of particle defects on semiconductor wafers," *IEEE Transactions on Semiconductor Manufacturing*, vol. 33, no. 1, pp. 72–85, 2020.

[194] M. Bradshaw, S. M. Assad, and P. K. Lam, "A tight cramér–rao bound for joint parameter estimation with a pure two-mode squeezed probe," *Physics Letters A*, vol. 381, no. 32, pp. 2598–2607, 2017.

List of Figures

List of Acronyms

AI Artificial Intelligence.

BS Beam Splitter.

CGH Computer-Generated Hologram.

CMOS Complementary Metal-Oxide Semiconductor.

CR Crámer-Rao.

DLS Dynamic Light Scattering.

DOE Diffractive Optical Element.

EUV Extreme Ultraviolet.

FFT Fast Fourier Transform.

FI Fisher Information.

FIM Fisher Information Matrix.

HG Hermite-Gaussian.

HWP Half-wave Plate.

KKT Karush-Kuhn-Tucker.

LC Liquid Crystal.

LCoS Liquid Crystal on Silicon.

LD Laser Diffraction.

LG Laguerre-Gaussian.

LP Linear Polarizer.

MICR Most Informative Crámer-Rao.

ML Machine Learning.

NN Neural Networks.

PM Power Meter.

PNJ Photonic Nano-jets.

POM Probability Operator Measure.

POVM Positive Operator-Valued Measure.

PSF Point Spread Function.

RLD Right Logarithmic Derivative.

SILVER Superlocalization by Image Inversion Interferometry.

SLD Symmetric Logarithmic Derivative.

SLM Spatial Light Modulator.

SLS Static Light Scattering.

SPADE Spatial-mode Demultiplexing.

SPDC Spontaneous Parametric Down-conversion.

SPP Spiral Phase Plate.

STA Scattering Tracking Analysis.

STED Stimulated Emission Depletion.

TEM Transverse Electromagnetic.

UV Ultraviolet.